

Functional drawn polymer composites

Citation for published version (APA):

Pan, X. (2021). *Functional drawn polymer composites: for thermal management and actuators*. [Phd Thesis 1 (Research TU/e / Graduation TU/e), Chemical Engineering and Chemistry]. Technische Universiteit Eindhoven.

Document status and date:

Published: 29/06/2021

Document Version:

Publisher's PDF, also known as Version of Record (includes final page, issue and volume numbers)

Please check the document version of this publication:

- A submitted manuscript is the version of the article upon submission and before peer-review. There can be important differences between the submitted version and the official published version of record. People interested in the research are advised to contact the author for the final version of the publication, or visit the DOI to the publisher's website.
- The final author version and the galley proof are versions of the publication after peer review.
- The final published version features the final layout of the paper including the volume, issue and page numbers.

[Link to publication](#)

General rights

Copyright and moral rights for the publications made accessible in the public portal are retained by the authors and/or other copyright owners and it is a condition of accessing publications that users recognise and abide by the legal requirements associated with these rights.

- Users may download and print one copy of any publication from the public portal for the purpose of private study or research.
- You may not further distribute the material or use it for any profit-making activity or commercial gain
- You may freely distribute the URL identifying the publication in the public portal.

If the publication is distributed under the terms of Article 25fa of the Dutch Copyright Act, indicated by the "Taverne" license above, please follow below link for the End User Agreement:

www.tue.nl/taverne

Take down policy

If you believe that this document breaches copyright please contact us at:

openaccess@tue.nl

providing details and we will investigate your claim.

Functional drawn polymer composites

for thermal management and actuators

PROEFSCHRIFT

ter verkrijging van de graad van doctor

aan de Technische Universiteit Eindhoven,

op gezag van de rector magnificus prof.dr.ir. F.P.T. Baaijens,

voor een commissie aangewezen door het College voor Promoties,

in het openbaar te verdedigen

op dinsdag 29 juni 2021 om 16:00 uur

door

Xinglong Pan

geboren te Anhui, China

Dit proefschrift is goedgekeurd door de promotoren en de samenstelling van de promotiecommissie is als volgt:

voorzitter: prof.dr.eng. F. Gallucci

1^e promotor: prof.dr. A. P. H. J. Schenning

copromotor(en): prof.dr.ing. C. W. M. Bastiaansen (Queen Mary University of London)

leden: prof.dr. Q. Li (Kent State University)

prof.dr.ir. L. E. Govaert

prof.dr. Z. Tomović

adviseur (s): dr.ir. T. A. P. Engels (DSM)

dr. M. G. Debije

Het onderzoek of ontwerp dat in dit proefschrift wordt beschreven is uitgevoerd in overeenstemming met de TU/e Gedragscode Wetenschapsbeoefening

Let bygones be bygones

Xinglong pan

Functional drawn polymer composites for thermal management and actuators

A catalogue record is available from the Eindhoven University of Technology Library

ISBN: 978-90-386-5309-9

The research in this thesis was supported by the China Scholarship Council (CSC).

Reproduction: ProefschriftMaken || www.proefschriftmaken.nl

Front cover image: This view from NASA's Cassini spacecraft shows a wave structure in Saturn's rings known as the Janus spiral density wave. (Permission from NASA)

Back cover image: The full Moon phase as the International Space Station orbited 264 miles above China near the Mongolian border. (Permission from NASA)

Copyright © 2021 by Xinglong Pan

Table of Contents

Summary

Chapter 1. Introduction	1
1.1 Introduction.....	2
1.2 Achieving anisotropy in polymeric materials	4
1.3 Thermal transport in anisotropic polymer materials	5
1.4 Thermal conductivity of anisotropic polymer materials	9
1.4.1 Thermal conductivity of polymers with post-processing	9
1.4.2 Thermal conductivity of liquid crystal networks.....	13
1.4.3 Thermal conductivity of anisotropic polymer composites	14
1.5 Research aim and outline of the thesis	15
1.6 References.....	17
Chapter 2. The Role of Polyethylene Wax on the Thermal Conductivity of Transparent Ultradrawn Polyethylene Films	21
2.1 Introduction.....	22
2.2 Results and Discussion	22
2.2.1 Thermal conductive and transparent ultradrawn films	22
2.2.2 Model for thermal conductivity, M_n and draw ratio.....	27
2.3 Conclusions.....	29
2.4 Experimental section.....	30
2.5 References.....	32
Chapter 3. Transparent High Thermal Conductivity Ultra-drawn Polyethylene/Graphene Nanocomposite Films	33
3.1 Introduction.....	34
3.2 Results and Discussions	34
3.3 Conclusions.....	40
3.4 Experimental Section	41
3.5 References.....	43
Chapter 4. Enhanced thermal conductivity in oriented polyvinyl alcohol/graphene oxide composites	45
4.1 Introduction.....	46
4.2 Results and Discussion	46

4.3 Conclusions.....	52
4.4 Experimental section.....	53
4.5 References.....	55
4.6 Supporting Information.....	57
Chapter 5. Three-Dimensional Anisotropic Polyethylene as Light-Responsive Grippers and Surfing Divers	61
5.1 Introduction.....	62
5.2 Results and Discussion	63
5.2.1 Preparation of the photothermal actuators.....	63
5.2.2 Photoresponsive actuators	65
5.2.3 NIR light diving-surfer	67
5.2.4 Photo-fueled cargo displacement at liquid surfaces	69
5.3 Conclusions.....	70
5.4 Experimental Section.....	71
5.5 References.....	72
Chapter 6. NIR-Vis-UV Light-Responsive High Stress-Generating Polymer Actuators with a Reduced Creep Rate	75
6.1 Introduction.....	76
6.2 Results and Discussion	77
6.3 Conclusions.....	82
6.4 Experimental Section	83
6.5 References.....	85
Chapter 7. Technology assessment.....	87
Curriculum Vitae.....	95
Acknowledgments.....	97

Summary

Functional drawn polymer composites for thermal management and actuators

Thermal management is vital to extending the lifetime and maintaining the performance of a variety of electronic devices, including solar cells, light-emitting diodes (LEDs), and microchips. With the widespread application of electronics, effective thermal management with thermally conductive materials has become a major technological challenge. Commodity polymers, including polyethylene, polystyrene, and polypropylene, have been explored extensively at large scales over the past decades due to their low density, ease of processing, high electrical resistivity, and corrosion resistance (**Chapter 1**). Although the thermal conductivity of commodity polymers can be enhanced by adding high thermal conductive additives, the increase in thermal conductivity is limited to less than one order of magnitude ($< 10 \text{ W m}^{-1} \text{ K}^{-1}$), resulting from the high thermal interface resistance between the additive and the polymer matrix. Furthermore, most polymer composites become non-transparent with reduced mechanical properties due to the addition of the fillers. These shortcomings limit their application as thermal management windows and (photo-)thermal actuators. In this thesis, high thermal conductivity is obtained in drawn polymers and drawn composite films with high visible light transmission, at least in some cases, and the potential applications of these materials as photo-thermal actuators were explored.

Chapter 2 reports ultra-drawn films of ultra-high molecular weight polyethylene (UHMWPE) blended with a wide range of low molecular weight, monodisperse waxes which exhibit M_n -dependent thermal conductivities. A new model correlating molecular weight, draw ratio, and thermal conductivity is presented and validated against the experimental results, which can be used to predict thermal conductivities of future drawn polyethylene films using draw ratio and M_n .

In **Chapter 3**, highly thermally-conductive, ultradrawn UHMWPE films containing a low concentration of graphene and a commercial UV absorber are presented. Such ultradrawn composite films show a visible light transmission of $\sim 85\%$ and a metal-like thermal conductivity of $\sim 75 \text{ W m}^{-1} \text{ K}^{-1}$. The high thermal conductivity of these composite films is attributed to the high chain orientation and chain extension of polyethylene and the strong interaction between additives, which opens new possibilities of managing heat transport in windows and devices.

To achieve the high thermal conductivity of drawn polar polymer films and to gain further insight into the mechanism of heat conductivity, drawn polyvinyl alcohol containing graphene oxide and a co-additive interacting via hydrogen bonds are reported in **Chapter 4**. The thermal conductivity of drawn composite films with 5 wt% graphene oxide and 1 % co-

additive is approximately 3-fold higher than that of neatly drawn polyvinyl alcohol films, resulting from the simultaneous orientation of polyvinyl alcohol and graphene oxide and the hydrogen bonds at the interfaces.

Three-dimensional anisotropic polyethylene films with graphene, BZT, and NIR dyes are prepared as light-responsive grippers and diving-surfers in **Chapter 5**. The anisotropic films are cut perpendicular to the film drawing direction and self-bend due to the concentration gradient of additives. Under UV and NIR light illuminations, the films unbend and can act as grippers for grasping cargo. The films can also be driven to dive and ‘surf’ in a solvent under UV or NIR light. In addition, the films can be used as cargo transporters when surfing over the surface of the solvent.

To integrate the negative thermal expansion and high mechanical properties of drawn polyethylene in drawing direction, drawn commodity polyethylene films with graphene, BZT, and NIR dyes as photo-responsive, stress-generating actuators are also demonstrated in **Chapter 6**. Under NIR light illumination, the drawn commodity polyethylene composite films show actuation stresses of approximately 35 MPa with only a change in small strain (< 1%). This actuation stress is also generated under UV and blue light, indicating that the drawn commodity polyethylene films could be used as light-driven metal-like actuators.

Finally, a technology assessment is presented in **Chapter 7**. The low-cost polymers are explored with potential new additives and the possible applications of highly thermal-conductive polymer films in thermal management and light-driven actuators are discussed.

Chapter 1

Introduction

1.1 Introduction

Thermally conductive materials (TCMs) are integrated into electronics, including solar cells, batteries, thermo-electrics, light-emitting diodes, and transistors where heat dissipation impacts the performance and lifetime of the devices.^[1–7] Traditional TCMs such as metals, ceramics, and carbon-based materials exhibit excellent isotropic thermal conductivities. For instance, copper has a thermal conductivity (TC) of ~ 400 W/(m K), silver ~ 430 W/(m K), and graphene ~ 5000 W/(m K) (see **Figure 1.1**).^[3,8,9] However, these high-density TCMs generally are heavy, absorb, reflect or scatter light, and have high electrical conductivity and costs, which limit their application. Traditional TCMs, for instance, require the consumption of more fuel by transports, aircraft, and spacecraft, with the potential of forming electronic short circuits due to their high-density and electrical conductivity. These TCMs are semi-transparent or opaque, which cannot be used in the screens of electronics to release inside heat. For some applications, TCMs with high thermal conductivity, high electrical resistance, low density, low-cost, and/or high transparency are desirable for thermal management.

TCMs based on polymers are attractive due to their low densities, corrosion resistance, high electrical resistance, and ease of processing.^[1,2,5–7,10] However, normal polymers have TCs on the order of only $0.1 \text{ W m}^{-1} \text{ K}^{-1}$ (**Figure 1.1**).^[2,5] The TC of polymers has been increased through the incorporation of thermally conductive additives like graphene,^[8,11–13] carbon nanotubes (CNTs),^[9,14,15] and boron nitride (BN) nanomaterials.^[16–18] In such composites, the mass and/or volume fractions of additives are usually high, typically $\geq 40\%$, achieving TCs on the order of $1 - 10 \text{ W m}^{-1} \text{ K}^{-1}$ (**Figure 1.1**). However, this increase often comes at the expense of higher costs, complex manufacturing processes, and deterioration of the mechanical and optical properties of the polymer composite.^[19]

Anisotropic polymers have been explored over the past few decades because of their tunable, high one-dimensional TC per unit density with corresponding high electrical resistivity (**Figure 1.1**). We will first present basic polymers and methods for generating anisotropy in the materials. Then, thermal conductivity in anisotropic polymers is discussed both from fundamental and experimental viewpoints, including the role of the chemical structure, chain orientation, temperature, and chain length/molecular weight, with a special emphasis on structure-property relationships. Finally, some key challenges and prospects of anisotropic thermally conductive polymeric materials for various applications will be discussed.

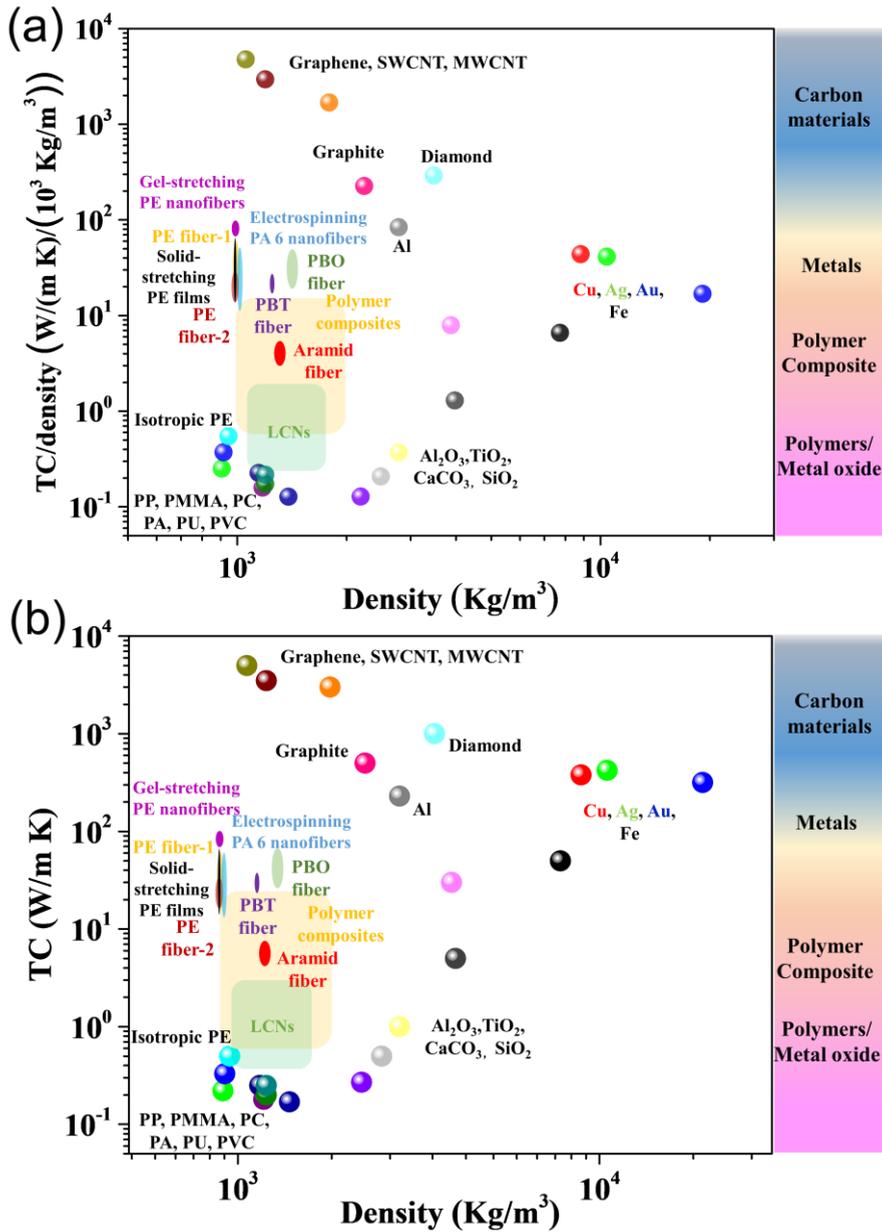


Figure 1.1 (a) Specific and (b) absolute TC of different materials as a function of density. Here, PE: bulk polyethylene, PP: bulk polypropylene, PMMA: bulk poly(methyl methacrylate), PC: bulk polycarbonate, PA 6: polyamide (Nylon 6) fiber, PU: bulk polyurethane, PVC: bulk polyvinyl chloride, PBT fiber: poly p-phenylene benzobisthiazole, Aramid fiber: poly-p-phenylene terephthalamide (Kevlar[®]), PBO fiber: polybenzoxazole (Zylon[®]), SWCNT: single-wall carbon nanotubes, MWCNT: multi-wall carbon nanotubes, Al_2O_3 : aluminum oxide, TiO_2 : titanium dioxide, $CaCO_3$: calcium carbonate, SiO_2 : silicon dioxide, LCNs: liquid crystal networks, PE-1: Dyneema[®] fiber (DSM), and PE-2: Spectra[®] fiber (Honeywell).^[5,8,10,11]

1.2 Achieving anisotropy in polymeric materials

Anisotropy in traditional polymers is typically generated via post-processing (stretching, spinning, or similar techniques), via spinning of lyotropic solutions of rigid polymers, or directly by the alignment of reactive liquid crystal monomers before polymerization (**Figure 1.2**, with the processing of traditional polymers in green and liquid crystal networks in orange).

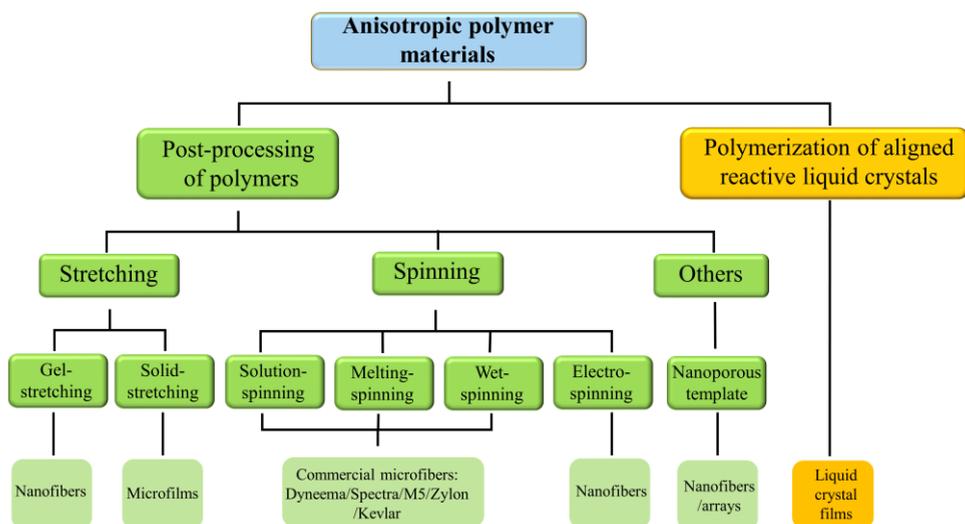


Figure 1.2 Classification of anisotropic polymer materials based on the final fabrication process.

For standard polymers, post-processing (the final fabrication process before achieving anisotropic materials, excluding drying or annealing) can involve solid- or gel-stretching, melting- or solution-spinning, spinning from lyotropic solutions, electrospinning of a solution, or nanoporous template wetting techniques where melted polymers are squeezed through nanopores by, for example, hot gas flow. Such processing results in the extension of individual polymer chains along one direction, increasing crystallinity, and the shrinkage of amorphous regions in the polymer. Polymers that have been made anisotropic with post-processing include drawn polyethylene (PE) films, micro- and nano-fibers, polyamide nanofibers, polybenzoxazole fibers (PBO, Zylon[®]), poly-p-phenylene terephthalamide fibers (Kevlar[®]), polyhydroquinone diimidazopyridine fibers (PIPD), and poly p-phenylene benzobisthiazole (PBT) microfibers. These polymer films and fibers often exhibit extremely high orientation, crystallinity, corrosion resistance, and specific strength per unit density, and sometimes even high visible light transmission, all of which are indicators that these films or

fibers have the potential of high TC. Also, some commercial fibers, like PBO, PBT, and PE fibers, have high-moduli,¹⁰ which are used widely in industry and daily life.

Due to the high TC of nanomaterial fillers such as graphene,^[8,13,20,21] CNTs,^[5,9] and BN^[16-18], drawn composites of these nano-fillers in highly-aligning matrix hosts have the potential to achieve much higher TC than isotropic composites. However, poor interaction between fillers and matrix often causes serious phonon scattering at interfaces,^[22-24] resulting in low thermal transport and/or light transmission, even in drawn composites at high draw ratios.

First aligning reactive liquid crystal (LC) monomers and subsequently photopolymerizing them yield anisotropic LC network (LCN) films.^[25-31] Alignment of the LC is possible by using rubbed surfaces, photo-alignment layers, flow fields, and/or electrical or magnetic fields.^[25-31] In addition, enhanced alignment can be achieved by exploiting the different LC phases, which include nematic, chiral nematic, smectic, and columnar (discotic) nematic phases, all of which vary in the intermolecular alignments and orientations and degrees of molecular anisotropy, with the specific phase trapped in the LCN film dependent on the polymerization temperature. In a discotic nematic phase, the discotic molecules possess full translational and rotational freedom around their short molecular axis (disc normal).^[32] Generally, the degree of orientation of planar LCNs is described by the order parameter^[33] and/or Herman's orientation function.^[34] The order parameter, S , is generally described by the equation $S = \frac{A_{par} - A_{per}}{A_{par} + 2A_{per}}$, where A_{par} and A_{per} are the absorbance of light polarized parallel and perpendicular to the alignment of the monomers, respectively. For perfectly aligned LCs, S is 1, while $S = 0$ represents a random, isotropic phase. S is dictated by the chemical nature of the reactive LC and on the LC phase. In the case of smectic phases, for example, which have greater positional and orientational order than the nematic phase, the S can be relatively high.^[35]

Various anisotropic polymers and their composites are fabricated through the above-mentioned methods, presenting high crystallinity and chain orientation, and achieving high thermal conductivity. However, there is a large difference in crystallinity, chain orientation, and intermolecular interaction, resulting in different TC, which will be discussed below in detail.

1.3 Thermal transport in anisotropic polymer materials

The theory of thermal transport in crystals and glasses has been developed over many years, including the Debye model, Cahill-Pohl/Einstein model, Boltzmann transport model, Allen-Feldman model, and their modified forms, by empirical methods or measuring crystalline and amorphous silicon.^[36-40] For instance, the Cahill-Pohl/Einstein model of minimum phonon thermal conductivity is widely successful as the lower limit for fully dense amorphous and disordered materials.^[40] The Boltzmann transport model and Allen-

Feldman's model are also used to describe the low heat conduction of silicon and thermoelectric materials based on first-principles simulations from physics.^[37,38] It is generally assumed that heat transport in solid insulators, either crystalline or disordered, is dominated by the dynamics of lattice vibrations (phonon).^[38]

To easily and directly represent the relationship between thermal transport and chemical structure, we consider the Debye model, even though it is simple and empirical. The thermal transport in isotropic polymers is dominated by phonon scattering, which can be roughly described by the Debye equation,

$$\kappa = (C_p v l)/3 \quad (1.1)$$

where κ is the thermal conductivity and C_p is the specific heat capacity of the polymer, v is the phonon velocity, and l is the mean free path of phonon transport. In most polymers, l is rather short due to the strong phonon scattering caused by defects or voids, grain boundaries, and interaction with other phonons, leading to the generally low TC of unaligned polymers.^[1] Similarly, interfaces and/or gaps between additives and matrix lead to strong phonon scattering in polymer composites.^[1] Thus, to achieve high TC, anisotropic polymers must decrease the phonon scattering.

In anisotropic polymers, the thermal conductivity is also anisotropic and, therefore, should be represented by a matrix in which all components are represented in three dimensions. To describe thermal transport in anisotropic polymers, theoretical models must include factors related to the chemical structure of polymers, including chain length, number and branching of side chains, and intermolecular interactions.^[41-47] Simulations predict that the maximum TC of a single polyethylene (PE) chain, one of the simplest polymer structures imaginable, is up to $350 \text{ W m}^{-1} \text{ K}^{-1}$ when the chain length is more than $1 \mu\text{m}$. This theoretical value for a single polyethylene chain is several orders of magnitude larger than the values of bulk PE and increases with respect to chain length (L) (**Figure 1.3a**).^[43] Similar phenomena are observed in other polymer chains, including poly(p-phenylene), poly(methylene oxide), poly(ethylene oxide), and poly(phenylene ether). In these cases, the logarithmic TC ($\log_{10}TC$) increased linearly with the logarithmic chain length ($\text{Log}_{10}L$) (**Figure 1.3b**).^[41,44] The slope (β) of a plot of $\log_{10}TC$ against $\text{Log}_{10}L$ indicates the competition between diffusive (scattering) and ballistic (quantized thermal resistance independent of length) phonon transport: predominantly ballistic phonon transport leads to $\beta = 1$, while predominantly diffusive phonon transport leads to $\beta = 0$.^[44] The different β and TC of polymer chains give indications of the effects on thermal transport of bond-strength/mass disorder and interaction between molecules (**Figure 1.3c**).^[44] Additionally, it found that there is an interchain distance-dependent TC in isotropic polymers, revealing the mechanism of different TC in various

polymers and the positive effect of entanglement.^[48] However, the interchain distance-dependent TC is negligible in oriented polymers because the TC of oriented polymers is dominated by the intrinsic TC of molecular chains.^[48] Furthermore, the entanglements in anisotropic polymers are negative to chain orientation during stretching.

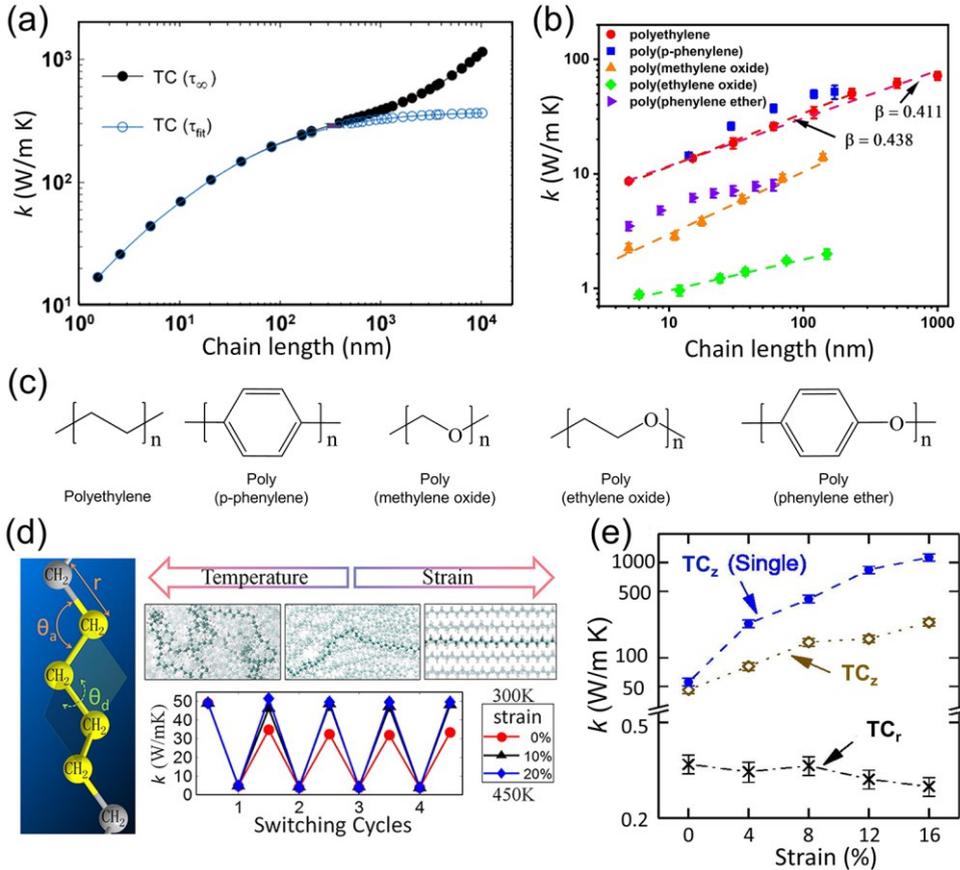


Figure 1.3 (a) Simulated TC of a PE chain as a function of chain length (Reprinted with permission.^[43] Copyright 2008, American Physical Society). τ is the relaxation time in the simulation. (b) TC of different polymers as a function of chain length. The dashed lines are fits of the data. The slope β indicates the competition between diffusive and ballistic phonon transports. (Reprinted with permission.^[44] Copyright 2012, American Physical Society) (c) Chemical structures of polymers. (d) Illustration of temperature and strain-dependent TC of a PE chain (Reproduced with permission.^[47] Copyright 2013, American Chemical Society). (e) TC of PE chain and PE crystalline in directions parallel (TC_z) and perpendicular (TC_r) to the main chain extension as a function of strain. (Reprinted with permission.^[45] Copyright 2018, American Physical Society)

Simple, single PE chains with the zig-zag structure seen in **Figure 1.3d** show a switchable TC, undergoing a temperature-induced phase transition from the crystalline state at 300 K to an amorphous state at 450 K due to the different degrees of segmental order of the flexible -CH₂ segments along the polyethylene chains, induced either by strain or temperature.^[47] As a result, the TC increases with strain due to the higher degree of orientation of the PE chain. As mentioned previously, the presence of side-chains and the interaction between polymer chains also affect thermal transport. Normally, heavy and dense side-chains have a negative contribution to thermal transport.^[46] On the other hand, strong intermolecular interactions, like hydrogen bonding and π interactions can decrease phonon scattering, leading to higher thermal conductivity. Furthermore, the TC_r in the x- and y-directions (perpendicular to the chain extension direction) of PE films decrease slightly while the TC_z in the chain direction increases upon the increasing strain (**Figure 1.3e**).^[45] The decreasing TC_r in the crystalline PE films is attributed to the decreasing intermolecular van der Waals (vdW) interactions with the increasing strain which enhances phonon scattering for inter-chain phonon transport.^[42,45,48]

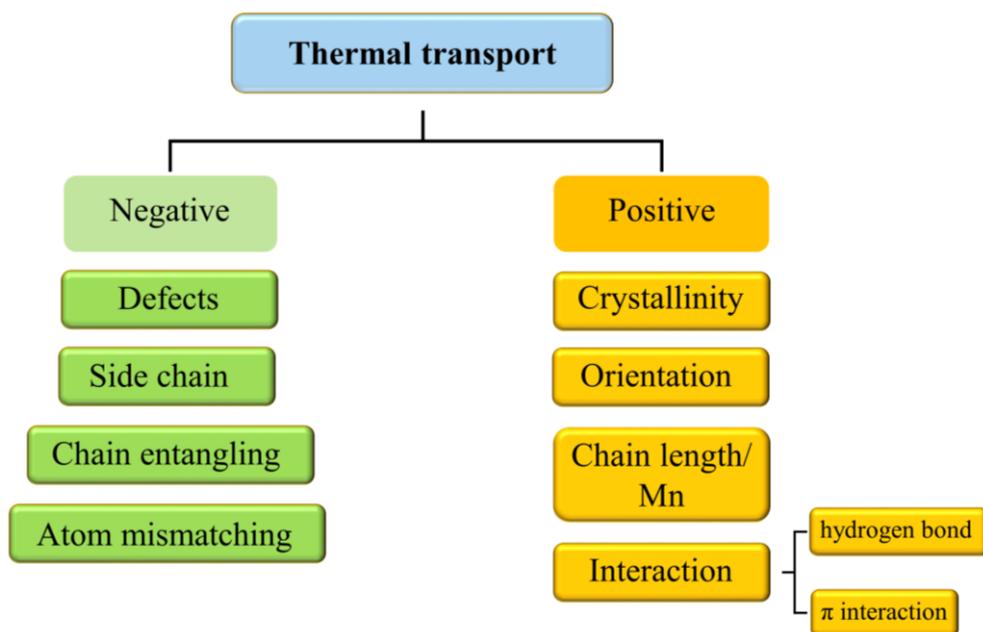


Figure 1.4 Effects of microstructure on thermal transport in anisotropic polymers.

The factors affecting thermal transport are summarized in **Figure 1.4** based on the results of computer simulations. For instance, the defects, side chain (branch), and atom

mismatching in the main chain increase the phonon scattering, decreasing TC.^[41,44,46] Chain entanglement is beneficial to the thermal transport in isotropic polymers; however, it is a negative factor for anisotropic polymers owing to the decreasing chain orientation and/or draw ratio induced by chain entanglement. On the other hand, chain orientation, crystallinity, and draw ratio are supposed to enhance the thermal transport and increase TC in anisotropic polymers, which is consistent with the effect of chain length (molecular weight). More importantly, the interaction between fillers and matrix is positive to TC^[44] due to the decreasing thermal resistivity in the interfaces and boundaries.

1.4 Thermal conductivity of anisotropic polymer materials

1.4.1 Thermal conductivity of polymers with post-processing

1.4.1.1 PE nanofibers fabricated by gel-stretching

Stretched PE fibers can present much higher TC than in the unstretched state due to their high crystallinity and main chain orientation induced by the ultra-stretchability (draw ratio > 100) and their simple chemical structure without atom mismatches to cause scattering.^{1,3-5,18-30} The TC of a high-quality 100-200 nm diameter gel-stretched PE nanofibers with draw ratios of ~ 400 was found to be as high as $\sim 104 \text{ W m}^{-1} \text{ K}^{-1}$,^[49] larger than the thermal conductivities of about half of the pure metals, including nickel, iron, and platinum. Remarkably, this value is about three times higher than previously reported for PE microfibrils^[50] and ~ 300 times higher than that of isotropic polyethylene (**Figure 1.5a**).^[49] Similarly, the ultra-drawn PE nanofibers had diameters of approximately 100 nm and showed extremely high strength and temperature-dependent TC (**Figure 1.5b** and **c**).^[51] Such temperature-dependent TC increases linearly as $\sim T$ from 20 to 100 K, reaching a plateau of $\sim 90 \text{ W m}^{-1} \text{ K}^{-1}$.^[51] In addition to high thermal conductivity, such PE nanofibers exhibit ultra-high strength (11 GPa) as well, exceeding any other existing soft materials.^[51] These results are explained by the high degree of chain orientation and reduction of the periodic boundary phonon scattering.^[42,49]

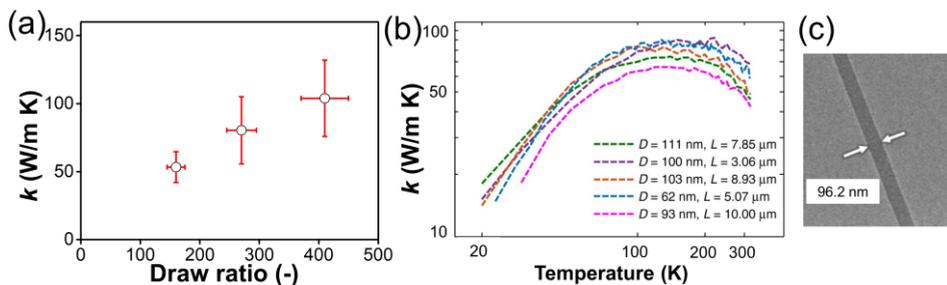


Figure 1.5 (a) TC of ultradrawn PE nanofibers as a function of draw ratio.^[49] (b) TC of ultradrawn PE nanofibers with different diameters (D) and length (L) as a function of temperature. (c) TEM micrograph of a PE nanofiber. (Reprinted with permission.^[51] Copyright 2018, Nature)

1.4.1.2 PE microfilms fabricated by solid-stretching

Although ultra-drawn PE films possess similar crystallinity and chain orientation to ultra-drawn PE fibers, ultra-drawn PE films have other potential uses due to their larger surface areas, high visible light transmissions, and relative ease of processing.^[55] Drawn PE films fabricated by solution-extrusion and solid-drawing methods show increasing in-plane parallel TC with increased draw ratios, the maximum of TC measured being approximately $62 \text{ W m}^{-1} \text{ K}^{-1}$ with a draw ratio of 110 using the steady-state method (**Figure 1.6a**).^[52] Similarly, ultra-drawn PE films achieved by multi-stage drawing in the solid-state produce a TC of $65 \text{ W m}^{-1} \text{ K}^{-1}$ at a draw ratio of 410 (**Figure 1.6b**).^[54] The tiny difference of TC in ultra-drawn PE films could be attributed to different crystallinity or chain orientation induced by the pre-process of PE films before stretching.

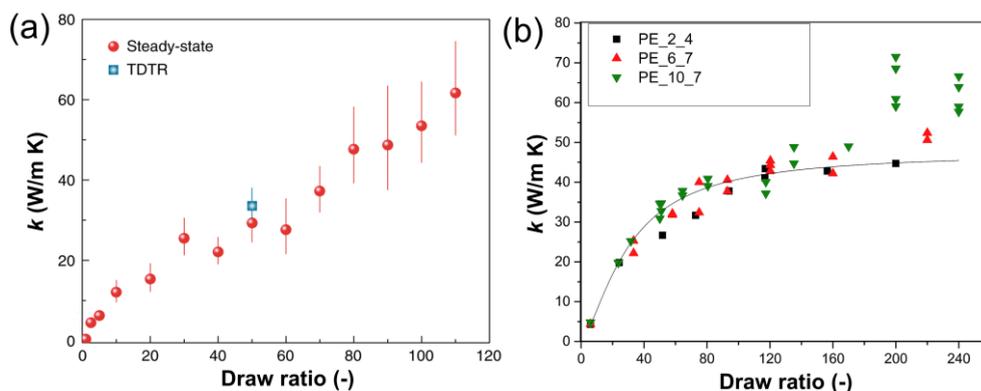


Figure 1.6 (a) TC of ultradrawn PE films as a function of draw ratios (Reprinted with permission.^[52] Copyright 2019, Nature). Here, TDTR represents the time-domain thermal reflection method.^[53] (b) TC of ultradrawn PE films with different molecular weights as a function of draw ratio (Reprinted with permission.^[54] Copyright 2017, Elsevier B.V.). PE_2_4, PE_6_7, and PE_10_7 represent PE films with weight-average molecular weights (M_w) of 2000, 6000, and 10000 kg/mol and molecular weight distribution of 4, 7, and 7, respectively.

1.4.1.3 Commercial microfibers fabricated by the wet-/solution-/melting-spinning process

Highly-oriented polymer fibers with strong interchain interactions have the potential to be excellent thermal conductors.^[10,56-59] For instance, the commercial fibers polybenzoxazoles (PBO, brand name Zylon[®]), poly p-phenyleneterephthamide (Aramid, Kevlar[®] 149), polyhydroquinone diimidazopyridine (PIPD), (poly(p-phenylene benzobisthiazole)) (PBT), and polyethylene (brand names Dyneema[®] and Spectra[®]) not only exhibit high tensile moduli but also high TCs (**Figure 1.7a**), higher than most isotropic polymers and ceramics.^[49] Commercial PE microfibers show a temperature-dependent TC

from 50 to 250 K, usually lower than that of PE nanofibers (**Figure 1.7b**),^[49] a result of their relatively low degree of chain orientation and stronger periodic boundary phonon scattering.^[42] As mentioned above, anisotropic PE films and fibers fabricated by different processes can show a large difference in thermal conductivity, which is mainly attributed to the different chain orientations (draw ratios) induced by the fabrication process. Usually, the PE nanofibers^[49] fabricated by gel-stretching show greater chain orientation (draw ratios) than PE microfilms and PE fibers achieved by other methods,^[52] and the PE microfilms could possess stronger periodic boundary phonon scattering than PE microfibers.^[42]

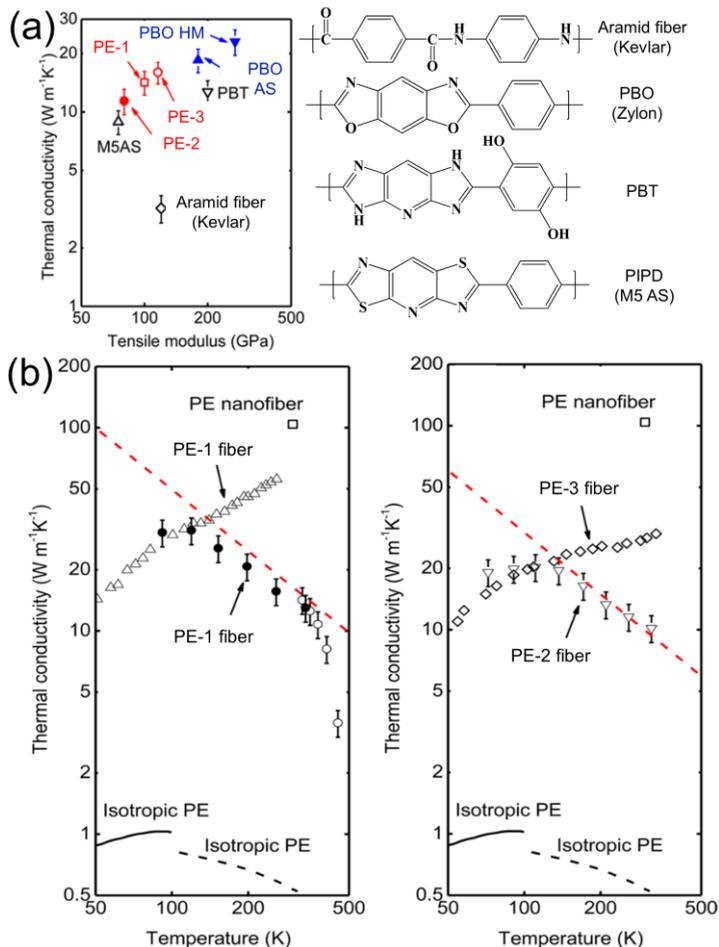


Figure 1.7 (a) TC of commercial PBO, PE (PE-1: Dyneema[®] fiber, PE-2, and PE-3: Spectra[®] 900 and 2000 fibers), Aramid[®], PIPD, and PBT fibers as a function of tensile moduli and their chemical structures. The diameters of the fibers range from 10 to 30 μm . (b) TC of the same polymer fibers as a function of temperature. (Reproduced with permission.^[10] Copyright 2013, American Chemical Society)

1.4.1.4 Nanofibers fabricated by nanoporous template wetting/electrospinning

A PE nanofiber array fabricated by nanoporous template wetting had a maximum TC ($14.8 \text{ W m}^{-1} \text{ K}^{-1}$) with a diameter of 100 nm, approximately 30 times greater than the TC of bulk PE (**Figure 1.8a**).^[60] The single PE nanofibers in this array have an estimated TC slightly more than $20 \text{ W m}^{-1} \text{ K}^{-1}$ at room temperature, however, this value is considerably lower than that of gel-stretched PE nanofibers ($\sim 104 \text{ W m}^{-1} \text{ K}^{-1}$)^[62] probably due to the relatively low orientation in PE nanofiber array. Pure polythiophene (PT) nanofibers fabricated by electropolymerization using nanoscale templates display a TC of $\sim 4.4 \text{ W m}^{-1} \text{ K}^{-1}$, over 20 times greater than bulk PT.^[56] This remarkable result is attributed to the enhanced chain orientation along the fiber axis obtained during electropolymerization.^[56] PE nanofibers fabricated by electrospinning show an increasing TC with increasing electrospinning voltage (**Figure 1.8b**),^[61] this increase attributable to the increase in crystallinity induced by the higher voltages. Over the temperature range of 100 to $\sim 270 \text{ K}$, the TC of the PE nanofibers increases: further temperature increase results in TC decay as a result of increasing phonon scattering.^[61] The semi-crystalline Nylon nanofibers fabricated by electrospinning exhibit a large, annealing time-dependent TC of $59.1 \text{ W m}^{-1} \text{ K}^{-1}$ due to the reduced configuration disorder after annealing, approximately 3 orders of magnitude higher than that of pristine Nylon nanofibers (**Figure 1.8c and d**).^[59]

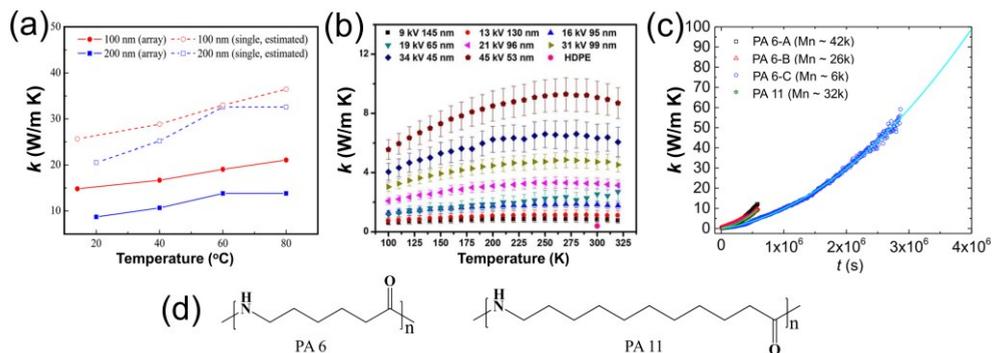


Figure 1.8 (a) TC of PE nanofiber arrays fabricated by nanoporous template wetting and the estimated TC of single fibers as a function of temperature. (Reprinted with permission.^[60] Copyright 2011, Elsevier B.V.) (b) TC of PE nanofibers with different electrospinning voltages and diameters as a function of temperature. (Reproduced with permission.^[61] Copyright 2015, Royal Science of Chemistry) (c) TC of polyamide 6 (PA 6, Nylon 6) and polyamide 11 (PA 11, Nylon 11) with different Mn as a function of annealing time. (Reproduced with permission.^[59] Copyright 2020, American Chemical Society) (d) Chemical structures of PA6 and PA11 fibers.

1.4.2 Thermal conductivity of liquid crystal networks

Photopolymerized LCNs exhibit anisotropic properties, including thermal conductivity due to the anisotropic intermolecular-interaction and chain orientation.^[63,64] As a result of the conjugated and extended π -system of the mesogenic core and length extension of the terminal aliphatic tails, the through-plane TC and the TC anisotropy ratio of LC polymer films reach $3.56 \text{ W m}^{-1} \text{ K}^{-1}$ and 15, respectively.^[63] Similarly, discotic LC (DLC) films prepared by thermal treatment and photo-crosslinking exhibit increased in-plane TC ($3.8 \text{ W m}^{-1} \text{ K}^{-1}$) and anisotropy ratios (~ 38) resulting from the homeotropic alignment and high crosslinking density.^[64] These values for the TC are low in comparison to other anisotropic systems, such as anisotropic PE films and fibers^[51,52] due to the side chains and atomic mismatches in molecules, and a lower degree of orientation of LCNs. LC films incorporating photoisomers can be designed with properties that are tunable using external stimuli, including engineering variation in their TCs, visible light transmission, and actuation capability.^[64–69] Typically, to achieve these responsive properties, the polymers are created from LCs doped with azobenzene (**Figure 1.9**).^[69] Azobenzene is a photoisomer that can change from the extended *trans*- form to the bent *cis*-isomer upon exposure to UV light and can be returned to the *trans* form by exposure to longer wavelengths, such as blue light (see **Figure 1.9a**).^[69] The TC of polymers doped with azobenzene is tunable: when the azobenzene transfers from planar (*trans*) to nonplanar (*cis*) states under UV illumination, the TC ($\lambda_{trans}/\lambda_{cis}$) varies up to a factor of 3.5 (**Figure 1.9b**), a higher anisotropy ratio of TC than found in other responsive materials.^[70–72] Although the thermal conductivity is low, these results indicate that LCN films could potentially be used to fabricate remote-controlled, switchable TCM ‘smart’ materials.

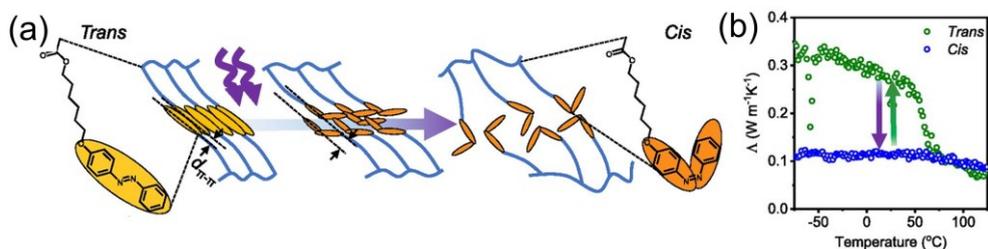


Figure 1.9 (a) Schematic diagram of the structural transition in azobenzene polymers from the *trans* to *cis* states under UV light stimuli. (b) TC of azobenzene polymers in *trans* and *cis* states. (Reprinted with permission.^[69] Copyright 2019, National Academy of Sciences)

1.4.3 Thermal conductivity of anisotropic polymer composites

As mentioned in section 1.2, poor interaction between fillers and their matrix can result in serious phonon scattering at interfaces in anisotropic polymer composites,^[22–24] resulting in low TC. Therefore, drawn composites with strong interaction between filler and matrix or with a low draw ratio have been produced to good effect.^[73–76] The TCs of DLC were studied with different volumetric amounts of expanded graphite (EG) or BN (**Figure 1.10a** and **b**).^[77] As expected, the TCs of both composites were enhanced with increasing volumetric quantity of fillers, based on both theoretical calculations and experimental measurements (**Figure 1.10 c** and **d**). The DLC-EG composite exhibited a higher TC than the DLC-BN composite at the same volumetric content, although pure BN shows a higher TC than EG. This work revealed good interfacial affinity between EG and DLC, resulting in suppressed interfacial phonon scattering by the strong π - π interactions, while BN instead interacts with DLC through weaker vdW forces (**Figure 1.10b**).

The effect of the simultaneous alignment of PE lamellae and graphene (GN) on the TC of their composites was investigated at low draw ratios (< 5).^[74] It found the TC of drawn PE-GN composite increases upon increasing content of GN and increasing draw ratios: the weak vdW interactions between GN and PE chains suggest simultaneous alignment has great potential to achieve high TC in the drawn polymer composites.

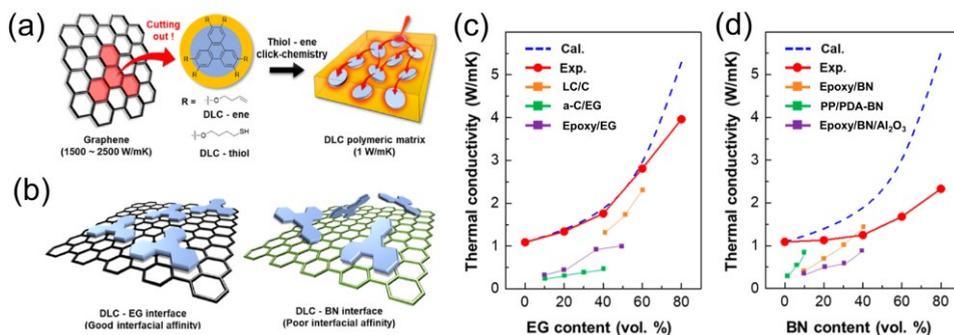


Figure 1.10 (a and b) Schematic diagram of the fabrication and interaction of DLC-GN and DLC-BN. (c and d) TC of DLC composites film with expanded graphene and BN as a function of volume content of additives. (Reproduced with permission.⁷⁹ Copyright 2018, American Chemical Society) LC/C (liquid crystals with carbon black),^[78] a-C/EG (activated carbon powder with expanded graphite),^[79] Epoxy/EG (epoxy with expanded graphite),^[80] Epoxy/BN (epoxy with boron nitride),^[81] PP/PDA-BN (polypropylene with polydopamine-functionalized boron nitride),^[82] Epoxy/BN/Al₂O₃ (epoxy with boron nitride and aluminum oxide)^[83]

1.5 Research aim and outline of the thesis

Commodity polymers, including polyethylene, polystyrene, and polypropylene, are widely used in daily life and at large scales. These low-density, low-cost polymers typically only exhibit low thermal conductivity and static functional properties, limiting their application as high-end products. In this thesis, drawn polyethylene, polyvinyl alcohol, and their composites films as high thermal conductors are explored. Furthermore, the application of these thermally conductive polymers as photothermal soft actuators is investigated.

Chapter 2 describes ultradrawn films of ultra-high molecular weight polyethylene (UHMWPE) blended with a wide range of low molecular weight poly waxes which exhibit number average-molecular weight (M_n) dependent thermal conductivities. A new model correlating molecular weight, draw ratio and thermal conductivity is presented and validated against the experimental results. Through this model, there is new potential for designing drawn polymers with high thermal conductivity using draw ratio and M_n .

To solve the weak interaction between drawn polymer matrixes and additives, a highly thermally-conductive ultradrawn UHMWPE film containing a low concentration of graphene and a commercial UV absorber (BZT) was explored in **Chapter 3**. Such ultradrawn composite films show a visible light transmission of $\sim 85\%$ and a metal-like thermal conductivity of $\sim 75 \text{ W m}^{-1} \text{ K}^{-1}$, which opens new possibilities of managing heat transport in windows and devices.

The effect of interaction between matrix and additive on thermal conductivity was studied in **Chapter 4** using drawn polyvinyl alcohol and graphene oxide composite films. The thermal conductivity of drawn composite films with 5 wt% graphene oxide is approximately 50-fold higher than that of neat undrawn polyvinyl alcohol films.

Chapter 5 demonstrates the use of a three-dimensional anisotropic commodity polyethylene film containing graphene, BZT, and near-infrared absorbing dyes as light-responsive actuators. The soft actuators are cut perpendicular to the film drawing direction and self-bend due to the concentration gradient of additives. Under UV and NIR light illuminations, the films unbend and can act as a gripper for grasping cargo. The films can also be driven to dive and 'surf' in isopropanol under UV or NIR lights. In addition, the films may be used as a cargo transporter when it is surfing on the surface of a solvent. This work demonstrates that commodity polymers can be used as soft actuators and robotic devices and the high thermal conductivity of composite films is able to improve the response time of photoresponsive actuators.

To integrate the negative thermal expansion and high mechanical properties in the drawing direction, **Chapter 6** reports drawn commodity polyethylene films with graphene, BZT, and NIR dyes as photo-responsive, stress-generating actuators. Under NIR light illumination, the drawn commodity polyethylene composite films show actuation stresses of

Chapter 1

approximately 35 MPa with only a change in small strain ($< 1\%$). This actuation stress is also generated under UV and blue lights, indicating that the drawn commodity polyethylene films could be used as light-driven metal-like actuators.

Chapter 7 provides the assessment of the results in this thesis and the potential applications of the low-cost commodity polymers as high thermal conductive polymer materials for thermal management, and soft actuators.

1.6 References

- [1] H. Chen, V. V. Ginzburg, J. Yang, Y. Yang, W. Liu, Y. Huang, L. Du, B. Chen, *Prog Polym Sci* **2016**, *59*, 41.
- [2] C. Huang, X. Qian, R. Yang, *Mater Sci Eng R Reports* **2018**, *132*, 1.
- [3] Y. Zhang, Y. J. Heo, Y. R. Son, I. In, K. H. An, B. J. Kim, S. J. Park, *Carbon* **2019**, *142*, 445.
- [4] A. Shanker, C. Li, G. Kim, D. Gidley, K. P. Pipe, J. Kim, *Sci Adv* **2017**, *3*, 1700342.
- [5] Z. Han, A. Fina, *Prog Polym Sci* **2011**, *36*, 914.
- [6] X. Xu, J. Chen, J. Zhou, B. Li, *Adv Mater* **2018**, *30*, 1705544.
- [7] X. Xu, J. Zhou, J. Chen, *Adv Funct Mater* **2019**, *10*, 1904704.
- [8] A. A. Balandin, S. Ghosh, W. Bao, I. Calizo, *Nano Lett* **2008**, *8*, 902.
- [9] S. Berber, Y.-K. Kwon, D. Tomanek, *Phys Rev Lett* **2000**, *84*, 4613.
- [10] X. Wang, V. Ho, R. A. Segalman, D. G. Cahill, *Macromolecules* **2013**, *46*, 4937.
- [11] S. Ghosh, W. Bao, D. L. Nika, S. Subrina, E. P. Pokatilov, C. N. Lau, A. A. Balandin, *Nat Mater* **2010**, *9*, 555.
- [12] R. Balog, B. Jørgensen, L. Nilsson, M. Andersen, E. Rienks, M. Bianchi, M. Fanetti, E. Lægsgaard, A. Baraldi, S. Lizzit, Z. Slijivancanin, F. Besenbacher, B. Hammer, T. G. Pedersen, P. Hofmann, L. Hornekær, *Nat Mater* **2010**, *9*, 315.
- [13] M. Mu, C. Wan, T. McNally, *2D Mater* **2017**, *4*, 042001.
- [14] M. Fujii, X. Zhang, H. Xie, H. Ago, K. Takahashi, T. Ikuta, H. Abe, T. Shimizu, *Phys Rev Lett* **2005**, *95*, 8.
- [15] H. Y. Chiu, V. V. Deshpande, H. W. C. Postma, C. N. Lau, C. Mikó, L. Forró, M. Bockrath, *Phys Rev Lett* **2005**, *95*, 226101.
- [16] V. Guerra, C. Wan, T. McNally, *Prog Mater Sci* **2019**, *100*, 170.
- [17] C. W. Chang, A. M. Fennimore, A. Afanasiev, D. Okawa, T. Ikuno, H. Garcia, D. Li, A. Majumdar, A. Zettl, *Phys Rev Lett* **2006**, *97*, 085901.
- [18] K. Chen, B. Song, N. K. Ravichandran, Q. Zheng, X. Chen, H. Lee, H. Sun, S. Li, G. A. G. U. Gamage, F. Tian, Z. Ding, Q. Song, A. Rai, H. Wu, P. Koirala, A. J. Schmidt, K. Watanabe, B. Lv, Z. Ren, L. Shi, D. G. Cahill, T. Taniguchi, D. Broido, G. Chen, *Science* **2020**, *367*, 555.
- [19] R. C. Zhang, Z. Huang, D. Sun, D. Ji, M. Zhong, D. Zang, J. Z. Xu, Y. Wan, A. Lu, *Polymer* **2018**, *154*, 42.
- [20] Y. Xu, Z. Li, W. Duan, *Small* **2014**, *10*, 2182.
- [21] M. Allen, *Chem Rev* **2010**, *110*, 132.
- [22] J. R. Gissinger, C. Pramanik, B. Newcomb, S. Kumar, H. Heinz, *ACS Appl Mater Interfaces* **2018**, *10*, 1017.
- [23] S. J. V. Frankland, V. M. Harik, G. M. Odegard, D. W. Brenner, T. S. Gates, *Compos Sci Technol* **2003**, *63*, 1655.
- [24] S. Herasati, L. C. Zhang, H. H. Ruan, *Int J Solids Struct* **2014**, *51*, 1781.
- [25] J. Xie, G. Zhu, Y. Tang, Y. Wang, *Liq Cryst* **2014**, *41*, 36.
- [26] O. G. Mamack. Marc, Coombs. Neil, *Adv Mater* **2000**, *12*, 167.
- [27] V. David, Coats Owain, Parri Mark, *J Chem Inf Model* **2019**, *53*, 1689.
- [28] O. Yaroshchuk, Y. Reznikov, *J Mater Chem* **2012**, *22*, 286.

Chapter 1

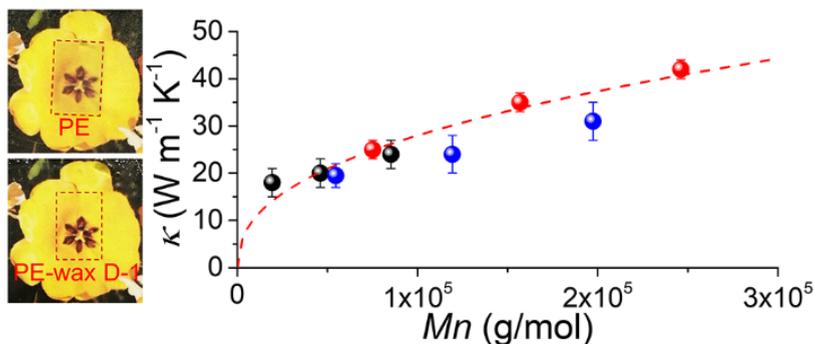
- [29] C. Sánchez, B. Villacampa, R. Alcalá, C. Martínez, L. Oriol, M. Piñol, J. L. Serrano, *Chem Mater* **1999**, *11*, 2804.
- [30] R. J. Bushby, K. Kawata, *Liq Cryst* **2011**, *38*, 1415.
- [31] K. Robbie, D. J. Broer, M. J. Brett, *Nature* **1999**, *399*, 764.
- [32] H. K. Bisoyi, Q. Li, *Chem Rev* **2016**, *116*, 15089.
- [33] K. H. Fischer, J. A. Hertz, *J Phys C Solid State Phys* **1983**, *16*, 5017.
- [34] J. J. Hermans P. H. Hermans D. Vermaas A. Weidinger, *Recl des Trav Chim des Pays-Bas banner* **1946**, *65*, 427.
- [35] J. D. Brock, A. Aharony, R. J. Birgeneau, K. W. Evans-Lutterodt, J. D. Litster, P. M. Horn, G. B. Stephenson, A. R. Tajbakhsh, *Phys Rev Lett* **1986**, *57*, 98.
- [36] C. Jeong, S. Datta, M. Lundstrom, *J Appl Phys* **2011**, *109*, 073718.
- [37] M. Simoncelli, N. Marzari, F. Mauri, *Nat Phys* **2019**, *15*, 809.
- [38] L. Isaeva, G. Barbalinardo, D. Donadio, S. Baroni, *Nat Commun* **2019**, *10*, 1.
- [39] R. Peierls, *Ann Phys* **1914**, *395*, 1055.
- [40] D. G. Cahill, S. K. Watson, R. O. Pohl, *Phys Rev B* **1992**, *46*, 6131.
- [41] X. Duan, Z. Li, J. Liu, G. Chen, X. Li, *J Appl Phys* **2019**, *125*, 164303.
- [42] A. Henry, G. Chen, S. J. Plimpton, A. Thompson, *Phys Rev B* **2010**, *82*, 144308.
- [43] A. Henry, G. Chen, *Phys Rev Lett* **2008**, *101*, 23502.
- [44] J. Liu, R. Yang, *Phys Rev B* **2012**, *86*, 104307.
- [45] J. He, K. Kim, Y. Wang, J. Liu, *Appl Phys Lett* **2018**, *112*, 051907.
- [46] D. Luo, C. Huang, Z. Huang, *J Heat Transfer* **2017**, *140*, 031302.
- [47] T. Zhang, T. Luo, *ACS Nano* **2013**, *7*, 7592.
- [48] J. Zhou, Q. Xi, J. He, X. Xu, T. Nakayama, Y. Wang, J. Liu, *Phys Rev Mater* **2019**, *4*, 015601.
- [49] S. Shen, A. Henry, J. Tong, R. Zheng, G. Chen, *Nat Nanotechnol* **2010**, *5*, 251.
- [50] C. L. Choy, Y. W. Wong, G. W. Yang, T. Kanamoto, *J Polym Sci Part B Polym Phys* **1999**, *37*, 3359.
- [51] R. Shrestha, P. Li, B. Chatterjee, T. Zheng, X. Wu, Z. Liu, T. Luo, S. Choi, K. Hippalgaonkar, M. P. De Boer, S. Shen, *Nat Commun* **2018**, *9*, 1664.
- [52] Y. Xu, D. Kraemer, B. Song, Z. Jiang, J. Zhou, J. Loomis, J. Wang, M. Li, H. Ghasemi, X. Huang, X. Li, G. Chen, *Nat Commun* **2019**, *10*, 1771.
- [53] A. Palacios, L. Cong, M. E. Navarro, Y. Ding, C. Barreneche, *Renew Sustain Energy Rev* **2019**, *108*, 32.
- [54] S. Ronca, T. Igarashi, G. Forte, S. Rastogi, *Polym* **2017**, *123*, 203.
- [55] B. Zhu, J. Liu, T. Wang, M. Han, S. Valloppilly, S. Xu, X. Wang, *ACS Omega* **2017**, *2*, 3931.
- [56] V. Singh, T. L. Bougher, A. Weathers, Y. Cai, K. Bi, M. T. Pettes, S. A. McMenamin, W. Lv, D. P. Resler, T. R. Gattuso, D. H. Altman, K. H. Sandhage, L. Shi, A. Henry, B. A. Cola, *Nat Nanotechnol* **2014**, *9*, 384.
- [57] Y. Park, M. You, J. Shin, S. Ha, D. Kim, M. H. Heo, J. Nah, Y. A. Kim, J. H. Seol, *Sci Rep* **2019**, *9*, 3026.
- [58] W. Zhao, J. Kong, H. Liu, Q. Zhuang, J. Gu, Z. Guo, *Nanoscale* **2016**, *8*, 19984.
- [59] H. C. Chien, W. T. Peng, T. H. Chiu, P. H. Wu, Y. J. Liu, C. W. Tu, C. L. Wang, M. C. Lu, *ACS Nano* **2020**, *14*, 2939.
- [60] B. Y. Cao, Y. W. Li, J. Kong, H. Chen, Y. Xu, K. L. Yung, A. Cai, *Polymer* **2011**, *52*, 1711.
- [61] J. Ma, Q. Zhang, A. Mayo, Z. Ni, H. Yi, Y. Chen, R. Mu, L. M. Bellan, D. Li, *Nanoscale* **2015**, *7*, 16899.

- [62] S. Shen, A. Henry, J. Tong, R. Zheng, G. Chen, *Nat Nanotechnol* **2010**, *5*, 251.
- [63] S. J. Ge, T. P. Zhao, M. Wang, L. L. Deng, B. P. Lin, X. Q. Zhang, Y. Sun, H. Yang, E. Q. Chen, *Soft Matter* **2017**, *13*, 5463.
- [64] D. G. Kim, Y. H. Kim, T. J. Shin, E. J. Cha, D. S. Kim, B. G. Kim, Y. Yoo, Y. S. Kim, M. H. Yi, J. C. Won, *Chem Commun* **2017**, *53*, 8227.
- [65] E. C. Davidson, A. Kotikian, S. Li, J. Aizenberg, J. A. Lewis, *Adv Mater* **2019**, *32*, 1905682.
- [66] R. Lan, J. Sun, C. Shen, R. Huang, Z. Zhang, L. Zhang, *Adv Mater* **2020**, *32*, 1906319.
- [67] K. Kumar, A. P. H. J. Schenning, D. J. Broer, D. Liu, *Soft Matter* **2016**, *12*, 3196.
- [68] E. P. A. Van Heeswijk, J. J. H. Kloos, J. De Heer, T. Hoeks, N. Grossiord, A. P. H. J. Schenning, *ACS Appl Mater Interfaces* **2018**, *10*, 30008.
- [69] J. Shin, J. Sung, M. Kang, X. Xie, B. Lee, K. M. Lee, T. J. White, C. Leal, N. R. Sottos, P. V. Braun, D. G. Cahill, *Proc Natl Acad Sci* **2019**, *116*, 5973.
- [70] G. Wehmeyer, T. Yabuki, C. Monachon, J. Wu, C. Dames, *Appl Phys Rev* **2017**, *4*, 041304.
- [71] J. Cho, M. D. Losego, H. G. Zhang, H. Kim, J. Zuo, I. Petrov, D. G. Cahill, P. V. Braun, *Nat Commun* **2014**, *5*, 2.
- [72] J. Shin, M. Kang, T. Tsai, C. Leal, P. V. Braun, D. G. Cahill, *ACS Macro Lett* **2016**, *5*, 955.
- [73] S. N. Leung, M. O. Khan, H. Naguib, F. Dawson, *Appl Phys Lett* **2014**, *104*, 081904.
- [74] M. Saeidjavash, J. Garg, B. P. Grady, B. Smith, Z. Li, R. J. Young, F. Tarranum, N. Bel Bekri, *Nanoscale* **2017**, *9*, 12867.
- [75] J. S. Kang, M. Li, H. Wu, H. Nguyen, Y. Hu, *Science* **2018**, *361*, 575.
- [76] D. Kang, H. Ko, J. Koo, S. Lim, J. S. Kim, Y. Yu, C. Lee, N. Kim, K. Jeong, *ACS Appl Mater Interfaces* **2018**, *10*, 35557.
- [77] D. G. Kang, N. Kim, M. Park, C. Nah, J. S. Kim, C. R. Lee, Y. Kim, C. Bin Kim, M. Goh, K. U. Jeong, *ACS Appl Mater Interfaces* **2018**, *10*, 3155.
- [78] J. A. King, M. G. Miller, R. L. Barton, J. M. Keith, R. A. Hauser, K. R. Peterson, L. L. Sutter, *J Appl Polym Sci* **2006**, *99*, 1552.
- [79] I. I. El-Sharkawy, A. Pal, T. Miyazaki, B. B. Saha, S. Koyama, *Appl Therm Eng* **2016**, *98*, 1214.
- [80] Z. Wang, R. Qi, J. Wang, S. Qi, *Ceram Int* **2015**, *41*, 13541.
- [81] W. Zhou, J. Zuo, X. Zhang, A. Zhou, *J Compos Mater* **2014**, *48*, 2517.
- [82] L. Chen, H. F. Xu, S. J. He, Y. H. Du, N. J. Yu, X. Z. Du, J. Lin, S. Nazarenko, *PLoS One* **2017**, *12*, 0170523.
- [83] L. Fang, C. Wu, R. Qian, L. Xie, K. Yang, P. Jiang, *RSC Adv* **2014**, *4*, 21010.

Chapter 1

Chapter 2

The Role of Polyethylene Wax on the Thermal Conductivity of Transparent Ultradrawn Polyethylene Films



Abstract Transparency and thermal conductivity of ultradrawn ultrahigh molecular weight polyethylene films containing different contents of low molecular weight polyethylene wax (PE_{wax}) are explored from experimental and theoretical viewpoints. It is shown that the addition of PE_{wax} decreases light scattering in all directions, resulting from a reduction of defects while having little effect on crystallinity or chain orientation of ultradrawn films. In general, upon the addition of PE_{wax} , the thermal conductivity of ultradrawn films increases with the highest conductivity being $47 \text{ (W m}^{-1} \text{ K}^{-1}\text{)}$ and subsequently decreases at higher concentrations. The thermal conductivity also depends on the draw ratio and number-average molecular weight (M_n) of the films. A model is presented which correlates the thermal conductivity of the films with the draw ratio and M_n , enabling an explanation of the experimental results. Hence, the thermal conductivity of ultradrawn polyethylene films can be predicted as a function of M_n and draw ratio.

This chapter is largely reproduced from:

Pan, X., Schenning, A. P. H. J., Shen, L., & Bastiaansen, C. W. M. The Role of Polyethylene Wax on the Thermal Conductivity of Transparent Ultradrawn Polyethylene Films. *Macromolecules*, 2020, 53, 5599.

2.1 Introduction

Thermally conductive materials such as metals, ceramics, carbon materials, and polymer composites are receiving a lot of attention both from scientific and application points of view. Polymer composites are attractive due to their low density, ease of processing and chemical stability (as seen in **Chapter 1**).^[1–4] In these composites, the intrinsically low conductivity of polymers is enhanced by adding thermal conductive additives. However, most polymer composites are non-transparent due to light scattering and/or absorbance by additives, which limits their applications. Most polymers are amorphous or semi-crystalline and their low thermal conductivity is usually attributed to phonon scattering.^[2,5] Generally, phonon transport in isotropic polymers is influenced by many factors including the number of side chains, the chemical composition, and morphology.^[2,3] The thermal conductivity of isotropic polymers is typically below $1 \text{ W m}^{-1} \text{ K}^{-1}$,^[6] while anisotropic polymers with higher thermal conductivity can be obtained via a variety of techniques such as drawing.^[7–10]

The thermal conductivity of ultradrawn PE films in the drawing direction increases non-linearly with increasing draw ratio^[11,12] while the transverse thermal conductivity slightly decreases.^[12] A model has been derived by Ronca et al. to describe the non-linear thermal conductivity versus draw ratio of ultradrawn PE, which assumes that the thermal conductivity is governed only by the draw ratio.^[11] Xu et al. reported that thermal conductivity also depends on the length of the crystal phase.^[9] Furthermore, computer simulations suggest that the thermal conductivity of a single PE chain and bulk PE might also depend on chain length to some extent.^[6,13–15] However, experimental evidence for chain length dependence of the thermal conductivity in drawn polymer films has not been reported to date.

2.2 Results and Discussion

2.2.1 Thermal conductive and transparent ultradrawn films

Transparent ultradrawn UHMWPE ($M_w \sim 4 \times 10^3 \text{ kg/mol}$) with different ratios of PE_{wax} of different M_n (PE_{wax} B, $M_n \sim 1000 \text{ g/mol}$; PE_{wax} C, $M_n \sim 3000 \text{ g/mol}$, and PE_{wax} D, $M_n \sim 4255 \text{ g/mol}$) were fabricated by solution-casting, followed by solid-state stretching. The M_w of the PE films decreases linearly upon adding PE_{wax} (**Figure 2.1a**) while the M_n of the films shows a sharp, non-linear decrease (**Figure 2.1b**). The polydispersity, \mathfrak{D} , displays an inverse, linear trend (**Figure 2.1c**), indicating that adding wax with low M_w and M_n has a little effect on M_w of PE-wax films but a large effect on M_n since short chains mainly contribute to M_n . To further characterize the structure of ultradrawn UHMWPE films before and after adding different PE_{wax}, Raman spectra were recorded (**Figure 2.2**). The intensity ratio of Raman bands at 1128 cm^{-1} to 1060 cm^{-1} is representative of the orientation of ultradrawn films, while the ratio of integral areas of the Raman band at 1414 cm^{-1} to Raman the bands at 1293 cm^{-1} and 1305 cm^{-1} represent the crystallinity of the films.^[16] The Raman results indicate that adding PE_{wax} has no obvious effect on the crystallinity or the orientation of the films while drawing increases the chain orientation and crystallinity.

Thermal conductivity of transparent ultradrawn polyethylene/wax films

M_w , M_n , and PDI were calculated by the following equations

$$M_{wf} = M_{ww}\varphi + M_{wp}(1 - \varphi) \quad (2.1)$$

$$\frac{1}{M_{nf}} = \frac{\varphi}{M_{nw}} + \frac{(1-\varphi)}{M_{np}} \quad (2.2)$$

$$PDI = \frac{M_w}{M_n} \quad (2.3)$$

Here, M_{wf} , M_{ww} , and M_{wp} are the M_w of the films, wax, and polyethylene, respectively. M_{nf} , M_{nw} , and M_{np} are the M_n of the films, wax, and polyethylene, respectively. φ is the wax content in the film.

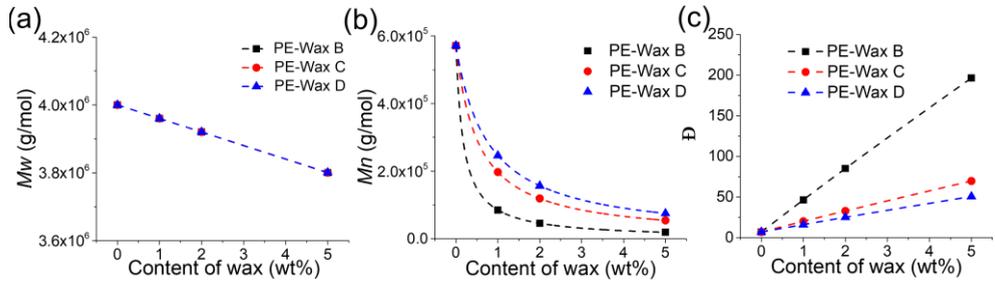


Figure 2.1 (a) M_w , (b) M_n and (c) PDI (b) of pure PE and PE-wax films.

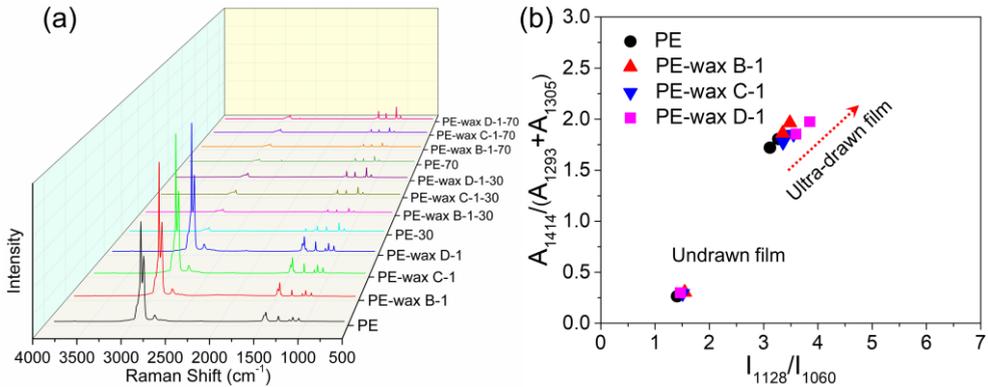


Figure 2.2 (a) Raman spectra of PE and PE-wax films with draw ratios of 1, 30 and 70, (b) Ratio of integral areas of Raman band at 1414 cm^{-1} to Raman bands at 1293 cm^{-1} and 1305 cm^{-1} versus intensity ratio of Raman bands at 1128 cm^{-1} and 1060 cm^{-1} .

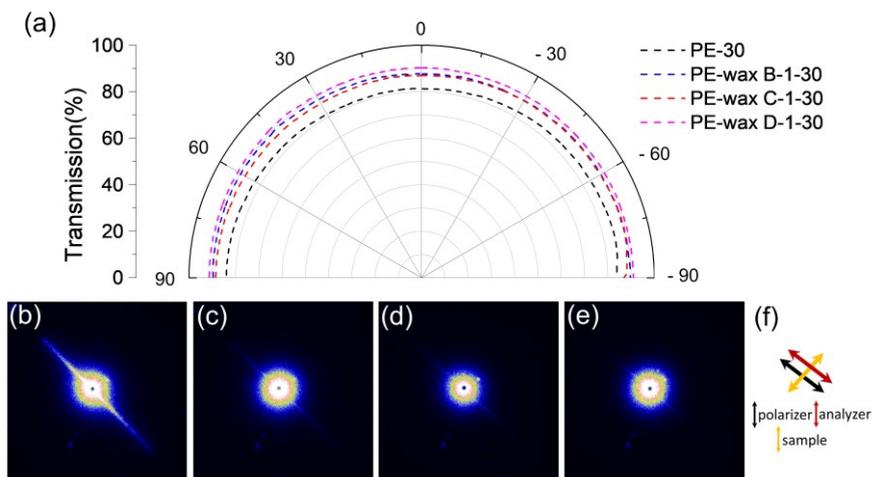


Figure 2.3 (a) Polarized visible light transmission of pure PE and PE-wax films at 550 nm. The angular axes represent the angle between the polarizer and the drawing direction of the films. (b-e) SALS (Vv) patterns of PE, PE-wax B, PE-wax C and PE-wax D films with 1 wt% wax and a draw ratio of 30. (f) Drawing directions of samples and polarizers in SALS images.

First, the polarized visible light transmission was measured of the ultradrawn PE and PE-wax films containing 1 wt% PE_{wax} (**Figure 2.3a**). The transparency of the PE-wax films is higher than the PE films and displays angular independence. The PE-wax films exhibit a higher visible light transmission (over 90%), while pure PE film shows a lower visible light transmission (84%). However, ultradrawn PE-wax films with different waxes or M_n did not show the obvious difference between optical transmission (**Figure 2.3**). Small-angle light scattering (SALS) measurements reveal strong and weak light scattering in the pure PE and PE-wax films, respectively. In the past, the enhanced visible light transmission was attributed to the filling of microvoids with an elongated shape parallel to the drawing direction^[17] and it is assumed that this is also the case here. The improved optical transmission of PE-wax films could be attributed to the decreasing voids inside drawn films and matched refractive indexes between PE and PE_{wax}.

Next, the thermal conductivities of the different ultradrawn UHMWPE and PE_{wax} films were measured (**Figure 2.4a-c**). In the case of PE_{wax} films with a draw ratio of 30 (**Figure 2.4a**), the thermal conductivity of the films increased upon the addition of 1 wt% PE_{wax}. PE-wax D films exhibit a higher thermal conductivity than the PE-wax C and PE-wax B films, suggesting that the molecular weight of the wax has an effect on the thermal conductivity. Upon increasing the PE-wax content, the films showed a nonlinear decrease in the thermal conductivity (**Figure 2.4a**). In general, upon increasing the draw ratio from 30 to 100, the thermal conductivity increases (**Figure 2.4a-c**) and the highest conductivity of 47 (W m⁻¹ K⁻¹) is observed for the PE-wax containing 1 wt % PE_{wax}-D with a draw ratio of 100 (**Figure 2.4c** and **Figure 2.5a**).

Thermal conductivity of transparent ultradrawn polyethylene/wax films

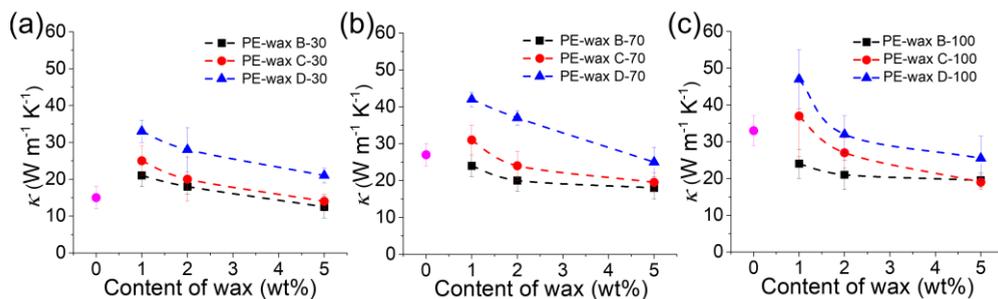


Figure 2.4 Thermal conductivity of PE-wax films as a function of contents of PE_{wax} with fixed draw ratios (a-c). The pink dot represents the data of pure PE films (without wax) with draw ratios of 30, 70 and 100.

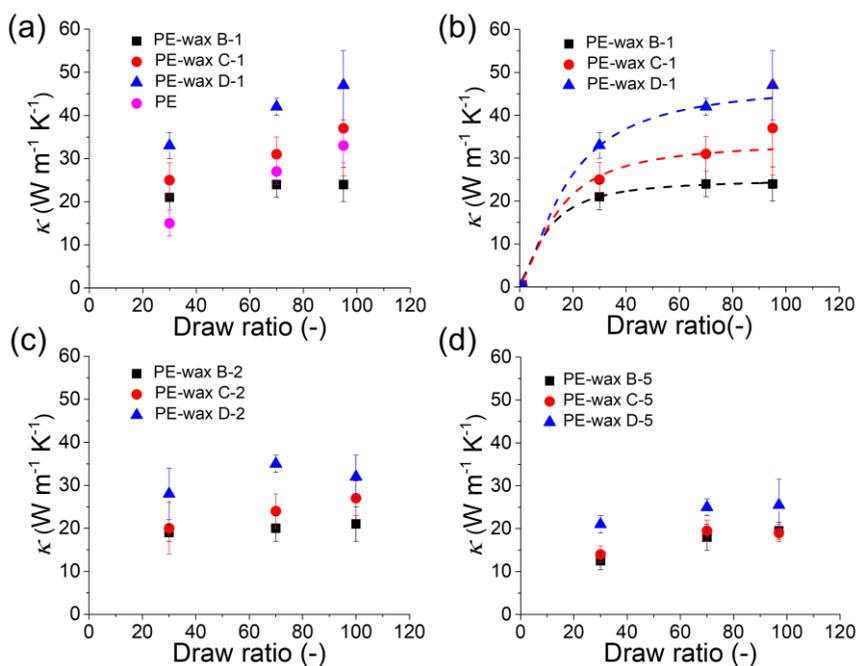


Figure 2.5 (a-d) Thermal conductivity of PE-wax films as a function of draw ratios. a: pure PE and PE with 1 wt% waxes. b-d: PE with 1, 2 and 5 wt% waxes. In **Figure 2.6**, the dashed lines are the fitting curves using equation 1 and the value of thermal conductivity with a draw ratio of 1 is set as $0.5 \text{ W m}^{-1} \text{ K}^{-1}$.^[2,5,7]

When displaying the thermal conductivity as a function of the draw ratio, a non-linear relationship is observed (**Figure 2.5a-d**), consistent with previous publications.^[10,18] However, the thermal conductivity of ultradrawn films with high PE_{wax} content did not increase further (**Figure 2.5c-d**).

The lower thermal conductivity of pure PE ultradrawn films could result from the phonon scattering (**Figure 2.3**) caused by defects such as nano- or microvoids inside the bulk PE films. Upon addition of 1% of PE-wax, these voids are filled, leading to less phonon scattering and enhanced thermal conductivity. However, PE-wax B films having a low molecular weight of PE-wax with a high draw ratio are an exception. The different PE-wax films show different thermal conductivity at the same draw ratio, and the films with the highest molecular weight PE_{wax} (PE-wax D) outperform the other films. As the crystallinity and chain orientation in the PE-wax films is the same (*vide supra*), this reveals that the thermal conductivity also depends on the molecular weight of the wax.

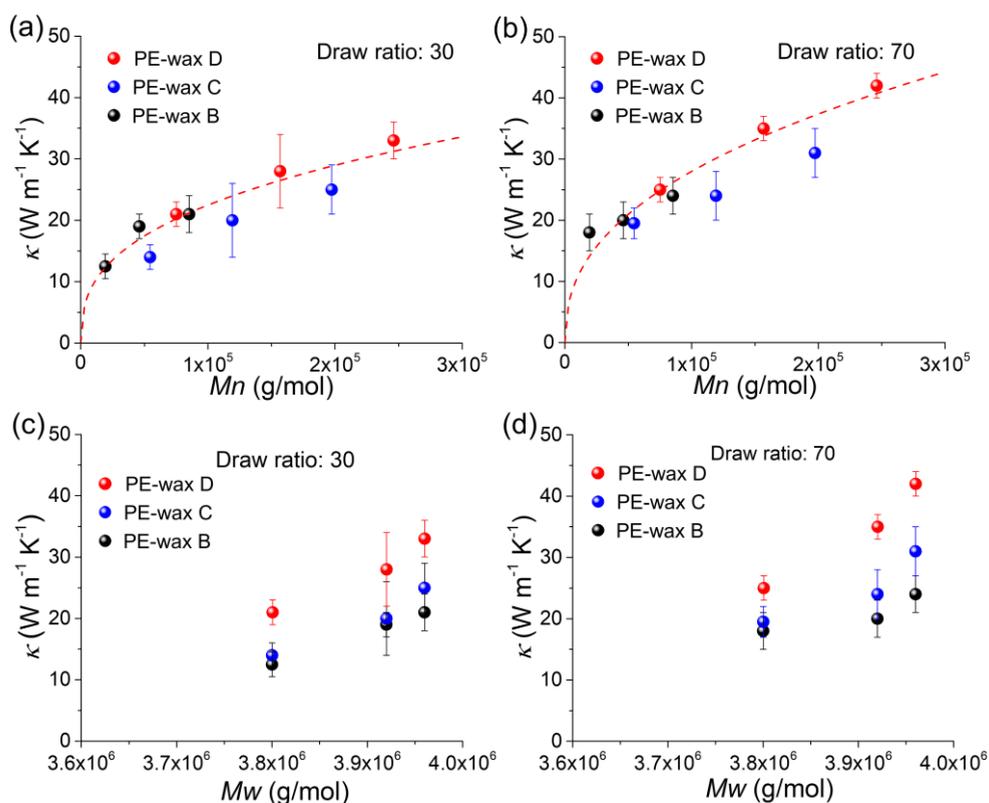


Figure 2.6 Thermal conductivity of PE-wax films with draw ratios of 30 and 70 as a function of M_n (a, b) and M_w (c, d). The red dashed lines are the curves fit using equation 2.4. When the draw ratio is 70 times, κ is close to κ_1 and κ_2 is ignored. The values of parameters in equation 2.4 are obtained based on the thermal conductivity at a draw ratio of 70. The data of pure PE films are excluded due to their different morphology with PE-wax films.

Thermal conductivity of transparent ultradrawn polyethylene/wax films

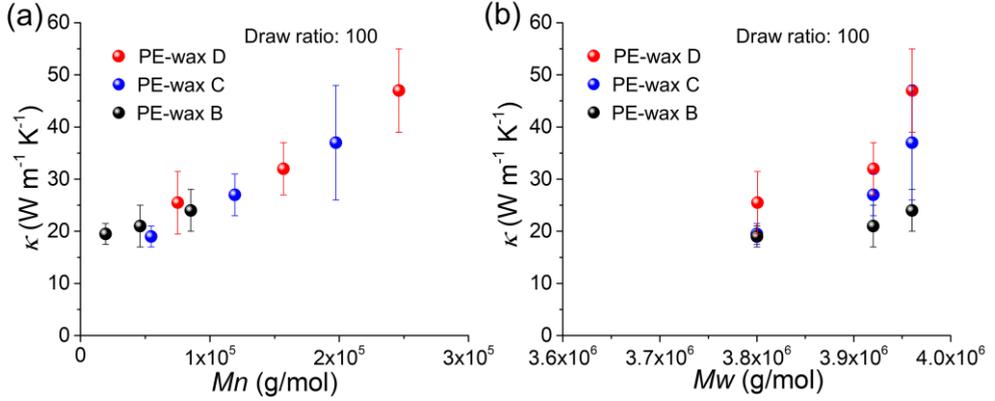


Figure 2.7 Thermal conductivity of PE-wax films with a draw ratio of 100 as a function of M_n and M_w .

To investigate the molecular weight dependence further, the thermal conductivity of PE-wax films with different PE_{wax} concentrations was plotted as a function of the number-average molecular weight, M_n , and the weight-average molecular weight, M_w , at two draw ratios (**Figure 2.6** and **Figure 2.7**). The plots show that the thermal conductivity of ultradrawn films increases with increasing M_n , while there is no such relationship with M_w . PE-wax films with similar M_w and content of PE_{wax} show different thermal conductivities, indicating the thermal conductivity of ultradrawn films is more related to M_n than M_w .

2.2.2 Model for thermal conductivity, M_n and draw ratio

To shed light on the relationship between M_n , draw ratio and thermal conductivity of PE-wax films, a model is developed based on the assumption that the extended-chain region mainly contributes to thermal conductivity in ultradrawn films and that the majority of regions in ultradrawn PE films are extended chain regions.^[10] Thus, only the effect of the extended-chain region is considered in our model.

The thermal conductivity (κ) in anisotropic polymers has been described by Ronca et al (equation 2.4):^[11]

$$\frac{1}{\kappa} = \left(\frac{1}{\kappa_1} - \frac{1}{\kappa_2} \right) \left\{ \frac{\lambda^3}{\lambda^3 - 1} - \frac{\lambda^3}{(\lambda^3 - 1)^{\frac{3}{2}}} \tan^{-1} \left[(\lambda^3 - 1)^{\frac{1}{2}} \right] \right\} + \frac{1}{\kappa_2} \quad (2.4)$$

where λ is the draw ratio, κ_1 and κ_2 the thermal conductivities of perfectly oriented polymers parallel and perpendicular to the chain axis, respectively, and they are considered as constant

Chapter 2

typically. It was found that equation 2.4 can also describe our data at a constant M_n in each PE-wax system assuming that the thermal conductivity on unstretched PE-wax films is low (**Figure 2.5b**). However, this equation is not able to describe the different thermal conductivity values for the different PE-wax films (**Figure 2.6a and b**).

As mentioned earlier, κ_l has been described in computer simulations as an exponential function of chain length (L).^[13,14] However, the thermal transport is different in a single PE chain than PE films^[19] as PE chains are difficult to be extended completely in polymer films without entanglements and kinks.^[13,15] Therefore, in our model, κ_l is described by an exponential function of M_n instead of chain length.

$$\kappa_1 = BM_n^\gamma \quad (2.5)$$

Here, B is a constant and its unit is $W/(g/mol)^\gamma m^{-1} K^{-1}$. γ indicates the competition between diffusive and ballistic phonon transport, where diffusive and ballistic phonon transport leads to $\gamma = 0$ and 1, respectively.^[13]

By combining equations 2.4 and 2.5, equation 2.6 describes both the dependence of the thermal conductivity as a function of M_n and draw ratio:

$$\frac{1}{\kappa} = \left(\frac{1}{BM_n^\gamma} - \frac{1}{\kappa_2} \right) \left\{ \frac{\lambda^3}{\lambda^3 - 1} - \frac{\lambda^3}{(\lambda^3 - 1)^{\frac{3}{2}}} \tan^{-1} \left[(\lambda^3 - 1)^{\frac{1}{2}} \right] \right\} + \frac{1}{\kappa_2} \quad (2.6)$$

In the case of a specific draw ratio, the thermal conductivity is described roughly by M_n following the equation below, which is consistent with that in a perfect stretched PE chain.^[13]

$$\kappa = BM_n^\gamma \quad (2.7)$$

The values of B and γ are approximately 0.206 ± 0.13 and 0.426 ± 0.052 by fitting the data in **Figures 2.6a and b**.

When M_n was fixed, equation 2.4 is obtained from equation 2.5 while equation 2.7 is achieved from equation 2.6 with a fixed draw ratio. Equation 2.6 was verified using the ultimate thermal conductivity predicted by equation 2.4, revealing the good fitting between

equation 2.4 and equation 2.6 in different systems. These fitting results demonstrate the accuracy of our model and its feasibility in other polyethylene systems.

According to our model, the draw ratio is the main factor determining thermal conductivity at low draw ratios, while M_n mainly contributes to the increase in thermal conductivity at high draw ratios. This indicates that polyethylene films with a high M_n could exhibit a high thermal conductivity at high draw ratios. The increased thermal conductivity in ultradrawn films with the high M_n could be attributed to less short chains, resulting in weak photon scattering.¹⁴ However, chain entanglements, side chains and defects inside of films show negative effects on thermal conductivity and these factors were not considered in our work (see also supporting information). The underlying mechanism was speculated. The thermal conductivity of (isotropic and anisotropic) polymers is governed by intramolecular and intermolecular phonon transport. In the case of most polymers, the intramolecular phonon transport along the macromolecular backbone is dominated which results in a high theoretical thermal conductivity for extended-chain molecules and/or extended-chain crystals with an infinite molecular weight.^{6,9,10,14} In real polymeric systems with a high molecular weight, the macroscopic thermal conductivity is usually restricted by intermolecular phonon transport between the chains which is facilitated by orientation and chain extension.^{1,2,15,20} Upon the addition of waxes with low contents, the interfibrillar voids in ultra-drawn polymers are avoided which decreases intermolecular phonon scattering and enhances thermal conductivity. With the increasing M_n of PE wax, the number of chain ends of PE wax decreases, resulting in less phonon scattering, which explains the observed semi-empirical relationship presented in this study to a certain extent. The density/size of phase-separated PE wax at low content could decrease when M_n of PE wax increases.

2.3 Conclusions

Highly transparent PE-wax ultradrawn films were fabricated by solution-casting and solid-stretching method. It was found that adding PE_{wax} improves the visible light transmission (> 90%) of ultradrawn PE films via decreasing defects inside films while adding PE_{wax} has a little effect on the crystallinity and orientation of ultradrawn films. It is revealed that the thermal conductivity of ultradrawn PE-wax films not only depends on the draw ratio but also on the M_n of PE-wax films. Furthermore, the thermal conductivity of PE-wax films predicted by our model is in good agreement with experimental results. The model shows the relationship between thermal conductivity, M_n and draw ratio and it is able to predict the thermal conductivity of drawn polymers by macroscopic parameters, such as M_n and draw ratio, which is vital for making transparent, high thermally conductive polymer films in optoelectronic devices where thermal management is crucial.

2.4 Experimental section

Materials. UHMWPE (weight-average molecular weight (M_w) $\sim 4 \times 10^3$ kg/mol and a polydispersity index (PDI or $\mathfrak{D} \sim 7$) was received from DSM (Geleen, The Netherlands). PE_{wax} B ($M_n \sim 1000$ g/mol, $\mathfrak{D} \sim 1.08$) and PE_{wax} C ($M_n \sim 3000$ g/mol, $\mathfrak{D} \sim 1.08$) were purchased from Baker Hughes Incorporated. PE_{wax} D ($M_n \sim 4255$ g/mol, $\mathfrak{D} \sim 3$) was received from Mitsui Chemicals Incorporated (Japan). Paraffin oil and xylene were purchased from Thermo Fisher Scientific Incorporated (The Netherlands) and Biosolve BV (The Netherlands), respectively. All reagents were used without further purification.

Fabrication. Firstly, UHMWPE powder (2 g), PE_{wax} (0, 1, 2 and 5 wt% to UHMWPE/PE_{wax} blend) and the antioxidant Irganox 1010 (0.1 wt% to UHMWPE) were added to xylene (200 mL). After degassing via ultra-sonication for 30 minutes, the mixture was stirred at approximately 120 °C in an oil bath until the Weissenberg effect was observed. The solution was then cast into aluminum trays of approximately 144 cm² after UHMWPE was completely dissolved. The solution-cast films were left at room temperature for several days to evaporate the xylene completely. Dry UHMWPE/PE_{wax} (PE-wax) films were then cut into small strips and were stretched at ~ 120 °C.

Analytical Techniques. The surface microstructure and roughness of the films were characterized by optical microscopy (Leica DM 2700M) and an Interferometer (FOGALE Nanotech Incorporated, France). The polarized transmittance of samples was measured in the range of 0-180 degrees at 550 nm on a Shimadzu (Japan) UV-3102 PC spectrophotometer with a 1-degree interval. During UV-vis measurement, the samples were sandwiched between two glass slides and coated with a few drops of paraffin oil to reduce the surface scattering of the samples. Small-angle light scattering (SALS) patterns were measured using a He-Ne gas laser (wavelength: 632 nm) and Vv patterns were obtained with the polarizer and analyzer parallel. Differential scanning calorimetry (DSC) experiments were performed on a TA Instruments Q2000 calorimeter at a rate of 10 °C/min between 25 °C to 180 °C. Wide-angle X-ray scattering (WAXS) measurements were performed on a Ganesha lab instrument equipped with a Genix-Cu ultralow divergence source producing an X-ray with a wavelength of 1.54 Å. Raman spectra were performed to characterize the crystallinity and chain orientation on a Raman Microscope (Witec Alpha 300 R). Thermal conductivity was measured by a setup based on the Angstrom method (**Figure 2.8**).^[20] The thermal conductivity (κ) was calculated using the equation 2.8:

$$\kappa = C_H \times \rho \times \alpha \quad (2.8)$$

Here, C_H is the heat capacity (~ 1.8 J/kg K) of samples, ρ is the density (~ 1000 kg/m³) of samples and α is the thermal diffusivity (m²/s).

Thermal conductivity of transparent ultradrawn polyethylene/wax films

The thermal diffusivity (α) was calculated using Equation 2.9:

$$\alpha = \frac{(\Delta x)^2}{2\Delta t \ln \frac{A_1}{A_2}} \quad (2.9)$$

Here, Δx is the distance between thermocouples (m), Δt (s) is the phase difference between the temperature of the thermocouples, A_1 and A_2 are the temperature amplitudes at the testing points 1 and 2 on the film.

The heater temperature (T) was set following a sine function (equation 2.10):

$$T = 10 \sin(\pi t f) + 55 \quad (2.10)$$

Here, t is time (s), f is the frequency (s^{-1}) and its value is 0.02.

The schematic diagram and calibration of the setup are shown in **Figure 2.8**.

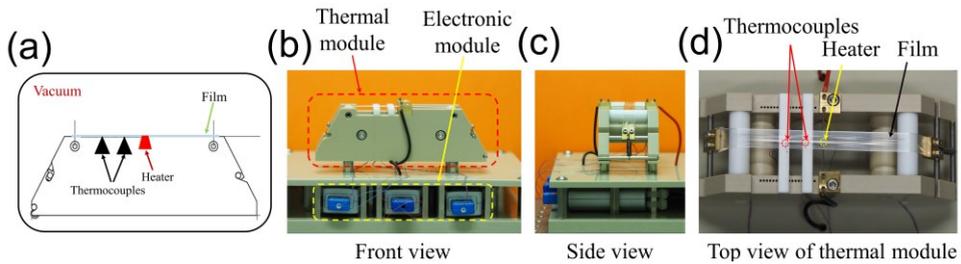


Figure 2.8 (a) The schematic diagram of setup; the images of the measurement module of the system: front (b), side (c) and top (d) view of the experimental setup.

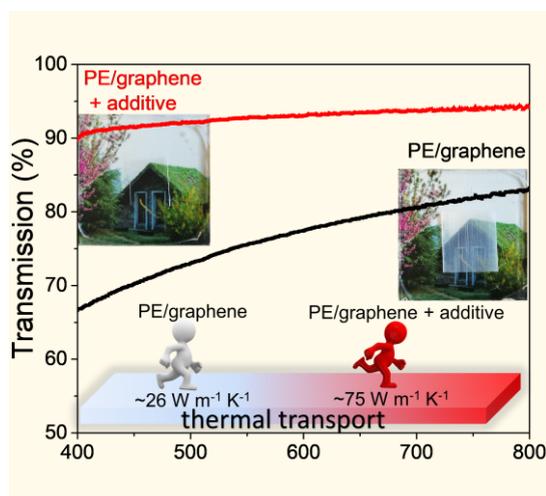
Chapter 2

2.5 References

- [1] X. Xu, J. Chen, J. Zhou, B. Li, *Adv Mater* **2018**, *30*, 1705544.
- [2] H. Chen, V. V. Ginzburg, J. Yang, Y. Yang, W. Liu, Y. Huang, L. Du, B. Chen, *Prog Polym Sci* **2016**, *59*, 41.
- [3] C. Huang, X. Qian, R. Yang, *Mater Sci Eng R Reports* **2018**, *132*, 1.
- [4] Y. Zhang, Y. J. Heo, Y. R. Son, I. In, K. H. An, B. J. Kim, S. J. Park, *Carbon* **2019**, *142*, 445.
- [5] Z. Han, A. Fina, *Prog Polym Sci* **2011**, *36*, 914.
- [6] A. Henry, G. Chen, *Phys Rev Lett* **2008**, *101*, 23502.
- [7] M. Saeidijavash, J. Garg, B. P. Grady, B. Smith, Z. Li, R. J. Young, F. Tarranum, N. Bel Bekri, *Nanoscale* **2017**, *9*, 12867.
- [8] B. Zhu, J. Liu, T. Wang, M. Han, S. Valloppilly, S. Xu, X. Wang, *ACS Omega* **2017**, *2*, 3931.
- [9] Y. Xu, D. Kraemer, B. Song, Z. Jiang, J. Zhou, J. Loomis, J. Wang, M. Li, H. Ghasemi, X. Huang, X. Li, G. Chen, *Nat Commun* **2019**, *10*, 1771.
- [10] S. Shen, A. Henry, J. Tong, R. Zheng, G. Chen, *Nat Nanotechnol* **2010**, *5*, 251.
- [11] S. Ronca, T. Igarashi, G. Forte, S. Rastogi, *Polym* **2017**, *123*, 203.
- [12] C. L. Choy, Y. W. Wong, G. W. Yang, T. Kanamoto, *J Polym Sci Part B Polym Phys* **1999**, *37*, 3359.
- [13] X. Duan, Z. Li, J. Liu, G. Chen, X. Li, *J Appl Phys* **2019**, *125*, 164303.
- [14] J. Liu, R. Yang, *Phys Rev B* **2012**, *86*, 104307.
- [15] Y. Ouyang, Z. Zhang, Q. Xi, P. Jiang, W. Ren, N. Li, J. Zhou, J. Chen, *RSC Adv* **2019**, *9*, 33549.
- [16] R. Shrestha, P. Li, B. Chatterjee, T. Zheng, X. Wu, Z. Liu, T. Luo, S. Choi, K. Hippalgaonkar, M. P. De Boer, S. Shen, *Nat Commun* **2018**, *9*, 1664.
- [17] L. Shen, K. Nickmans, J. Severn, C. W. M. Bastiaansen, *ACS Appl Mater Interfaces* **2016**, *8*, 17549.
- [18] Y. Xu, X. Wang, J. Zhou, B. Song, Z. Jiang, E. M. Y. Lee, S. Huberman, K. K. Gleason, G. Chen, *Sci Adv* **2018**, *4*, 3031.
- [19] A. Henry, G. Chen, S. J. Plimpton, A. Thompson, *Phys Rev B* **2010**, *82*, 144308.
- [20] A. J. Angstrom, *Ann. Phys. Chem.* **1861**, *114*, 33.

Chapter 3

Transparent, High Thermal Conductivity Ultra-drawn Polyethylene/Graphene Nanocomposite Films



Abstract Transparent, ultra-drawn, ultra-high molecular weight polyethylene (UHMWPE)/graphene nanocomposite films with a high thermal conductivity were successfully fabricated by solution-casting and solid-state drawing. It was found that the low optical transmittance ($< 75\%$) of ultra-drawn UHMWPE/graphene composite films was drastically improved ($> 90\%$) by adding 2-(2H-benzotriazol-2-yl)-4, 6-ditertpentylphenol (BZT) as a second additive. This high transmission was interpreted in terms of a reduced void content in the composite films and the improved dispersion of graphene both of which decrease light scattering. The high thermal conductivity is attributed to the π - π interaction between BZT and graphene. In addition, a high specific thermal conductivity of $\sim 75 \text{ W m}^{-1} \text{ K}^{-1}$ of ultra-drawn UHMWPE/graphene/BZT composite films was obtained which is higher than most metals and polymer nanocomposite. These transparent films are potentially excellent candidates for thermal management in various applications due to a combination of low density, ease of processing and high thermal conductivity.

This chapter is largely reproduced from:

Pan, X., Shen, L., Schenning, A. P. H. J., & Bastiaansen, C. W. M. Transparent, High-Thermal-Conductivity Ultradrawn Polyethylene/Graphene Nanocomposite Films. *Advanced Materials*, 2019, 31, 1904348.

3.1 Introduction

Thermal management is vital to the lifetime and performance of a wide variety of electronic devices including solar cells, light-emitting diodes (LEDs) and chips (as seen in **Chapter 1**).^[1-3] With the widespread application of electronics, effective thermal management with thermally conductive materials has become a major technological challenge. Therefore, new and high thermally conductive materials with a high visible light transmission are needed, especially for the thermal management of windows (as seen in **Chapter 2**).^[3,4]

In general, thermally conductive materials include metals, ceramics, carbon materials and polymer composites.^[1,5-12] Compared with other thermally conductive materials, polymer composites have been explored extensively in the past decades due to their low density, ease of processing, high electrical resistivity and corrosion resistance.^[2] Normally, the thermal conductivity of polymers is enhanced with highly thermal conductive additives but the increase in thermal conductivity is limited to less than one order of magnitude ($< 10 \text{ W m}^{-1} \text{ K}^{-1}$), resulting from the high thermal interface resistance between the additive and the polymer matrix.^[2,5,7] Also, polymer composites with a high concentration of fillers are non-transparent due to the visible light scattering and/or absorbance of fillers.

Ultra-drawn, highly oriented and chain-extended polymers were studied extensively due to their high thermal conductivity and mechanical properties even without additives.^[13-17] Solution-spun, ultra-drawn UHMWPE fibers have a thermal conductivity between 10 and 20 $\text{W m}^{-1} \text{ K}^{-1}$ which is at least one order of magnitude higher than that of isotropic polymers.^[17] The maximum thermal conductivity of ultra-drawn nascent UHMWPE films with a draw ratio of more than 200 is $\sim 50 \text{ W m}^{-1} \text{ K}^{-1}$ ^[16] and ultra-drawn nanofibers with a thermal conductivity of $\sim 104 \text{ W m}^{-1} \text{ K}^{-1}$ were also reported with a draw ratio of ~ 410 .^[13] Unfortunately, the latter results were obtained with rather unpractical processing and/or ultra-drawing procedures which limits the usefulness of these fibers and films. In addition, it is tempting to expect that composites consisting of highly oriented systems with inorganic fillers might have an even higher thermal conductivity.^[2] However, inorganic fillers like graphene in ultra-drawn polymers usually cause defects and cracks at the interface between the filler and the highly anisotropic matrix.^[18] These defects or cracks cause light scattering and premature fracture upon ultra-drawing.^[19-21] In other words, it remains a challenge to fabricate transparent ultra-drawn polymer composite films with a high thermal conductivity without defects.

3.2 Results and Discussions

UHMWPE films with draw ratios of 30 and 70 were fabricated by simple solution-casting and solid-state drawing and the transparency of the films was studied using UV-vis spectroscopy. Both light scattering and absorption of light are influenced by film thickness

and in order to eliminate this effect the absorption was divided by the film thickness. Pure UHMWPE films (PE-30 and PE-70, respectively) exhibit a slight deviation from a flat curve (**Figure 3.1a** and **b**) which is usually attributed to light scattering in the drawn films originating from micro-voids parallel to the drawing direction.^[22] The addition of graphene (GN) to the ultra-drawn UHMWPE films (PE-GN-30 and PE-GN-70, respectively) increases the scattering of light enormously. Previously, we found that the addition of 2 wt% of 2-(2H-benzotriazol -2-yl)-4, 6-ditertpentylphenol (BZT) (without graphene) reduces this light scattering and transparent glass-like films are obtained in the visible wavelength range.^[22] Therefore BZT was added to the UHMWPE/GN films. BZT shows a high absorbance of UV light and graphene also absorbs some light in the visible part of the spectrum (**Figure 3.1c**). The addition of both BZT (2 wt%) and graphene (0.1 wt%) to the ultra-drawn UHMWPE films resulted in films with very little visible light scattering which appeared transparent upon visual inspection (Figure 1d and e). From these data, there is a low visible light transmission in ultra-drawn PE-GN film due to light scattering while PE-BZT-GN films show a high visible light transmission and very little light scattering.

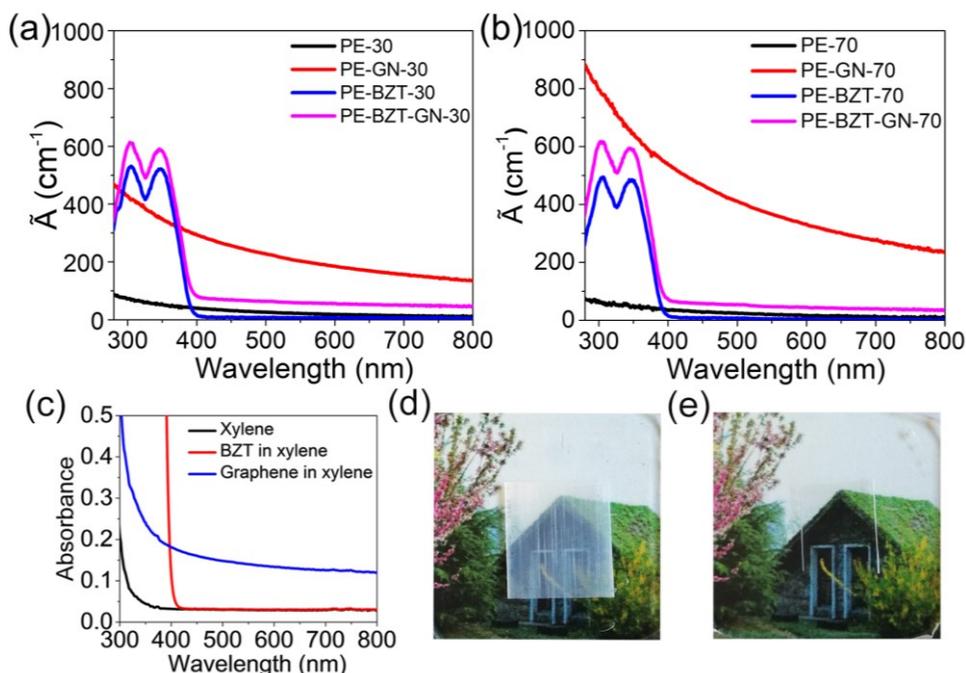


Figure 3.1 UV-vis spectra of solution-cast, ultra-drawn PE, PE-BZT, PE-GN and PE-BZT-GN with draw ratios of (a) 30 and (b) 70. The absorption divided by the film thickness (\tilde{A}) is used to eliminate the effect of film thickness. (c) UV-vis spectra of pure xylene, BZT-xylene solution and graphene-xylene dispersion. The concentration of graphene and BZT in xylene is 0.01 and 0.2 mg/mL, respectively. Optical images of (d) PE-GN and (e) PE-BZT-GN ultra-drawn films with a draw ratio of 30.

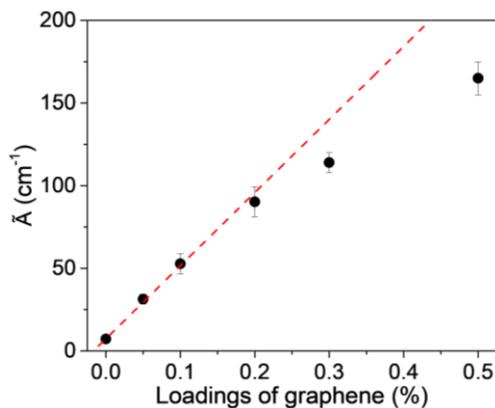


Figure 3.2 \bar{A} of ultra-drawn PE-BZT-GN films at 550 nm as a function of the graphene content and the fitted dashed line of \bar{A} using Lambert-Beer law. There is about 6% error in the data points due to variations in film thickness. The mass ratio of BZT to PE is 0.02 and the background in the UV-vis measurements is PE-BZT films. The draw ratio of the films is 30.

To further explore the role of BZT in the polymer nanocomposite film, ultra-drawn films with different contents of graphene and a constant content of 2 wt% BZT were studied (Figure 3.2). It was found that the transmittance at 550 nm did not follow Lambert-Beer's law at a graphene content above 0.2 wt% due to the aggregation of graphene particles (Figure 3.2). The extinction coefficient of graphene in PE-BZT-GN films was calculated from the slope below a graphene content of 0.2 wt% and was found to be approximately 45.1 L/(g cm) (Figure 3.2), which indicates that the reduced transmittance of PE-BZT-GN film is mainly attributed to the absorbance of GN. Ultra-drawn transparent films with 0.1 wt% graphene and 2 wt% BZT were studied in more detail as these films also showed a high thermal conductivity

The films were further studied by optical microscopy, SALS and WAXS. PE-GN-30 films without BZT showed a lot of defects and aggregation (Figure 3.3a) and the defects increase in size with an increase in draw ratio (Figure 3.3a and 3.3c). The PE-BZT-GN films exhibit an improved dispersion of graphene with the addition of BZT (Figure 3.3b and 3.3d), which indicates that BZT is beneficial to the dispersion of the graphene nanoplatelets. SALS (Vv) patterns were measured to further characterize the light scattering in these ultra-drawn films (Figure 3.3e-h). In accordance with previous studies, SALS (Vv) patterns were used because they are highly sensitive to the density fluctuations and light scattering.^[22] It was found that pure ultra-drawn UHMWPE films exhibit light scattering perpendicular to the drawing direction of the films which is usually attributed to micro-voids parallel to the drawing direction.^[22] The addition of graphene to the ultra-drawn UHMWPE films increases light scattering (Figure 3.3e) and the light scattering increases with the increasing draw ratio (Figure 3.3g), which is in agreement with the results in Figure 1. On the other hand, the ultra-drawn films with BZT/graphene mixtures (Figure 3.3f) hardly exhibit light scattering which is also in accordance with the absorption spectra in Figure 3.1. With an increasing

Transparent, high thermal conductivity ultra-drawn polyethylene/graphene films

draw ratio, the same phenomena are observed e.g. the light scattering is strongly reduced in ultra-drawn UHMWPE films containing BZT/graphene mixtures (**Figure 3.3h**). These results indicate that the increased light scattering in ultra-drawn UHMWPE films upon addition of graphene can be circumvented by adding BZT. Apparently, BZT decreases the voids in ultra-drawn UHMWPE composite films containing graphene and also improves the dispersion of graphene, both of which reduce light scattering enormously. WAXS measurements of undrawn films and ultra-drawn films are shown (**Figure 3.3i-l**). The unit cell parameters and the Herman's orientation function of ultra-drawn films were calculated and it was found that the addition of the graphene/BZT mixtures has no obvious effect on both the unit cell parameters and orientation of ultra-drawn films. Therefore, it is concluded that the addition of graphene and BZT has no significant effect on the degree of chain orientation and extension, that BZT and graphene are not incorporated in the crystal lattice and that the melting temperature and crystallinity of ultra-drawn composite films are not influenced to a large extent.

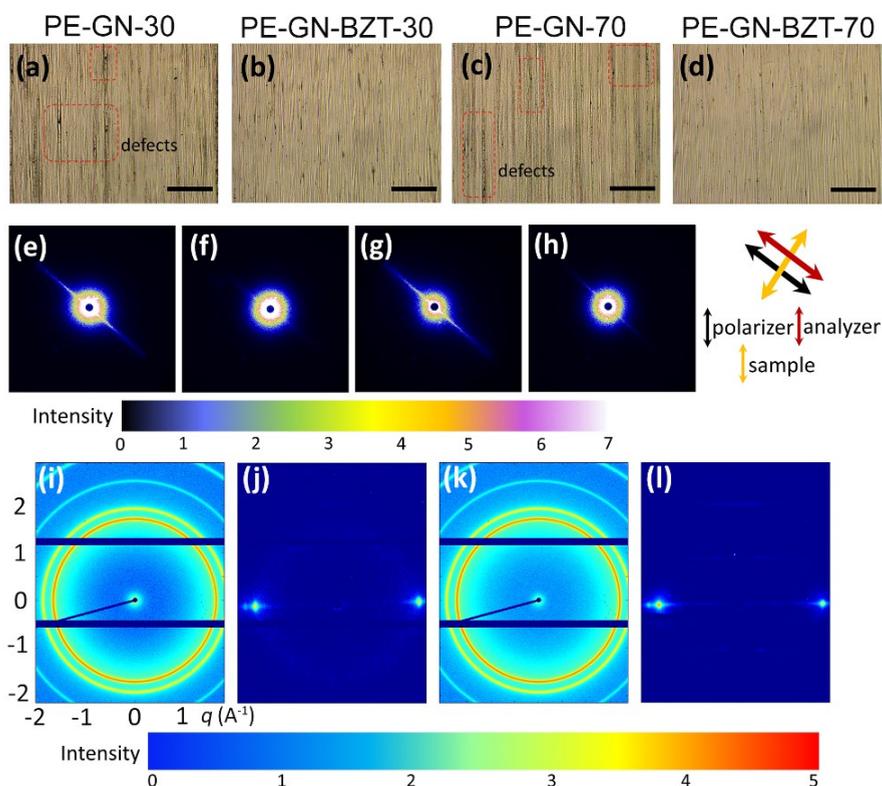


Figure 3.3 Optical images of (a) PE-GN-30, (b) PE-BZT-GN-30, (c) PE-GN-70 and (d) PE-BZT-GN-70 films (Scale bar: 100 μm); SALS (Vv) images of (e) PE-GN-30, (f) PE-BZT-GN-30, (g) PE-GN-70 and (h) PE-BZT-GN-70 films; 2D wide-angle X-ray scattering (WAXS) images of (i) PE-GN-1, (j) PE-GN-70, (k) PE-BZT-GN-1 and (l) PE-BZT-GN-70 films.

To explore the interaction between BZT and graphene, UV-vis spectra were recorded as a function of the graphene content (**Figure 3.4a**). A red shift of about 3 nm is observed in the UV-vis spectra of BZT/graphene mixtures in comparison to the films containing graphene only. Furthermore, hyperchromicity is observed and the absorption peaks at 305 and 350 nm increased with increasing contents of graphene, which suggests the presence of most likely π - π interaction between BZT and graphene.^[23] This is further supported by Raman spectroscopy. Raman spectra of the films show peak shifts of BZT at 1380, 1448 and 1600 cm^{-1} (**Figure 3.4b**), which correspond to the stretching mode of combination of C-C and C-N, combination of the stretching mode of N=N and in-plane bending mode of CH_2 and the stretching mode of C=C in the benzene ring, respectively.^[24,25]

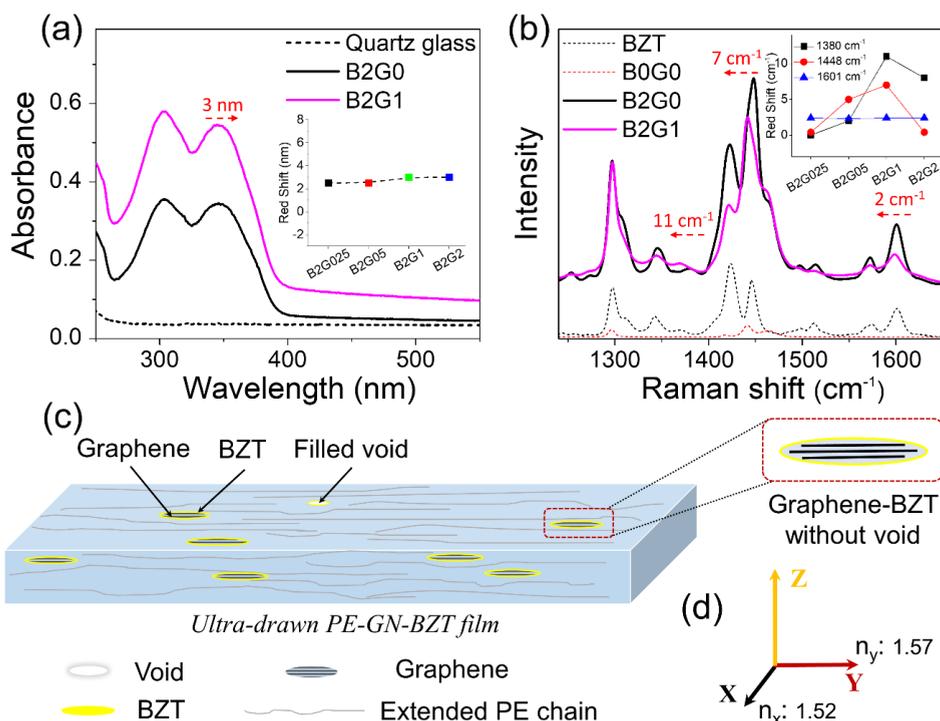


Figure 3.4 (a) Absorbance spectra of ultra-drawn composite films with a draw ratio of 30. (b) Raman spectra of BZT, undrawn B0G0 (pure PE), B2G0 and B2G1 film. BXGY represents the ultra-drawn composite films with X wt% BZT and Y/10 wt% graphene. (c) Schematic representation of the structure of ultra-drawn PE film containing BZT and graphene (d) Refractive index of drawn PE films in different directions.

Normally, there are defects and voids in ultra-drawn polyethylene film, which can cause light and phonon scattering. Adding inorganic fillers like graphene causes a large number of additional defects at the interface between graphene and polyethylene in ultra-drawn films, which mainly results in a large increase in light and phonon scattering and a decrease in visible light transmission. In PE-BZT-GN ultra-drawn films, BZT apparently restricts the light scattering to some extent by filling the voids and it improves the dispersion of graphene

Transparent, high thermal conductivity ultra-drawn polyethylene/graphene films in polyethylene (**Figure 3.4c**) both of which improve the visible transmission of ultra-drawn PE-BZT-GN film.^[21,22] BZT can fill in voids to reduce light scattering mainly due to the similar refractive index of BZT ($n_{\text{BZT}} = 1.575$ and its structure as shown in **Figure 3.4d**) and PE ($n_y = 1.57$ parallel to the drawing direction and $n_x = 1.52$ perpendicular to the drawing direction as shown in **Figure 3.4d**).^[26]

The thermal conductivity of the ultra-drawn films with different draw ratios was measured using the Angstrom method (see **Chapter 2, Figure 2.8**).^[27] The experimental data using this method are compared with data from the literature which indicates that the setup is accurate about 5%. The thermal conductivity of the pure solution-casting ultra-drawn polyethylene films increases with an increasing draw ratio due to an increase in the degree of chain orientation and chain extension.^[13] The addition of graphene and BZT increases the thermal conductivity of ultra-drawn films with more than a factor 2, while the addition of BZT alone or graphene alone improves thermal conductivity a little bit or even has a negative effect (**Figure 3.5a**) because the voids or defects in the films increase phonon scattering which decreases the thermal conductivity.^[2] Rather surprisingly, the thermal conductivity of ultra-drawn films with both BZT and graphene increases quite a lot compared to the reference samples and a maximum thermal conductivity of $75 \text{ W m}^{-1} \text{ K}^{-1}$ is found at a draw ratio of 100.

It is assumed that the thermal conductivity in macromolecular systems is dominated by phonon transport along the macromolecular chain and phonon scattering.^[2,5,28] The high thermal conductivity of oriented and chain extended systems (without additives) in the alignment direction is usually attributed to a reduced phonon scattering.^[13,14] In composite films without BZT, only weak vdW interactions can occur which is usually assumed to be not beneficial for phonon transport.^[7] On the contrary, the π - π interaction in composite films containing both BZT and graphene could substantially enhance phonon transport.^[8] Therefore, the high thermal conductivity of B2G1 ultra-drawn film is attributed to the reduction of defects and voids and the π - π interaction between BZT and graphene.

As mentioned earlier, commercial solution-spun and ultra-drawn UHMWPE fibers have a typical thermal conductivity of $\sim 15 \text{ W m}^{-1} \text{ K}^{-1}$ ^[17] and ultra-drawn UHMWPE films based on so-called nascent or virgin UHMWPE exhibit a thermal conductivity of $\sim 50 \text{ W m}^{-1} \text{ K}^{-1}$.^[16] The maximum value for the thermal conductivity of B2G1 ultra-drawn film is about 3-fold higher than that of stainless steel ($\sim 18 \text{ W m}^{-1} \text{ K}^{-1}$) but lower in comparison to metallic thermally conductive materials, such as copper ($\sim 410 \text{ W m}^{-1} \text{ K}^{-1}$), aluminum ($\sim 237 \text{ W m}^{-1} \text{ K}^{-1}$) and silver ($\sim 403 \text{ W m}^{-1} \text{ K}^{-1}$). However, these metals are reflective and/or non-transparent which can be a limitation in specific applications. More importantly, in many applications the specific thermal conductivity (e.g. per unit weight) is relevant especially if weight is an issue, for instance, to reduce fuel consumption in transport applications.^[29,30] Therefore, the data are re-plotted in **Figure 3.5b** and it is shown that solution-casting ultra-drawn UHMWPE films outperform steel and copper and that maximum values close to aluminum can be obtained which, of course, is also non-transparent.^[2,5]

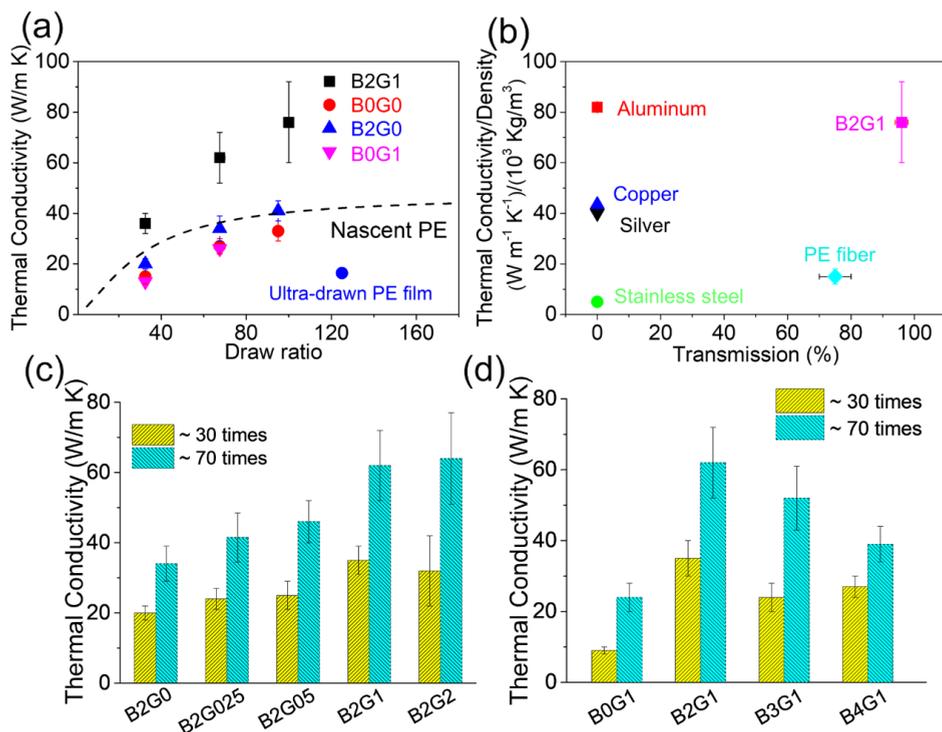


Figure 3.5 (a) Comparison of thermal conductivity for different polyethylene samples as a function of draw ratio. The measurement was repeated at least four times and the average data were calculated. (b) The specific thermal conductivity of different materials. Here, nascent PE,^[16] PE fibers^[17] and ultra-drawn PE films^[31] (without additives) are used as reference materials. The transmission of PE fibers and nascent PE was estimated based on the data of pure PE film. The thermal conductivity of ultra-drawn films with different contents of graphene (c) and BZT (d).

The effect of the content of the two additives was studied in detail (**Figure 3.5c** and **d**). The thermal conductivities of ultra-drawn films increase with the increasing content of graphene. The increasing thermal conductivity could be attributed to the highly thermal conductive of graphene. However, graphene could not be dispersed well in the polymer matrix when its content is higher than 0.1 wt% (**Figure 3.2**). In addition, it is shown that the thermal conductivity first increases with an increasing BZT content and then declines again (**Figure 3.5d**). It is proposed that the initial increase originates from the decreasing voids and the π - π interaction and the decrease is caused by the addition of an excess of BZT with the low thermal conductivity.

3.3 Conclusions

In this work, highly transparent, ultra-drawn UHMWPE/graphene nanocomposite films without light scattering were fabricated by adding small amounts of BZT via solution-casting and solid-state drawing. These transparent films possessed a high specific thermal

Transparent, high thermal conductivity ultra-drawn polyethylene/graphene films conductivity, which is higher than that of most metals. The high transmission was interpreted in terms of a reduced void content inside the composite films and the improved dispersion of graphene. WAXS and DSC results showed that adding BZT and graphene had no obvious effect on the crystal structure, orientation, crystallinity and melting temperature of ultra-drawn composite films. These transparent films are potentially excellent candidates for thermal management due to a combination of low density, ease of processing and high thermal conductivity.

3.4 Experimental Section

Materials. Ultra-high molecular weight polyethylene (UHMWPE) with a molecular weight (Mw) $\sim 4 \times 10^3$ kg/mol and dispersity index (\bar{D}) ~ 7 was received from DSM (Geleen, The Netherlands) and graphene nanoplatelets (particle size < 2 μm , specific surface area ~ 750 m^2/g) were purchased from Sigma-Aldrich. 2-(2H-benzotriazol-2-yl)-4, 6-ditertpentylphenol (BZT) was purchased from BASF (Germany). Paraffin oil was purchased from Thermo Fisher Scientific Incorporated (The Netherlands). Xylene was purchased from Biosolve BV (The Netherlands). All reagents were used directly as received without further purification.

Fabrication Ultra-drawn UHMWPE films were prepared by solution-casting and solid-state drawing. Pure UHMWPE, UHMWPE with BZT, UHMWPE with graphene, UHMWPE with both BZT and graphene were prepared and were defined as PE-X, PE-BZT-X, PE-GN-X and PE-BZT-GN-X, respectively. Here, X represents the draw ratio of the films. Firstly, graphene (0.05, 0.1, 0.2, 0.3 and 0.5 wt% to UHMWPE) and BZT (2 wt% to UHMWPE) were dispersed in 200 mL xylene under ultra-sonication for 30 minutes. UHMWPE powder and antioxidant Irganox 1010 (0.1 wt% to UHMWPE) were then added to the dispersion before degassing with a second ultra-sonication at room temperature for 30 minutes. Subsequently, the mixture was stirred continuously in an oil bath at about 125 °C until the Weissenberg effect was observed. Then the mixture was heated for 2 h to completely dissolve the UHMWPE in the xylene. The solutions were cast in aluminum trays and quenched to room temperature. A dry film was obtained after xylene evaporation at room temperature. UHMWPE films without graphene and/or BZT were produced using the same procedure. To prepare ultra-drawn films, the as-prepared cast films were first cut into small strips with dimensions of 12 mm \times 15 mm which were ultra-drawn at 120 °C. The draw ratio was determined by measuring the displacement of ink marks.

Analytical Techniques. The transmittance spectra of films were measured in the range of 300-800 nm on a Shimadzu (Japan) UV-3102 PC spectrophotometer at a 1-nm interval. The UV-vis was equipped with an MPC-3100 multi-purpose large sample compartment. The samples were sandwiched between two glass slides and were coated with a few drops of paraffin oil to avoid surface light scattering.^[22] A sample to detector distance of about 85 cm was employed. In a few cases, the paraffin oil was replaced by a thermoplastic polyurethane (TPU) and a laminate was made by compression molding at 100 °C.

Chapter 3

Optical microscopy images of samples were performed on a Leica DM 2700M microscopy without polarizers. Small-angle light scattering (SALS) patterns were measured using a He-Ne gas laser (wavelength: 632 nm) and Vv patterns were obtained with the polarizer and analyzer parallel. The drawing direction of the ultra-drawn film was always perpendicular to both the polarizer and the analyzer.

Wide-angle X-ray scattering (WAXS) measurements were performed on a Ganesha lab instrument equipped with a Genix-Cu ultralow divergence source producing X-ray with a wavelength of 1.54 Å and a flux of 1×10^8 photons/second. Diffraction patterns were collected on a Pilatus 300 K silicon pixel detector which consists of three plates with a 17 pixels spacing in between, resulting in two dark bands on the image. The intensity versus the scattering vector (q) was obtained by azimuthal integration of the obtained diffraction patterns. The unit cell parameters of the orthorhombic crystal lattice and Herman's orientation function of the polyethylene crystals was calculated.^[33]

Thermal conductivities of ultra-drawn composite films were characterized based on the Angstrom method (see **Chapter 2**).

3.5 References

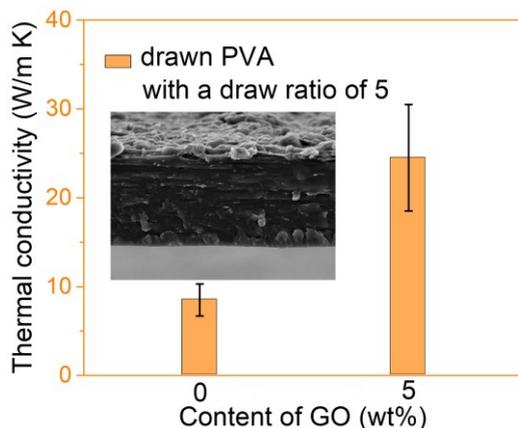
- [1] Z. Han, A. Fina, *Prog Polym Sci* **2011**, *36*, 914.
- [2] H. Chen, V. V. Ginzburg, J. Yang, Y. Yang, W. Liu, Y. Huang, L. Du, B. Chen, *Prog Polym Sci* **2016**, *59*, 41.
- [3] A. Vadiee, V. Martin, *Appl Energy* **2013**, *109*, 337.
- [4] G. K. Dalapati, A. K. Kushwaha, M. Sharma, V. Suresh, S. Shannigrahi, S. Zhuk, S. Masudy-Panah, *Prog Mater Sci* **2018**, *95*, 42.
- [5] C. Huang, X. Qian, R. Yang, *Mater Sci Eng R Reports* **2018**, *132*, 1.
- [6] T. Kuilla, S. Bhadra, D. Yao, N. H. Kim, S. Bose, J. H. Lee, *Prog Polym Sci* **2010**, *35*, 1350.
- [7] X. Xu, J. Chen, J. Zhou, B. Li, *Adv Mater* **2018**, *30*, 1705544.
- [8] Y. Xu, X. Wang, J. Zhou, B. Song, Z. Jiang, E. M. Y. Lee, S. Huberman, K. K. Gleason, G. Chen, *Sci Adv* **2018**, *4*, 3031.
- [9] A. A. Balandin, *Nat Mater* **2011**, *10*, 569.
- [10] M. H. Al-Saleh, U. Sundararaj, *Carbon* **2009**, *47*, 2.
- [11] B. Lv, Y. Lv, X. Liu, Q. Zheng, P. Y. Huang, D. G. Cahill, S. Li, X. Wang, *Science* **2018**, *361*, 579.
- [12] S. Suñer, R. Joffe, J. L. Tipper, N. Emami, *Compos Part B Eng* **2015**, *78*, 185.
- [13] S. Shen, A. Henry, J. Tong, R. Zheng, G. Chen, *Nat Nanotechnol* **2010**, *5*, 251.
- [14] R. Shrestha, P. Li, B. Chatterjee, T. Zheng, X. Wu, Z. Liu, T. Luo, S. Choi, K. Hippalgaonkar, M. P. De Boer, S. Shen, *Nat Commun* **2018**, *9*, 1664.
- [15] C. L. Choy, Y. W. Wong, G. W. Yang, T. Kanamoto, *J Polym Sci Part B Polym Phys* **1999**, *37*, 3359.
- [16] S. Ronca, T. Igarashi, G. Forte, S. Rastogi, *Polym* **2017**, *123*, 203.
- [17] X. Wang, V. Ho, R. A. Segalman, D. G. Cahill, *Macromolecules* **2013**, *46*, 4937.
- [18] J. R. Gissinger, C. Pramanik, B. Newcomb, S. Kumar, H. Heinz, *ACS Appl Mater Interfaces* **2018**, *10*, 1017.
- [19] S. J. V. Frankland, V. M. Harik, G. M. Odegard, D. W. Brenner, T. S. Gates, *Compos Sci Technol* **2003**, *63*, 1655.
- [20] S. Herasati, L. C. Zhang, H. H. Ruan, *Int J Solids Struct* **2014**, *51*, 1781.
- [21] Y. Lu, Y. Wang, R. Chen, J. Zhao, Z. Jiang, Y. Men, *Macromolecules* **2015**, *48*, 5799.
- [22] L. Shen, K. Nickmans, J. Severn, C. W. M. Bastiaansen, *ACS Appl Mater Interfaces* **2016**, *8*, 17549.
- [23] Y. Chen, J. Qian, X. Liu, Q. Zhuang, Z. Han, *New J Chem* **2013**, *37*, 2500.
- [24] N. Biswas, S. Umopathy, *J Phys Chem A* **2000**, *104*, 2734.
- [25] R. G. Brown, *J Chem Phys* **1963**, *38*, 221.
- [26] C. Bunn, P. Daubeny, P. Division, W. G. City, *Trans. Faraday Soc.* **1954**, *50*, 1173.
- [27] A. J. Angstrom, *Annalen der Physik und Chemie* **1861**, *114*, 33.
- [28] M. Sato, A. Kumada, K. Hidaka, T. Hirano, F. Sato, *Appl Phys Lett* **2017**, *110*, 092923.
- [29] G. C. Yu, L. Z. Wu, L. J. Feng, *Mater Des* **2015**, *88*, 1063.
- [30] J. Doychak, *Jom* **1992**, *44*, 46.
- [31] H. Ghasemi, N. Thoppey, X. Huang, J. Loomis, X. Li, J. Tong, J. Wang, G. Chen, *Fourteenth Intersociety Conference on Thermal and Thermomechanical Phenomena in Electronic Systems (ITherm)*. IEEE Orlando, Florida, USA **2014**, pp. 235-239.

Chapter 3

- [32] B. Wunderlich, G. Czornyj, *Macromolecules* **1977**, *10*, 906.
- [33] H. Y. Chen, M. T. Bishop, B. G. Landes, S. P. Chum, *J Appl Polym Sci* **2006**, *101*, 898.

Chapter 4

Enhanced thermal conductivity in oriented polyvinyl alcohol/graphene oxide composites



Abstract Polymer composites have attracted increasing interest as thermal management materials for use in devices owing to their ease of processing and potential lower costs. However, most polymer composites have only modest thermal conductivities, even at high concentrations of additives, resulting in high costs and reduced mechanical properties, which limit their applications. To achieve high thermally conductive polymer materials with a low concentration of additives, anisotropic, solid-state drawn composite films were prepared using water-soluble polyvinyl alcohol (PVA) and dispersible graphene oxide (GO). A co-additive (sodium dodecyl benzenesulfonate) was used to improve both the dispersion of GO and consequently the thermal conductivity. The hydrogen bonding between GO and PVA and the simultaneous alignment of GO and PVA in drawn composite films contribute to the improved thermal conductivity ($\sim 25 \text{ W m}^{-1} \text{ K}^{-1}$), which is higher than most reported polymer composites and approximately 50-fold enhancement over isotropic PVA ($0.3\text{-}0.5 \text{ W m}^{-1} \text{ K}^{-1}$). This work provides a new method to prepare water-processable, drawn polymer composite films with high thermal conductivity which may be useful for thermal management applications.

This chapter is largely reproduced from:

Pan, X., Debijs, M. G., Schenning, A. P. H. J., & Bastiaansen, C. W. M. Enhanced Thermal Conductivity in Oriented Polyvinyl Alcohol/Graphene Oxide Composites. *ACS Applied Materials & Interfaces*, (Accepted)

4.1 Introduction

Due to their ease of processing, high corrosion and electrical resistances, and relatively low costs and weight, polymers are widely used in daily life.^[1-3] However, bulk polymers generally have relatively low thermal conductivities (usually $< 1 \text{ W m}^{-1} \text{ K}^{-1}$), which limits their application as thermal management materials for heat exchangers, electronic devices, and solar cells, for example (see in **Chapter 1**).^[3-7]

The thermal conductivity of polymers can be enhanced by adding fillers with high thermal conductivity.^[3-10] Typically, thermally conductive nano-carbon materials including graphite nanoplatelets, carbon nanotubes, graphene, and their derivatives are blended as additives into the polymer matrix to achieve an increased thermal conductivity.^[4,6,8] Still, the thermal conductivity of isotropic polymer composites with a high concentration of additives is $< 10 \text{ W m}^{-1} \text{ K}^{-1}$ due to the poor compatibility and interaction between the polymer matrix and additives, resulting in poor dispersion of the additives and serious phonon scattering,^[3-6] as well deterioration of the mechanical properties of the composites.

Recently, high thermal conductivities in anisotropic polymers, including polyethylene (PE) microfilms and micro/nano-fibers,^[10-14] polyvinyl alcohol (PVA) microfilms,^[15-17] polyamide nano-fibers,^[18] and their composite films, have been demonstrated via high degrees of chain orientation, chain extension, and crystallinity. For instance, stretched polyethylene containing graphene nanoplatelets (draw ratio of ~ 5) showed a thermal conductivity of $\sim 6 \text{ W m}^{-1} \text{ K}^{-1}$ with weak van der Waals interaction at the interfaces between the polyethylene and graphene nanoplatelets.⁷ Combined high thermal conductivity ($\sim 75 \text{ W m}^{-1} \text{ K}^{-1}$) and visible transparency were obtained using polyethylene with 0.1 wt% graphene and a compatibilizer (2-(2H-benzotriazol-2-yl)-4,6-ditertpentylphenol, BZT) at a draw ratio of 100 (see in **Chapter 3**).^[9]

As previously reported, enhanced intermolecular interactions between the polymer chains and the additives are an advantage for obtaining high thermal conductivity in drawn composite films (see in **Chapter 1**).^[9,19-21] While anisotropic polymer composites with high thermal conductivities have been reported for stretched polyethylene, to date studies of more polar anisotropic polymer composites, like PVA films employing green processes (that is, avoiding organic solvents) have been less prevalent. PVA is an atactic, water-soluble polymer with an orthorhombic unit cell and planar zigzag configuration similar to polyethylene, resulting in dense packing in the crystal lattice with a high theoretical modulus, strength, and thermal conductivity.^[16,22,23]

4.2 Results and Discussion

To obtain homogeneous PVA/GO composite films, PVA, GO and SDBS were employed (**Figure 4.1**). SDBS, which has a high melting point ($\sim 200 \text{ }^\circ\text{C}$), was included as a compatibilizer, while GO was used instead of graphene to enhance the dispersion in PVA.

Enhanced thermal conductivity in oriented polyvinyl alcohol/graphene oxide composites

The resulting solution/dispersion was poured into polystyrene molds and dried at 60 °C for 2 days. The composite films were then stretched at 130 °C with a draw ratio of ~ 5. The effects of GO (0-5 wt%) and SDBS (0-5 wt%) concentrations and draw ratio were systematically studied in the drawn polymer films (see **Table 4.1**: for this paper, the nomenclature PVA-*n* generally represents a drawn PVA composite film containing *n* wt% GO, variable amounts of SDBS, and drawn to a ratio of 5). Higher concentrations of GO (> 5 wt%) were not studied due to the generally poor dispersion and stretchability of the composite films.

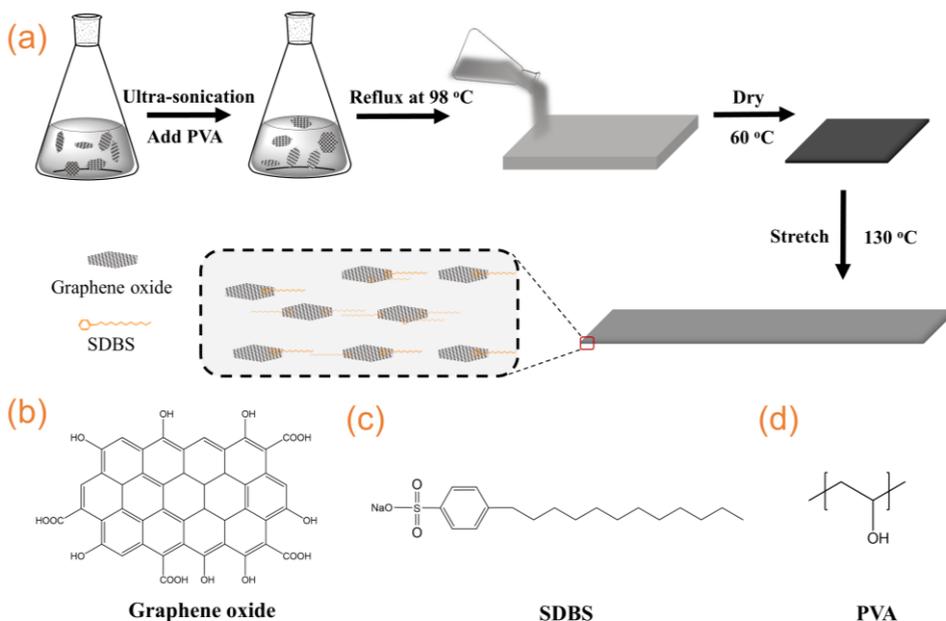


Figure 4.1 a) Fabrication process for drawn PVA composite films. b-d) Chemical structures of graphene oxide (GO, simplified chemical structure), sodium dodecyl benzenesulfonate (SDBS), and PVA.

The thermal conductivities of the drawn PVA/GO composite films were measured as a function of the concentration of GO (**Figure 4.2a**), revealing that the thermal conductivity increases with increasing concentration of GO. The highest thermal conductivity, ~ 25 W m⁻¹ K⁻¹, was obtained with drawn PVA-5, exhibiting approximately three times the thermal conductivity of drawn neat PVA-0 films, and an approximately 50-fold enhancement in thermal conductivity in comparison to pure, isotropic PVA-0 (**Figure 4.2d**).

The role of the SDBS surfactant was also studied (**Figure 4.2a** and **4.b**). The thermal conductivity of drawn PVA-0(2) decreases with the addition of SDBS compared to PVA-0 (**Figure 4.2a**), which may be expected, since the addition of low molecular weight additives

commonly reduces thermal conductivity.^[9] In contrast, adding SDBS (up to 1 wt%) *increases* the thermal conductivity of drawn PVA-5 (compare to PVA-5(2)): further increasing SDBS content to 5 wt% (sample PVA-5(3)) results in the thermal conductivity decreasing again (**Figure 4.2b**). Apparently, adding up to 1 wt% of the surfactant likely enhances the dispersion of GO (**Figure S4.1 and Figure S4.2**), but the poor thermal conductivity of SDBS dominates at higher contents, resulting in an overall lower conductivity. The experimental data in **Figure 4.2** also show that adding GO without SDBS increases the thermal conductivity from ~ 8 to $\sim 16 \text{ W m}^{-1} \text{ K}^{-1}$, which illustrates that the increase in thermal conductivity (from ~ 8 to $\sim 25 \text{ W m}^{-1} \text{ K}^{-1}$, **Figure 4.2a**) originates partly from both additives. The mechanical effects of adding SDBS were examined using DMA (**Figure S4.3**). The results indicate that a high content of SDBS reduces the storage modulus and increases $\tan\delta$. In other words, SDBS behaves as a mechanical plasticizer, especially at high SDBS contents. Please note that a very high SDBS content was used here (5 wt%) which is far higher than the optimum SDBS content (1 wt%). In addition, Young's modulus decreases with the addition of SDBS, while the maximum draw ratio increases (**Table S4.1**), probably further resulting from the addition of SDBS as a plasticizer.

Photographs of undrawn and drawn PVA-5 films are shown in **Figures 4.2c i and ii**. The OM image of the drawn PVA-5 film indicates that the addition of both additives (GO and SDBS) improves the dispersion (compare **Figure S4.2 and Figure 4.2c iii**) although there is aggregation due to the excessive content of GO in PVA films. In **Figure 4.2d**, the thermal conductivity of a wide variety of undrawn and drawn films described in the literature is shown as a function of the content of thermally conductive additives, including graphene, carbon nanotubes, graphene oxide, and mixtures,^[9,10,13,15,16,23–30] revealing the impressive thermal conductivity in drawn PVA-5 films with low additive contents. Drawn PE and PE/GN films showed greater thermal conductivity than drawn PVA/GO films in this work, probably due to the high orientation and crystallinity induced by ultrahigh draw ratios in drawn PE and PE/GN films, which could not be obtained in PVA/GO films.^[10,11]

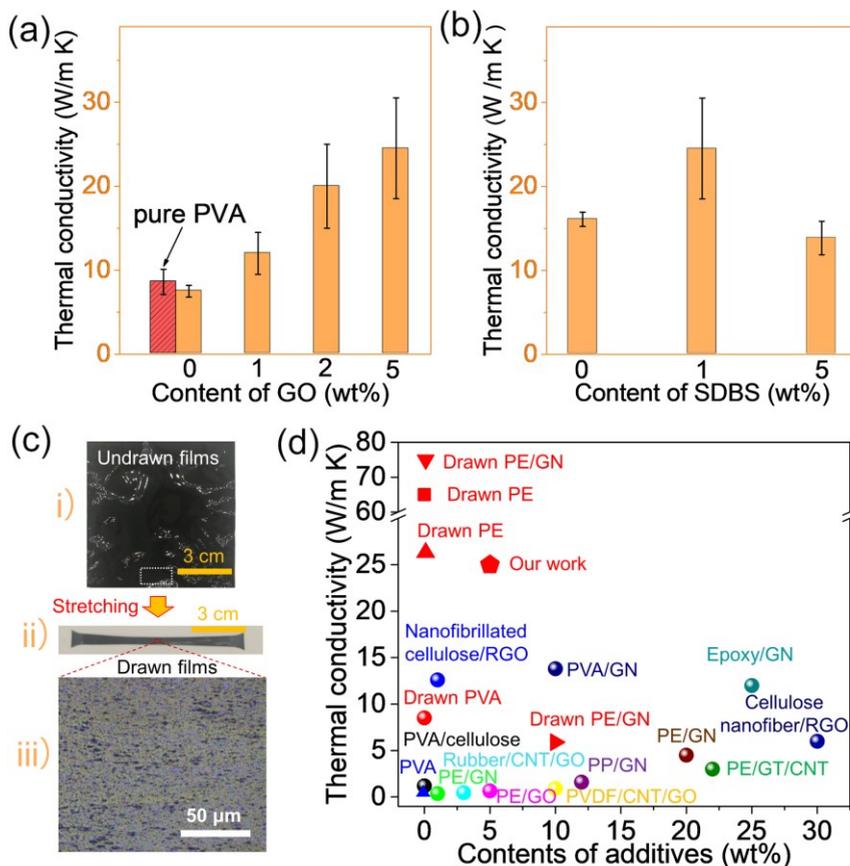


Figure 4.2 a) Thermal conductivity of drawn pure PVA-0 without SDBS (red block), and thermal conductivity of PVA-0(2), PVA-1, PVA-2, and PVA-5 films, each containing 1 wt% SDBS with an increasing GO content. b) Thermal conductivity of drawn PVA-5(2), PVA-5, and PVA-5(3) films containing variable concentrations of SDBS with 5 wt% of GO. c) Photographs of undrawn (i) and drawn (ii) PVA-5 films, and OM image (iii) of drawn PVA-5 films. d) Thermal conductivities reported for different films in the literature.^[9,10,13,15,16,23–30] The x-axis represents the wt% contents of the thermally conductive additives. The red symbols represent drawn polymers or composites. Here, GN, RGO, GT, CNT, and PVDF represent graphene, reduced graphene oxide, graphite, carbon nanotube, and polyvinylidene fluoride, respectively.

WAXS was performed to further analyze the drawn PVA/GO films (**Figure 4.3a-d**). Undrawn PVA-0 films without additives show two scattering rings of lattice planes of (101) at $2\theta \sim 19.5^\circ$ and (100) at $2\theta \sim 11.6^\circ$, corresponding to the PVA crystalline domains (**Figure 4.3a**), while these scattering rings coalesce into scattering dots in drawn PVA films (**Figure 4.3b**), indicating some alignment of PVA crystalline domains. A significant amorphous halo is also observed in both films, indicating little orientation, to be expected at these low draw ratios.

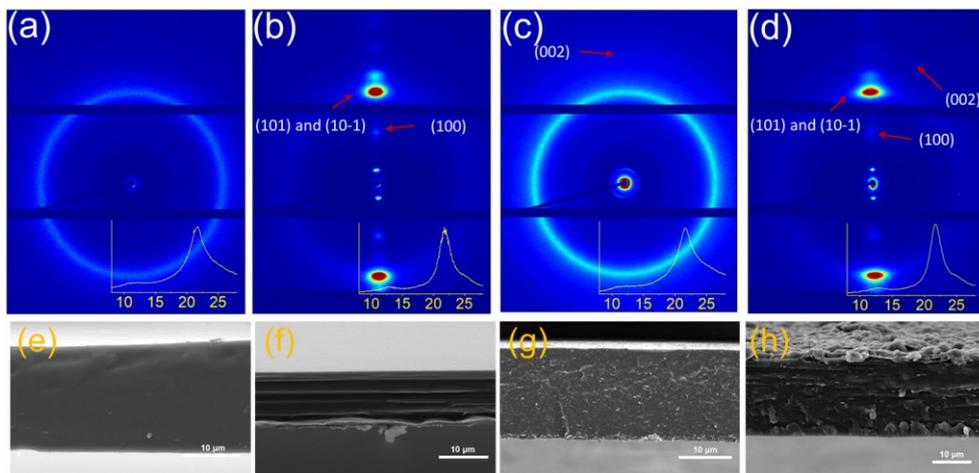


Figure 4.3 WAXS patterns of drawn PVA-0 (a) and drawn PVA-5 (b) composite films. The insets are the 1-D curves of X-ray scattering. Here, the plane of measured films is perpendicular to the incident X-ray (**Figure S4.4b**). SEM images of the cross-section of drawn PVA-0 (c) and drawn PVA-5 (d) composite films. e) Non-polarized FTIR spectra of drawn PVA-0, PVA-0(2), and PVA-5.

In the case of the polymer composite films, the scattering rings of PVA (at 11.6° and 19.5°) (**Figure 4.3c**) also transform into scattering dots upon stretching (**Figure 4.3d**), revealing alignment of PVA and suggesting low through-plane alignment of GO although the scattering rings of GO (lattice plane: (002), $2\theta: \sim 25.5^\circ$) transform into weak scattering arcs (**Figure 4.3d**). The Herman's orientation function calculated by the full width at half maximum (FWHM)^[24,25] reveals that both the drawn PVA films with and without graphene (PVA-0 and PVA-5) have a high degree of orientation (~ 0.9) of the crystalline domains of PVA, indicating there is no obvious effect of adding GO and SDBS. Anisotropy of SDBS in drawn PVA-5 films was also observed in the WAXS patterns due to the fact that the scattering rings of SDBS in undrawn films (**Figure 4.3c**) transfer into dots in drawn films (**Figure 4.4d**). **Figure S4.4c** reveals anisotropic GO in the plane of drawn PVA-5 films. These results suggest drawing-induced, simultaneous alignment of PVA and GO, similar to drawn PE and graphene films in the literature.^[8,16] In the cross-section of the SEM (**Figure 4.3e-f** and **Figure S4.2**), the drawn PVA-0 and PVA-5 films show more aligned and fibrillar structures than undrawn PVA-0 and PVA-5 films (**Figure 4.3f** and **Figure 4.3h**). Homogeneous dispersion of GO in PVA-5 films was observed in **Figure S4.2a** and **b**; the morphology of GO was characterized in **Figure S4.2c** and **d**, indicating that the size of GO is smaller than $2\ \mu\text{m}$, which is smaller than that in **Figure 2**, probably due to aggregation, or the interlayer splitting induced by stretching.^[16]

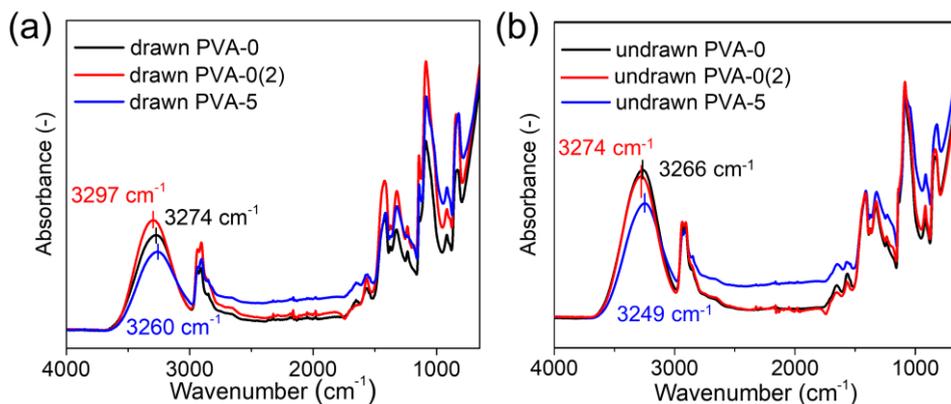


Figure 4.4 (a) Non-polarized FTIR spectra of drawn PVA-0, PVA-0(2), and PVA-5. (b) Non-polarized FTIR spectra of undrawn PVA-0, PVA-0(2), and PVA-5.

The interaction between PVA and the additives was investigated using infra-red spectroscopy. FTIR spectra of drawn PVA-0 films with and without 1 wt% SDBS (**Figure 4.4**) show vibration peaks at ~ 3274 and 3297 cm^{-1} , respectively, attributed to the -OH group of the PVA. In contrast, the drawn PVA films with 5 wt% GO and 1 wt% SDBS show a red-shifted (to lower energies/wavenumber) peak at ~ 3260 cm^{-1} , indicating the hydrogen bonding interaction between GO and PVA (**Figure 4.4a**).^[16,31,32] Although WAXS results indicate the orientation of the PVA chains, there is no obvious orientation of hydrogen bonding in the polarized FTIR spectra, consistent with previous literature reports.^[17] There is a drawing-induced shift to higher energies/wavenumber of the absorption peak of -OH in both PVA-0 and PVA-5 films in comparison with the undrawn PVA-0 and PVA-5 films, respectively (**Figure 4.4b**), as reported undrawn and drawn polyacrylonitrile, and PVA in the literature.^[33,34]

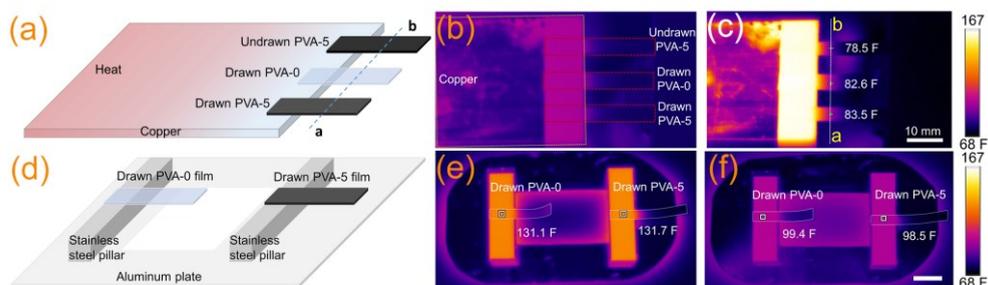


Figure 4.5 Schematic pictures of thermal analysis module in the heating (a) and cooling (d) processes. b-c) Thermal analysis of undrawn PVA-5, drawn PVA-0, and drawn PVA-5 films of similar sizes (highlighted by the dotted red boxes) during the heating process. e-f) Thermal analysis of the drawn PVA-0 and PVA-5 films (highlighted by the dotted white boxes) during the cooling process. F is Fahrenheit.

Simple setups were created to do a basic thermal analysis of representative composite films and to explore their potential application as heat transport and heat release elements (**Figure 4.5**). First, the ends of three films are fixed to the right end of a copper plate, and the left end of the copper plate was exposed to 194 F (80 °C) at time = 0 minutes (**Figure 4.5b**). After 2 minutes, the drawn PVA-5 film shows the highest temperature, while the undrawn PVA-5 film exhibits the lowest temperature at the same position (**Figure 4.5c**), indicating higher thermal transport and thermal conductivity in drawn PVA-5 film compared to both drawn PVA-0 and undrawn PVA-5 films. After heating, a cooling experiment was conducted to help clarify the heat release process of the composite films (**Figure 4.5d-f**). For the cooling measurement, the ends of two drawn films, one PVA-0 and the other PVA-5, were fixed atop stainless steel pillars as shown in **Figures 4.5d**, and exposed to 194 F (80 °C) for 10 minutes, before removing the entire setup to ambient conditions, and the decrease in sample temperature was recorded (**Figure 4.5e**). The drawn PVA-5 film exhibited a higher temperature decrease and a lower final temperature after 2 minutes than the drawn PVA-0 film (**Figure 4.5f**), demonstrating the drawn PVA-5 films more effectively release heat, which makes them potentially useful in devices as thermal management materials.

4.3 Conclusions

This work provides a new method to produce water-based polymer drawn films with high thermal conductivity, which are potentially useful for thermal management in electrical devices, like foldable video screens and flexible solar cells.

Oriented PVA/GO composite films were fabricated through water evaporation and solid-state stretching. SEM images and WAXS results reveal the improved dispersion of GO and the high orientation in drawn PVA/GO films when the co-additive (SDBS) is used. FTIR spectra of composite films demonstrated the presence of hydrogen bonding between PVA and GO. These results contributed to the high thermal conductivity of drawn PVA-5 composite films in the drawing direction, which is higher than most composite films, and approximately a 50-fold enhancement in comparison with isotropic PVA.

It is tempting to speculate further on the applications of these films in, for instance, flexible solar cells and foldable video screens. For instance, solar cells usually have an efficiency below 25 % and the residual absorbed energy is transferred into heat. The heating-up of the devices can be quite significant (100 °C) which actually reduces their efficiency and lifetime enormously especially. To satisfy the need in the foldable and flexible devices, the light-density and flexible thermal-conductive polymer composites were presented in this work.

4.4 Experimental section

Materials. PVA flakes (Mw: 146000-186000 Da., 99+% hydrolyzed, CAS number: 9002-89-5, product number: 363065), GO nanoplatelets (brown/black powder, layers: 15-20, edge-oxidization: 4-10%, product number: 796034) and sodium dodecyl benzenesulfonate (SDBS, CAS number: 25155-30-0, product number: 289957) were purchased from Sigma-Aldrich and used without further purification.

Fabrication. GO and SDBS were dispersed in deionized water (50 mL) using ultrasonication (Branson 1510 ultrasonic cleaner, 80 Watts) for 1 hour. The composition of the films after casting and drying is shown in **Table 4.1**. PVA flakes (5 g) were added to the mixture with vigorous stirring at 98 °C and then dissolved with reflux for 4 hours. The mixture was cast into polystyrene Petri dishes with an area of ~ 300 cm². After drying at 60 °C for 2 days, the composite films were drawn at 130 °C to a draw ratio of ~ 5.

Table 4.1. Contents of elements in drawn composite films

Samples	PVA (g)	GO (mg)	SDBS (mg)
PVA-0	5	0	0
PVA-1	5	50	50
PVA-2	5	100	50
PVA-5	5	250	50
PVA-0(2)	5	0	50
PVA-5(2)	5	250	0
PVA-5(3)	5	250	250

Analytical Techniques. The thermal conductivity of drawn composite films along the drawing direction was measured based on the Angstrom method (see in **Chapter 2**).^[9,10] 2D wide-angle X-ray scattering (WAXS) was performed on a Ganesha lab instrument equipped with a Genix-Cu ultralow divergence source producing 0.154 nm X-rays. Diffraction patterns were collected for 15 minutes on a Pilatus 300 K silicon pixel detector. The plane of measured films is perpendicular or parallel to the incident X-ray. The Herman's orientation function of the composite films was calculated from the full width at half maximum (FWHM) of the azimuthally scanned peak.^[24,25] Polarized and non-polarized FTIR spectra were measured on a Varian 670-IR spectrometer equipped with a golden gate setup with and without a polarizer, respectively. Raman scattering spectroscopy was performed on a Raman microscope (Witec Alpha 300 R) using a 532 nm laser. Photographs of composite films were taken using a Canon camera. Optical microscopy (OM) images of samples were performed on a Leica DM 2700M microscope without polarizers. The temperatures of composite films were recorded using an infrared (IR) camera (Fluke®). One end of the drawn films was affixed to one side of a copper plate with a high thermal conductivity with double-sided

Chapter 4

carbon tape (NEM tape, Nisshin EM. Co. Ltd), and the distal edge of the copper plate was placed on a hot plate set to 194 F (80 °C). The temperatures of the films at similar positions were recorded at 0 and 2 minutes after placement on the hot plate. For measurement of the cooling cycle, composite films were attached to the top of stainless-steel pillars with double-sided carbon tape. The pillars were fixed to the surface of an aluminum plate which was heated on a hot plate to 194 F (80 °C) for 10 minutes until thermal equilibrium was attained. Then, the entire assembly was removed from the hot plate and left to cool to room temperature. Stainless steel was used rather than copper to retard the cooling process (due to the lower thermal conductivity of stainless steel compared to copper) so that the difference in temperature between the drawn films could be more easily measured. The cooling measurements were repeated several times to accurately record the temperature of the films drawn with and without additives. Scanning electron microscopy (SEM, JSM-IT100, JEOL, secondary electron detector) images of samples were recorded with a beam current of 10 kV (magnification from 700-3000 ×) after breaking the samples in liquid nitrogen and sputtering with platinum (Pt). Characterization of GO was accomplished by dispersing as powder in alcohol and then dropped on a silicon wafer. After drying, the dispersed GO on the wafer was sputtered for 30 seconds with Pt at a current of 30 mA. Measurement of electrical conductivity of drawn PVA-5 films was performed on a SourceMeter (KEITHLEY, 2400) with a voltage of 10 volts. The mechanical properties of PVA-5 films were performed using dynamic mechanical analysis (DMA) from 25 - 90 °C with a frequency of 1 Hz and a strain of 0.5%, while Young's modulus of drawn PVA composite films was measured at ~ 25.5 °C using DMA.

4.5 References

- [1] R. C. P. Verpaalen, T. Engels, A. P. H. J. Schenning, M. G. Debije, *ACS Appl Mater Interfaces* **2020**, *35*, 38829.
- [2] X. Xu, J. Zhou, J. Chen, *Adv Funct Mater* **2019**, *10*, 1904704.
- [3] C. Huang, X. Qian, R. Yang, *Mater Sci Eng R Reports* **2018**, *132*, 1.
- [4] Z. Han, A. Fina, *Prog Polym Sci* **2011**, *36*, 914.
- [5] H. Chen, V. V. Ginzburg, J. Yang, Y. Yang, W. Liu, Y. Huang, L. Du, B. Chen, *Prog Polym Sci* **2016**, *59*, 41.
- [6] Y. Zhang, Y. J. Heo, Y. R. Son, I. In, K. H. An, B. J. Kim, S. J. Park, *Carbon* **2019**, *142*, 445.
- [7] X. Xu, J. Chen, J. Zhou, B. Li, *Adv Mater* **2018**, *30*, 1705544.
- [8] M. Saeidijavash, J. Garg, B. P. Grady, B. Smith, Z. Li, R. J. Young, F. Tarranum, N. Bel Bekri, *Nanoscale* **2017**, *9*, 12867.
- [9] X. Pan, L. Shen, A. P. H. J. Schenning, C. W. M. Bastiaansen, *Adv Mater* **2019**, *31*, 1904348.
- [10] X. Pan, A. H. P. J. Schenning, L. Shen, C. W. M. Bastiaansen, *Macromolecules* **2020**, *53*, 5599.
- [11] Y. Xu, D. Kraemer, B. Song, Z. Jiang, J. Zhou, J. Loomis, J. Wang, M. Li, H. Ghasemi, X. Huang, X. Li, G. Chen, *Nat Commun* **2019**, *10*, 1771.
- [12] S. Shen, A. Henry, J. Tong, R. Zheng, G. Chen, *Nat Nanotechnol* **2010**, *5*, 251.
- [13] R. Shrestha, P. Li, B. Chatterjee, T. Zheng, X. Wu, Z. Liu, T. Luo, S. Choi, K. Hippalgaonkar, M. P. De Boer, S. Shen, *Nat Commun* **2018**, *9*, 1664.
- [14] R. Shrestha, Y. Luan, S. Shin, T. Zhang, X. Luo, J. S. Lundh, W. Gong, M. R. Bockstaller, S. Choi, T. Luo, R. Chen, K. Hippalgaonkar, S. Shen, *Sci Adv* **2019**, *5*, 3777.
- [15] Y. Park, M. You, J. Shin, S. Ha, D. Kim, M. H. Heo, J. Nah, Y. A. Kim, J. H. Seol, *Sci Rep* **2019**, *9*, 3026.
- [16] Y. Zhuang, K. Zheng, X. Cao, Q. Fan, G. Ye, J. Lu, J. Zhang, Y. Ma, *ACS Nano* **2020**, *14*, 11733.
- [17] A. Chen, Y. Wu, S. Zhou, W. Xu, W. Jiang, Y. Lv, W. Guo, K. Chi, Q. Sun, T. Fu, T. Xie, Y. Zhu, X. Liang, *Mater Adv* **2020**, *1*, 1996.
- [18] H. C. Chien, W. T. Peng, T. H. Chiu, P. H. Wu, Y. J. Liu, C. W. Tu, C. L. Wang, M. C. Lu, *ACS Nano* **2020**, *14*, 2939.
- [19] Y. Xu, X. Wang, J. Zhou, B. Song, Z. Jiang, E. M. Y. Lee, S. Huberman, K. K. Gleason, G. Chen, *Sci Adv* **2018**, *4*, 3031.
- [20] P. Hummel, A. M. Lechner, K. Herrmann, P. Biehl, C. Ro, L. Wiedenho, F. H. Schacher, M. Retsch, *Macromolecules* **2020**, *53*, 5528.
- [21] X. Pan, M. G. Debije, A. P. H. J. Schenning, *ACS Appl Polym Mater* **2021**, *3*, 578.
- [22] K. Yamaura, T. Tanigami, N. Hayashi, K. I. Kosuda, S. Okuda, Y. Takemura, M. Itok, S. Matsuzawa, *J Appl Polym Sci* **1990**, *40*, 905.
- [23] X. Xie, D. Li, T. Tsai, J. Liu, P. V Braun, D. G. Cahill, *Macromolecules* **2016**, *49*, 972.
- [24] T. Yano, Y. Higaki, D. Tao, D. Murakami, M. Kobayashi, N. Ohta, J. I. Koike, M. Horigome, H. Masunaga, H. Ogawa, Y. Ikemoto, T. Moriwaki, A. Takahara, *Polymer* **2012**, *53*, 4702.
- [25] T. Kongkhleng, K. Tashiro, M. Kotaki, S. Chirachanchai, *J Am Chem Soc* **2008**, *130*, 15460.
- [26] E. Tarani, Z. Terzopoulou, D. N. Bikiaris, T. Kyratsi, K. Chrissafis, G. Vourlias, *J Therm Anal Calorim* **2017**, *129*, 1715.
- [27] J. Gu, N. Li, L. Tian, Z. Lv, Q. Zhang, *RSC Adv* **2015**, *5*, 36334.

Chapter 4

- [28] J. Che, K. Wu, Y. Lin, K. Wang, Q. Fu, *Compos Part A Appl Sci Manuf* **2017**, *99*, 32.
- [29] W. Bin Zhang, Z. X. Zhang, J. H. Yang, T. Huang, N. Zhang, X. T. Zheng, Y. Wang, Z. W. Zhou, *Carbon* **2015**, *90*, 242.
- [30] S. Ronca, T. Igarashi, G. Forte, S. Rastogi, *Polym* **2017**, *123*, 203.
- [31] S. Kashyap, S. K. Pratihar, S. K. Behera, *J Alloys Compd* **2016**, *684*, 254.
- [32] J. Li, L. Shao, X. Zhou, Y. Wang, *RSC Adv* **2014**, *4*, 43612.
- [33] L. Dai, L. Ying, *Macromol Mater Eng* **2002**, *287*, 509.
- [34] L. Tan, A. Wan, *Colloids Surfaces A Physicochem Eng Asp* **2011**, *392*, 350.

4.6 Supporting Information

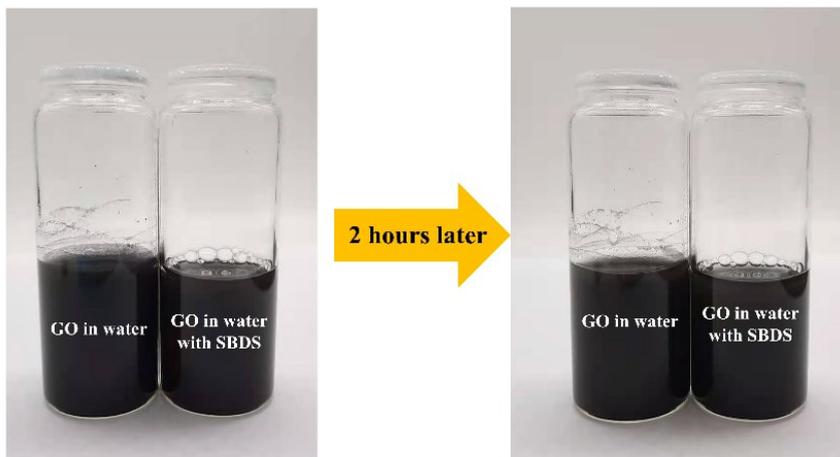


Figure S4.1 GO and GO/SDBS dispersions in water (GO/water: 0.4 mg/mL) immediately and two hours after ultrasonication for 1 hour and then manual shaking twice. There is no obvious sediment of two dispersion after 2 hours, indicating that there is no obvious improved stability of GO after adding SDBS.

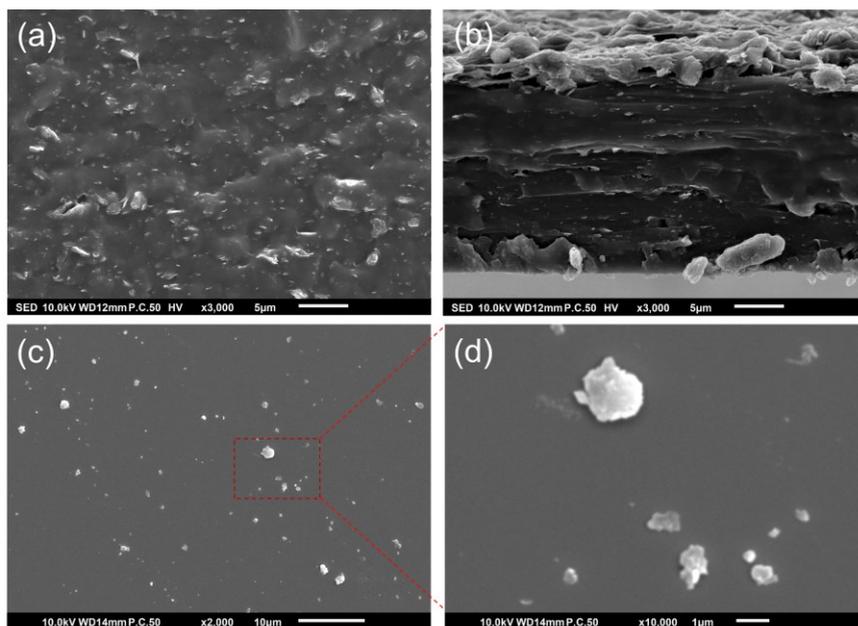


Figure S4.2 SEM images of the cross-section of undrawn (a) and drawn (b) PVA/GO films with a high resolution. SEM images of GO (c and d). Here, d is the zoom-in graph of the indicated region in c.

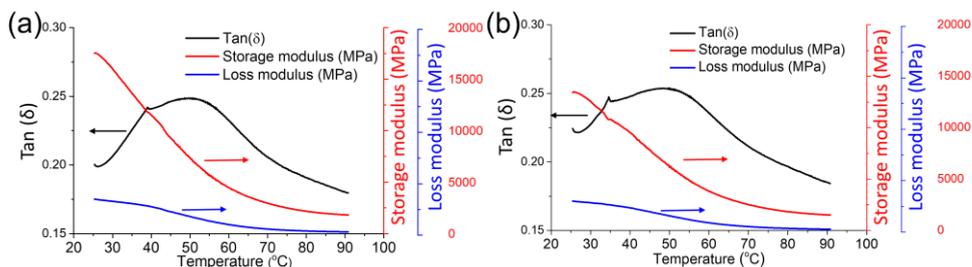


Figure S4.3 DMA of (a) drawn PVA-5 without SDBS (PVA-5(2)) and (b) drawn PVA-5 with 5 wt% SDBS (PVA-5(3)).

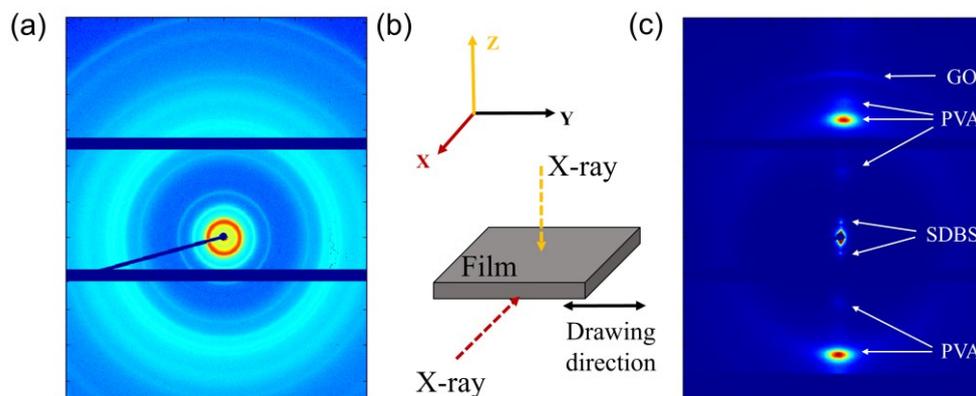


Figure S4.4 (a) WAXS of SDBS powder. The main peak of SDBS is at $2\theta \sim 3.1^\circ$. In combination with Figure 4.3d, this indicates that the SDBS is also oriented in drawn PVA-5 films. (b) Schematic diagram of incident X-ray in WAXS measurement. In Figure 4.3., the incident X-ray (the yellow arrow) is perpendicular to the plane of the films. (c) WAXS of drawn PVA-5 film. The incident X-ray (the red arrow in Figure S4.4b) is parallel to the plane of drawn PVA-5 film, which indicating the anisotropic GO in the plane of drawn PVA-5 films.

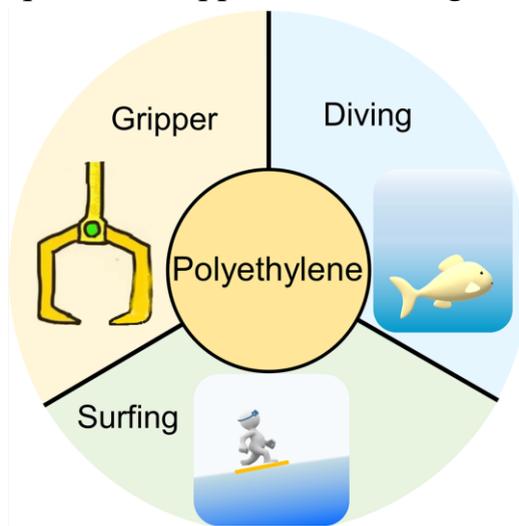
Enhanced thermal conductivity in oriented polyvinyl alcohol/graphene oxide composites

Table S4.1 Mechanical properties of drawn PVA-5 films without and with 5 wt% SDBS.

Films	PVA-5 without SDBS			PVA-5 with 5 wt% SDBS		
	1	2	3	1	2	3
3 samples in each film						
Draw ratio _{max} (λ_m)	5.0	5.1	5.5	6.0	5.6	5.8
Average λ_m	5.2			5.8		
Young's modulus (GPa)	~ 25.4			~ 15.9		

Chapter 5

Three-Dimensional Anisotropic Polyethylene as Light-Responsive Grippers and Surfing Divers



Abstract Untethered soft actuators are usually based on three-dimensional (3D) engineered special polymers such as liquid crystal networks or hydrogels that require complex fabrication methods. Here, an easy-to-process, anisotropic composite soft actuator based on a simple photothermal dye-doped polyethylene film is presented. The 3D anisotropic polymer films are prepared by solution-casting and subsequent thermal solid-stretching. The resulting soft actuators exhibit large and controllable bending in response to light (UV and/or near-infrared (NIR)) stimuli and are able to act as grippers picking up cargo. Additionally, the films are capable of realizing “diving” and “surfing” locomotion in and over a liquid via the photothermal induced Marangoni effect, yielding a NIR light-fueled transporter able to pick up cargo. The results open up new possibilities of using commodity polymers in a broad range of applications including untethered soft actuators and robotic devices.

This chapter is largely reproduced from:

Pan, X., Grossiord, N., Sol, J. A. H. P., Debije, M. G. & Schenning, A. P. H. J. Three-dimensional Anisotropic Polyethylene as Light-responsive Grippers and Surfing divers. *Advanced Functional Materials*, 2021, 31, 2100465.

5.1 Introduction

Commodity polymers, including polyethylene (PE), polystyrene, and polypropylene, are widely used in daily life at large scales.^[1] These low-density, low-cost polymers typically only exhibit static properties.^[1–3] Recently, stimuli-responsive polymers with functional properties that change in response to external stimuli have received considerable attention.^[4–6] Making commodity polymers stimuli-responsive is appealing and interesting for a broad range of applications such as soft actuators.^[1]

Inspired by nature, soft actuators have attracted ever-increasing attention, like electrochemical,^[7,8] electrothermal,^[9,10] thermal,^[11] acoustic,^[12] and especially photoresponsive actuators due to their wireless control and visual actuation.^[3,13–16] Photoresponsive soft actuators such as grippers, swimmers, and transporters^[4,17–20] have been developed using primarily specialty three-dimensional (3D) anisotropic polymers such as liquid crystal networks, hydrogels, or other engineering polymers,^[3,21–27] and the devices are often engineered by complex fabrication methods.

Recently, commodity polymers have also been used for fabricating untethered soft actuators^[1] where they are combined with liquid crystal networks,^[17–19,28] carbon materials,^[29] or hydrogels^[25,26] to create anisotropic composite or bilayer actuators capable of bending. For twisting and curling, the bilayers need to be cut at oblique angles relative to the molecular alignment.^[13,20,29–32] For instance, bilayer actuators have been described displaying photothermal-induced bending and rolling as a result of the difference in the thermal expansion coefficients of the two layers.^[29] Bilayer actuators have also been reported exhibiting a surfing-like motion over a liquid surface.^[20] Despite this, these untethered soft robots are limited by complex manufacturing procedures and limited robustness due to the use of multiple layers.

An appealing alternative is to prepare light-responsive single-layer polymer composite actuators without using a photo-responsive polymer layer. Blending light-responsive additives into the polymer is compatible with high-throughput industrial processes, and the additives themselves are protected by the robust commodity polymer.^[20,31,33,34] Recently, commodity polymer composite actuators containing light-responsive additives are reported showing only simple UV light-induced stress change with very small 2-dimensional shape changes (< 1%).^[35–37] However, fabrication of single-layer actuators with 3D, multiple actuation modes such as bending, curling, and cargo transport remains challenging and requires programmable 3D structured anisotropic commodity polymers.^[1]

5.2 Results and Discussion

5.2.1 Preparation of the photothermal actuators

For the free-standing anisotropic graded PE composite films (PE-BZT-GN-QR), graphene nanoplates (GN), 2-(2H-benzotriazol-2-yl)-4,6-ditertpentylphenol (BZT, also Tinuvin® 328), and quaterrylene-based (QR) near-infrared (NIR) dye Lumogen® IR 788 were used as additives. BZT and GN were added to increase the thermal conductivity and improve the response speed of actuators, and simultaneously acting as UV absorbing photothermal additives, while Lumogen® IR 788 was added as a NIR absorbing photothermal dye.^[38,39] When one of the additives is omitted the performance of the actuators and robotic devices are suboptimal (vide infra). The films were fabricated by solution-casting in which the additives are mixed with PE in xylene and poured into a mold (**Figure 5.1a**). After drying, the resulting films were stretched at 120 °C to different draw ratios and remained flat after quickly cooling to room temperature. Thermal conductivity measurements reveal that the stretched PE-BZT-GN-QR composite films show high anisotropic one-dimensional thermal conductivity along the stretching direction. The absorption spectrum of the films shows two NIR absorption peaks between 600 to 900 nm and a UV absorption band below 400 nm, with transmission at 550 nm being approximately 80%. The NIR absorption bands are attributed to the photothermal Lumogen® IR 788 dye while the absorption band below 400 nm results from the combination of all three additives (**Figure 5.1b**).

Remarkably, after cutting long strips from stretched film perpendicular to the stretching direction, the flat film with a draw ratio of 30 bends into a roll, whereas a film strip cut parallel to the draw direction shows no obvious bending (**Figure 5.1c**). Film strips cut at a 45° angle to the stretching axis of the PE film exhibit a right-handed curl. In both the bent and curled films, the top side (exposed to air during fabrication) of the film is always inside the deformation. The shape of films that were stretched with lower draw ratios and cut under 90° and 45° angles displayed less bending and curling. The composite films with a draw ratio of 20 cut at 0° angle are slightly bent, while the film with a draw ratio of 10 is flat. We measured the temperature response of a free-standing PE-BZT-GN-QR bent composite film strip. The size of this ~5 μm thick strip with a draw ratio of ~ 40 was approximately 3 × 1 cm², cut perpendicular to the stretching direction (90°, $y \times x$ in **Figure 5.1c**). At room temperature, the films rolled up with a curvature of several hundred degrees. The films were actuated over the temperature range of 20-80 °C in an oven (**Figure 5.1d**). As the temperature increased to 80 °C, the films gradually unrolled. The thermally induced unrolling reveals that the expansion of the top side of polymer composite is greater than the bottom side; that is, there is a larger coefficient of thermal expansion (CTE) at the top.

Chapter 5

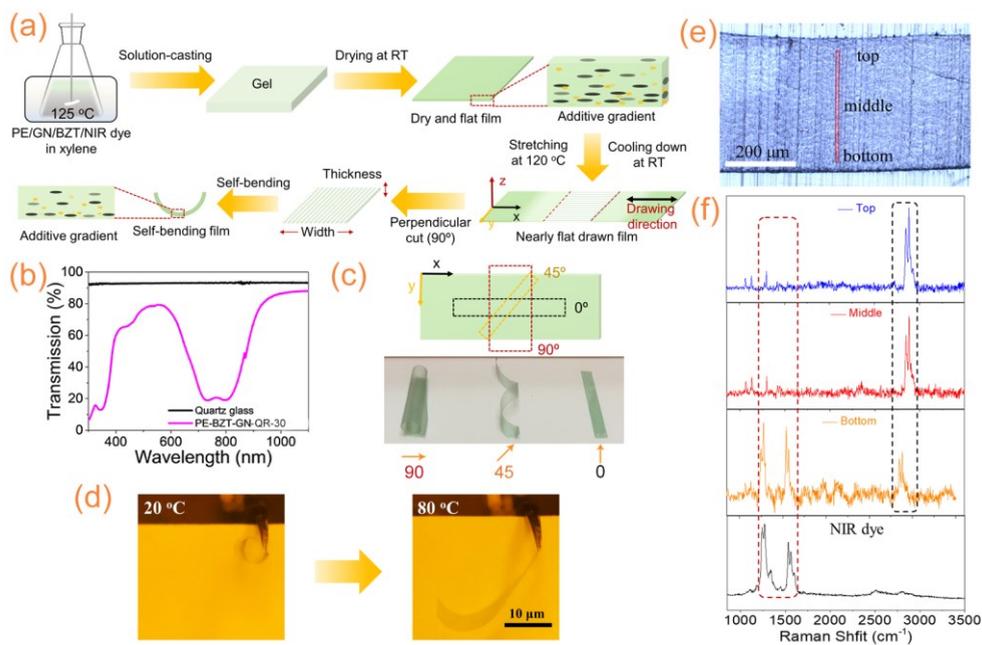


Figure 5.1 a) Fabrication process of thermally drawn PE-BZT-GN-QR dye composite films. b) UV-vis spectra of quartz glass and PE-BZT-GN-QR film (baseline: air). c) Optical images of drawn PE-BZT-GN-QR composite films with different angles between cutting and drawing directions (90°, 45°, and 0° are defined using red, orange, and black boxes). The orange arrow indicates the drawing direction. d) Thermal response of PE-BZT-GN-QR film in the air from 20–80 °C. The size of the PE-BZT-GN-QR composite film is approximately 3×1 (y×x) cm² and the thickness is about 5 μm with a draw ratio of 40, respectively. e) Raman mapping of the cross-section of undrawn PE-BZT-GN-QR films. f) Raman spectra of the cross-section of undrawn PE-BZT-GN-QR films at different positions in Figure 1d and pure NIR dye. The reference peaks are the peak of -CH₂.

To understand the bending and curling of the strips immediately after cutting from the larger film, a cross-section of the undrawn, flat PE-BZT-GN-QR composite film was characterized by Raman scattering spectroscopy^[40] (**Figure 5.1e** and **f**). The distribution of NIR photothermal dye was determined by mapping the $\tilde{\nu} = 1570 \text{ cm}^{-1}$ (**Figure 5.1e**, marked red region). The results suggest that the concentration of NIR dye increases through the depth of the film from the top to bottom surfaces, likely owing to dye migration during the solvent evaporation during the drying of the composite film (**Figure 5.1a**). It is likely that similar concentration gradients are present in the PE composite films for the BZT and GN additives, but unfortunately, no clear vibrational bands were visible in the Raman spectra.

Drawn PE films display lower moduli and larger, positive CTE (expansion, $(\alpha_{\perp}) > 0$) perpendicular to the drawing direction than parallel to the drawing direction, which shows higher moduli and smaller, negative CTEs (contraction, $(\alpha_{\parallel}) < 0$).^[41] The modulus in the parallel direction depends on the draw ratio and increases upon further stretching.^[42] The

Three-dimensional anisotropic polyethylene as light-responsive grippers and surfing divers

addition of additives with relatively low CTEs into PE films lowers the composite CTE: upon the increasing concentration of additives, the CTE will be lower at the bottom side of the film due to the gradient of additives through the depth of the films.^[43,44] Our composite films are nearly flat after drawing at 120 °C and stress is likely built up as a result of a CTE mismatch upon cooling, yet the film remains flat. After cutting a strip with the length parallel to the drawing direction, the high modulus apparently hinders bending, whereas cutting out a strip in the perpendicular direction releases the stress and bending occurs due to the relatively low modulus. Based on the temperature response of the actuator, the top side (with a lower concentration of additives) of the film has a larger absolute value for the CTE than the bottom side (with a high concentration of additives). Thus, the bending of the drawn PE-BZT-GN-QR composite film from the bottom (outside) to the top (inside) can be attributed to the differential CTE induced by the concentration gradient of additives. Composite films with lower draw ratios are thicker, which affects bending characteristics. In the case of cutting strips out parallel to the drawing direction of the film with a draw ratio of 20, there is only slight bending while for a draw ratio of 10 the film is too thick to induce any bending at all. Overall, these results reveal that 3D, anisotropic, single-layer polymer actuators can be fabricated in which the shape changes can be controlled by the degree of stretching and cutting direction.

5.2.2 Photoresponsive actuators

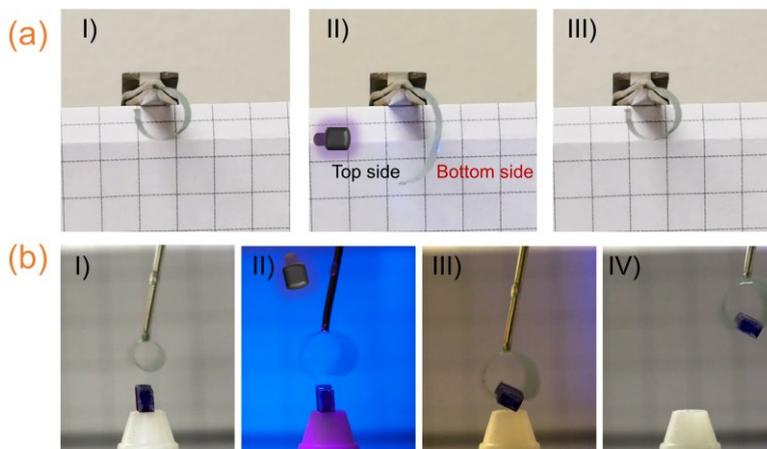


Figure 5.2 a) UV-NIR response of drawn PE-BZT-GN-QR films exposed to light (incident light from the right, I-II-III: light off-on-off); b) Soft robot of PE-BZT-GN-QR films under UV-NIR light (I-II-III-IV: light on-on-off-off). Here, the intensities of UV (365 nm) and NIR (780 nm) light are approximately 120 and 90 mW cm^{-2} , respectively. The size of the composite film is approximately $1.5 \times 1.5 \text{ cm}^2$ and the thickness is about $8 \mu\text{m}$ with a draw ratio of ~ 30 .

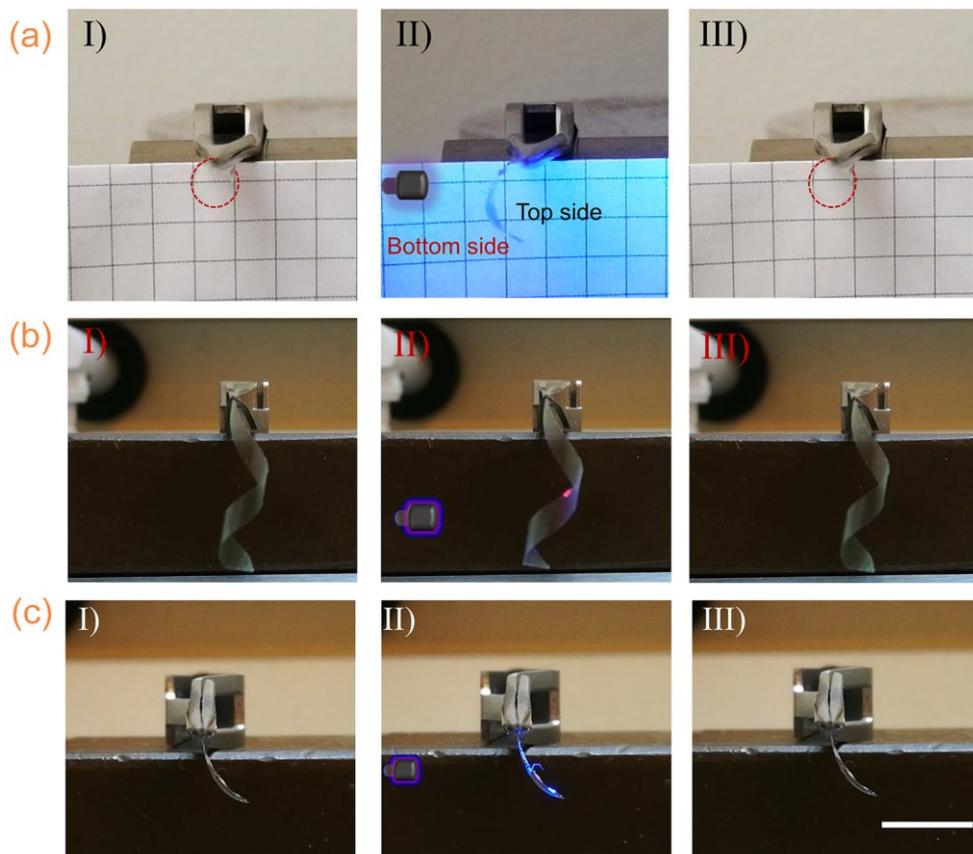


Figure 5.3 Photo-response of PE-BZT-GN-QR composite film with (a) 90 and (b) 45 degrees cutting under UV and NIR light (incident from the left, I-II-III: light off-on-off). The size of PE-BZT-GN-QR composite film with 90 degrees cutting is approximately $1.5 \times 1.5 \text{ cm}^2$ and the thickness is about $8 \text{ }\mu\text{m}$. The size before cutting of PE-BZT-GN-QR composite film with 45 degrees cutting is about $3 \times 3 \text{ cm}^2$ and thickness $\sim 4 \text{ }\mu\text{m}$. The draw ratios of the films are around 30. (c) Photo-response of pure PE film with 90 degrees cutting under UV and NIR light (light towards the right, I-II-III: light off-on-off). The scale bar is 20 mm.

Having characterized the composite films, we studied the light response of the actuators that were cut at an angle of 90° with a draw ratio of ~ 30 (thickness: $\sim 8 \text{ }\mu\text{m}$). UV and NIR light (365 and 780 nm) were used simultaneously as the intensity of NIR or UV light was not sufficient to achieve large shape deformations of the film in the air. The $1.5 \times 1.5 \text{ cm}^2$ PE-BZT-GN-QR composite film has a bending angle of 350° at room temperature in the absence of light irradiation. The unrolling occurs within 2 s upon UV and NIR light irradiation (**Figure 5.2a**). After turning off both UV and NIR lights, the PE-BZT-GN-QR composite film returns to the initial state in 1 s. When the films are exposed from the left side, the unbending of the films is in the opposite direction, indicating that the unbending actuation is

Three-dimensional anisotropic polyethylene as light-responsive grippers and surfing divers independent of the location of the light source but generated by the additive gradient in the composite film (**Figure 5.3a**). Polymer actuators cut under a 45° angle can also be driven under light stimuli and show unrolling from twist under UV and NIR light (**Figure 5.3b**) while the film with a draw ratio lower than 30 is hardly bent. The composite film cut under a 90° angle shows a similar deformation with light and temperature as a stimulus, indicating that the light-induced bending is initiated by the photothermal effect (**Figure 5.2a** and **Figure 5.3a**). As a control, a pure PE film was illuminated but did not show any obvious actuation under the same illumination conditions (**Figure 5.3c**). The bending/unbending deformation of the composite film could be used to fabricate a light-responsive gripper. The gripper opens under light irradiation and then seizes the object after switching off the lights and lifts an object 20 times its own weight (**Figure 5.2b**).

5.2.3 NIR light diving-surfer

The ascending/surfing/diving locomotion of the PE-BZT-GN-QR composite film was performed in isopropanol under NIR or UV light irradiation (**Figure 5.4**). To achieve locomotion, a new composite film with a bending angle less than 180° was driven under NIR or UV light (the intensities of UV and NIR light are 120 and 90 mW cm⁻², respectively), as a single light source is enough to drive the film in the liquid. The size of the composite film is approximately 1×1 cm² with a thickness of approximately 10 μm with a draw ratio of ~30. In the initial state, the PE-BZT-GN-QR film remains at the bottom of the isopropanol bath, as the density (0.98 g cm⁻³) of the composite film is higher than that (0.79 g cm⁻³) of the isopropanol (**Figure 5.4a I** and **figure 5.4b I**). Under NIR light irradiation, the film rises from the bottom to the surface (**Figure 5.4a II-IV** and **Figure 5.4c I-III**). It should be noted that this motion also could be initiated by exposure to UV light (**Figure 5.4b**). After arriving at the surface, the film ‘surfs’ into the dark following the direction perpendicular to the drawing direction of the film (**Figure 5.4c III-V**), similar to the ‘surfing’ of liquid crystal polymer films.^[27] The film sinks after several seconds when the light is switched off.

To study if the surfing locomotion (circle and straight line) can be directed, the location of the NIR light spot was changed (**Figure 5.4d** and **e**). Under NIR light irradiation, the film ascends first from the bottom and then ‘surfs’, following the circle of the light spot. The movement is essentially a ‘push’ by the light spot and controlled by the irradiation position on the film. The velocity of locomotion was measured following the straight-line light motion (**Figure 5.4e**). The surfing velocity attained is at least 2.5 mm s⁻¹ in isopropanol under NIR light irradiation. Remarkably, during the entire diving/ascending and surfing processes, the shape of the PE-BZT-GN-QR composite film did not noticeably change.

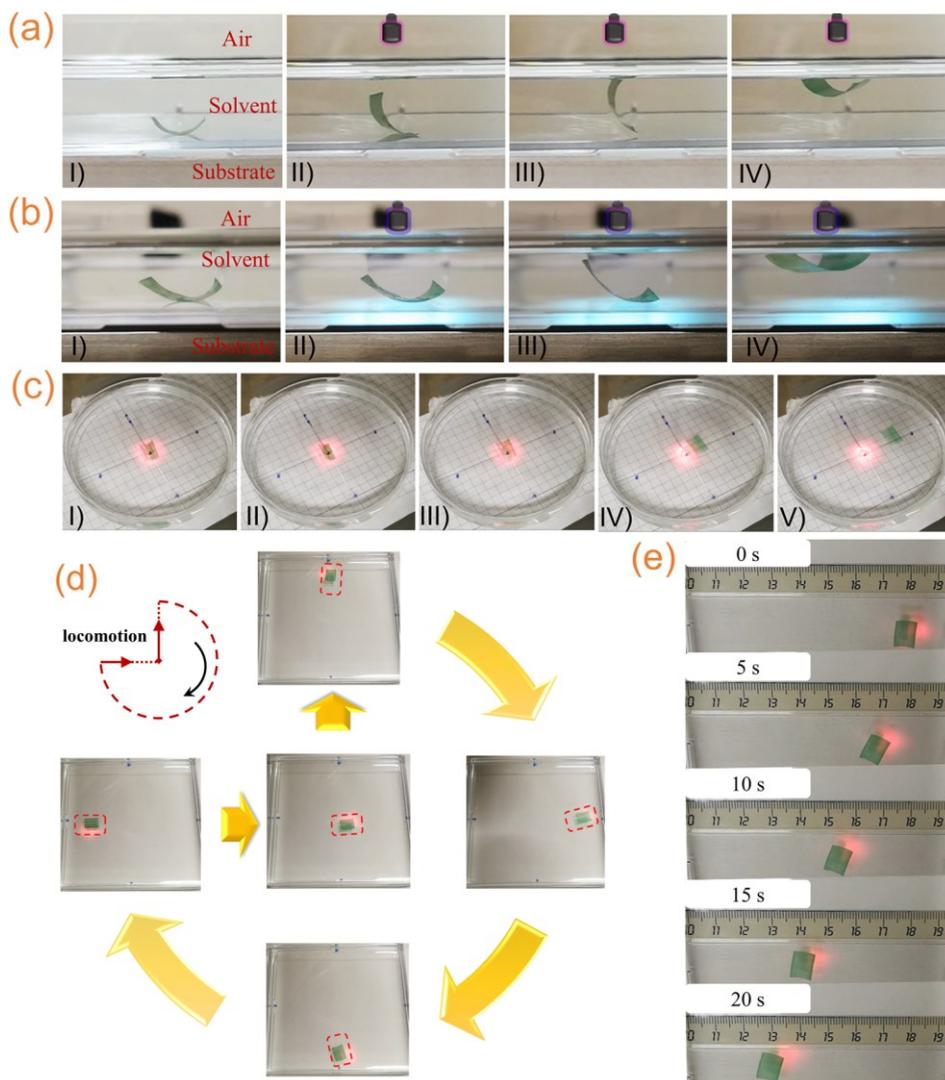


Figure 5.4 Front view of ascending motion of PE-BZT-GN-QR film under a) NIR (780 nm) and b) UV (365 nm) light irradiation. c) Top view of diving (I-III) and surfing (III-V) locomotion of PE-BZT-GN-QR film under NIR light. d-e) Controllable cycle and straight locomotion of PE-BZT-GN-QR film under NIR light. Here, the solvent is isopropanol. Here, the intensities of UV (365 nm) and NIR (780 nm) light are approximately 120 and 90 mW cm^{-2} , respectively.

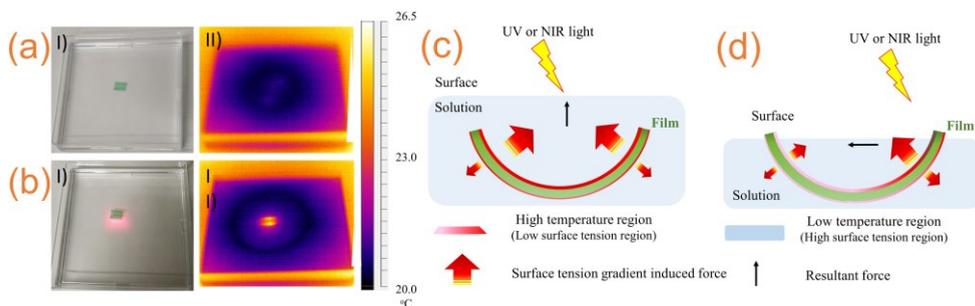


Figure 5.5 Optical (I) and IR (infrared, II) images of the PE-BZT-GN-QR composite film bent concave up in isopropanol without NIR light illumination (a) and on the surface of isopropanol under NIR light illumination (b). Mechanism of locomotion of PE-BZT-GN-QR composite film under light irradiation in isopropanol (c) and on the surface of isopropanol (d).

The temperatures of a PE-BZT-GN-QR composite film upon NIR light illumination were characterized by an IR camera. It was observed that the PE-BZT-GN-QR composite film under NIR light illumination is approximately 5 °C warmer than its surroundings, causing a temperature gradient around the film as the solvent is also heated by the film (**Figure 5.5 a and b**). As a result, the film and surrounding solvent are pushed from the lower temperature/higher surface tension area to the higher temperature/lower surface tension area (**Figure 5.5c and d**). This surface tension gradient was calculated to be of the order of 0.60-0.65 mN m⁻¹. The force induced by the Marangoni effect, which most likely is the origin of the locomotion of the film, was estimated to be equal to a couple of tens of μN.

5.2.4 Photo-fueled cargo displacement at liquid surfaces

The 3D anisotropic polyethylene surfer can be used as an untethered cargo transporter over the liquid surface powered by UV or NIR light; however, only the NIR light-driven transporter is shown (**Figure 5.6a and b**). To avoid the shadow formed by the aluminum cargo, the polymer film was illuminated from below. The aluminum cargo was deposited at the surface of the composite films when the latter had reached the isopropanol surface and was ‘surfing’ under illumination at a controllable and constant speed of approximately 1.2 mm s⁻¹. The distorted lines of the LED’s lens and background during NIR light irradiation in the photographs are attributed to the refractive index gradient induced by the temperature gradient, further indicating the presence of the temperature gradient upon illumination (**Figure 5.6c**).

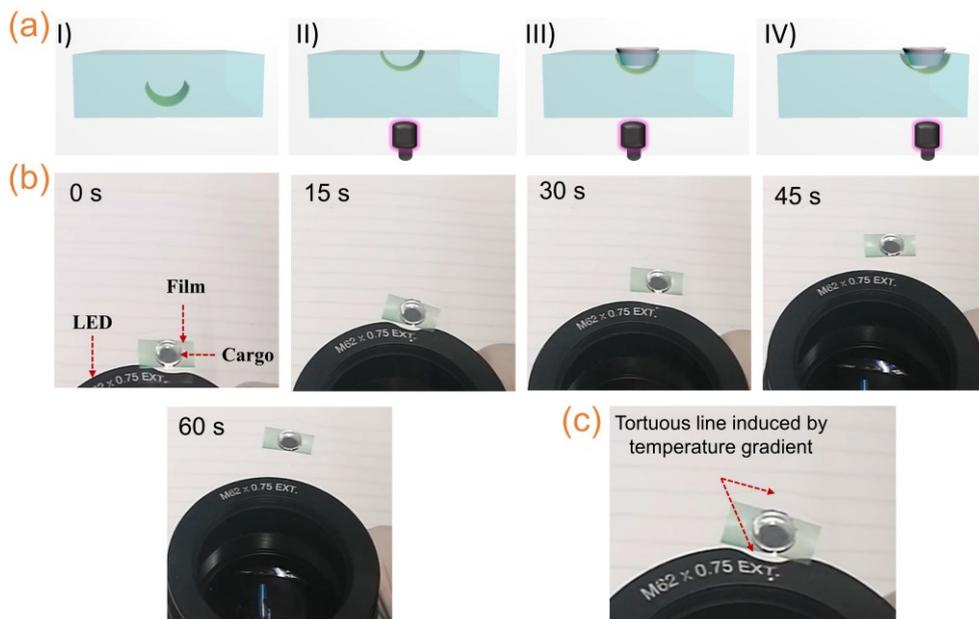


Figure 5.6 a) Schematic visualization of photo-fueled transport (I-II-III-IV: beginning-lifting-loading-transporting). b) Photo-fueled cargo transport on the surface of isopropanol (top view). An aluminum pan was put on PE-BZT-GN-QR film. c) Refractive index gradient induced by temperature gradient under NIR irradiation. Here, the intensities of NIR (780 nm) light are approximately 90 mW cm^{-2} .

5.3 Conclusions

We have reported free-standing 3D anisotropic, single-layer commodity polymer composite films based on polyethylene doped with photothermal additives produced with solution-casting and stretching. A facile and versatile method is demonstrated for producing photothermal responsive actuators with multiple actuation and surfing modes. The shape deformation can be controlled by light exposure with fast responses and short recovery times and remarkable shape morphing capabilities in air. Furthermore, remotely controllable ascending/descending and ‘surfing’ in liquid were achieved by a photo-induced thermal Marangoni effect, and a gripper capable of picking up cargo was also demonstrated. These composite commodity films have comparable responsive properties to 3D programmed anisotropic polymer based on specialty polymers such as liquid crystals and hydrogels reported earlier. Our results open up new possibilities for using commodity polymers in a broad range of applications such as light-responsive soft actuators and soft robotics.

5.4 Experimental Section

Materials. Ultra-high molecular weight polyethylene, UHMWPE ($M_w \sim 4 \times 10^6$ Da. with dispersity (\mathcal{D}) ~ 7), was received from DSM (Geleen, The Netherlands). UV absorber dye (BZT, also Tinuvin[®] 328), antioxidant pentaerythritol tetrakis(3-(3,5-di-tert-butyl-4-hydroxyphenyl)propionate) (Irganox[®] 1010), and quaterrylene bisimide-based NIR dye (Lumogen[®] IR 788) were received from BASF (Ludwigshafen, Germany). GN (specific surface area ~ 750 m² g⁻¹), paraffin oil, and sodium dodecylbenzene sulfonate (SDBS) were purchased from Sigma-Aldrich. Xylene was purchased from Biosolve B.V. Cellulose microfibers are recovered from a piece of scrap A4 paper. All reagents were used as received, without further purification.

Fabrication. BZT (2 wt% to UHMWPE), Irganox[®] 1010 (0.1 wt% to UHMWPE), GN (0.1 wt% to UHMWPE) and NIR dye (3 wt% to UHMWPE) were added to xylene (200 mL) with ultra-sonication for 1 h. Then, UHMWPE powder (2 g) was added to the mixture with degassing via ultra-sonication for 30 minutes. The mixture was stirred at approximately 125 °C in an oil bath until the Weissenberg effect was observed.^[45] Afterward, the solution was left in the oil bath for 1 h to dissolve UHMWPE completely, and then the solution was cast into an aluminum tray. During drying at room temperature, the cast films were fixed to avoid significant contraction. Finally, the dry films were cut into small strips and stretched manually at approximately 120 °C.

Analytical Techniques. UV-vis spectra of samples were measured from 300 to 1100 nm using a Shimadzu UV-3102 PC spectrophotometer (The distance between the samples and the light detector is approximately 85 cm). Before the measurement, the drawn films were coated with one drop of paraffin oil to reduce the surface light scattering and then sandwiched by two quartz glass slides. Raman scattering spectroscopy was performed on a Raman microscope (Witec Alpha 300 R). UV and NIR light were provided by LEDs from Thorlabs (M365L2 and M780L3) using a Thorlabs 4D100 controller.

Chapter 5

5.5 References

- [1] R. C. P. Verpaalen, T. Engels, A. P. H. J. Schenning, M. G. Debije, *ACS Appl Mater Interfaces* **2020**, *35*, 38829.
- [2] D. Rus, M. T. Tolley, *Nature* **2015**, *521*, 467.
- [3] Y. Cheng, H. Lu, X. Lee, H. Zeng, A. Priimagi, *Adv Mater* **2019**, *32*, 1906233.
- [4] M. Pilz da Cunha, M. G. Debije, A. P. H. J. Schenning, *Chem Soc Rev* **2020**, *49*, 6568.
- [5] L. Liu, M. del Pozo, F. Mohseninejad, M. G. Debije, D. J. Broer, A. P. H. J. Schenning, *Adv Opt Mater* **2020**, *8*, 2000732.
- [6] Y. Gao, B. Han, W. Zhao, Z. Ma, Y. Yu, H. Sun, *Front Chem* **2019**, *7*, 506.
- [7] L. Lu, J. Liu, Y. Hu, Y. Zhang, H. Randriamahazaka, W. Chen, *Adv Mater* **2012**, *24*, 4317.
- [8] L. Lu, J. Liu, Y. Hu, Y. Zhang, W. Chen, *Adv Mater* **2013**, *25*, 1270.
- [9] H. Kim, H. Lee, I. Ha, J. Jung, P. Won, H. Cho, J. Yeo, S. Hong, S. Han, J. Kwon, K. J. Cho, S. H. Ko, *Adv Funct Mater* **2018**, *28*, 1801847.
- [10] M. Amjadi, M. Sitti, *Adv Sci* **2018**, *5*, 1800239.
- [11] Y. S. Kim, M. Liu, Y. Ishida, Y. Ebina, M. Osada, T. Sasaki, T. Hikima, M. Takata, T. Aida, *Nat Mater* **2015**, *14*, 1002.
- [12] X. Yu, R. Rajamani, K. A. Stelson, T. Cui, *Sensors Actuators, A Phys* **2006**, *132*, 626.
- [13] W. Jiang, D. Niu, H. Liu, C. Wang, T. Zhao, L. Yin, Y. Shi, B. Chen, Y. Ding, B. Lu, *Adv Funct Mater* **2014**, *24*, 7598.
- [14] Q. Li, A. P. H. J. Schenning, T. J. Bunning, *Adv Opt Mater* **2019**, *7*, 1901160.
- [15] F. Ge, R. Yang, X. Tong, F. Camerel, Y. Zhao, *Angew Chem Int Ed* **2018**, *57*, 11758.
- [16] Z. Sun, Y. Yamauchi, F. Araoka, Y. S. Kim, J. Bergueiro, Y. Ishida, Y. Ebina, T. Sasaki, T. Hikima, T. Aida, *Angew Chem Int Ed* **2018**, *57*, 15772.
- [17] R. C. P. Verpaalen, M. Pilz da Cunha, T. A. P. Engels, M. G. Debije, A. P. H. J. Schenning, *Angew Chem Int Ed* **2020**, *59*, 4532.
- [18] R. C. P. Verpaalen, M. G. Debije, C. W. M. Bastiaansen, H. Halilović, T. A. P. Engels, A. P. H. J. Schenning, *J Mater Chem A* **2018**, *6*, 17724.
- [19] S. Ma, X. Li, S. Huang, J. Hu, H. Yu, *Angew Chem Int Ed* **2019**, *58*, 2655.
- [20] D. Okawa, S. J. Pastine, A. Zettl, J. M. J. Fre, *J Am Chem Soc* **2009**, *131*, 5396.
- [21] H. K. Bisoyi, Q. Li, *Chem Rev* **2016**, *116*, 15089.
- [22] A. Pal, D. Goswami, R. V. Martinez, *Adv Funct Mater* **2019**, *30*, 1906603.
- [23] M. Chen, B. Yao, M. Kappl, S. Liu, J. Yuan, R. Berger, *Adv Funct Mater* **2020**, *30*, 1906752.
- [24] J. A. H. P. Sol, A. R. Peeketi, N. Vyas, A. P. H. J. Schenning, R. K. Annabattula, M. G. Debije, *Chem Commun* **2019**, *55*, 1726.
- [25] Z. Jiang, B. Diggle, L. A. Connal, *Adv Mater* **2019**, *31*, 1904956.
- [26] H. Qin, T. Zhang, N. Li, H. Cong, S. Yu, *Nat Commun* **2019**, *10*, 1.
- [27] M. Camacho-lopez, H. Finkelman, P. Palfy-muhoray, M. Shelley, *Nat Mater* **2004**, *3*, 307.
- [28] Z. Cheng, T. Wang, X. Li, Y. Zhang, H. Yu, *ACS Appl Mater Interfaces* **2015**, *7*, 27494.
- [29] L. Li, J. Meng, C. Hou, Q. Zhang, Y. Li, W. Yu, Hao Hongzhi, *ACS Appl Mater Interfaces* **2018**, *10*, 15122.
- [30] X. Zhan, J. Zheng, Y. Zhao, B. Zhu, R. Cheng, J. Wang, J. Liu, J. Tang, J. Tang, *Adv Mater* **2019**, *31*, 72

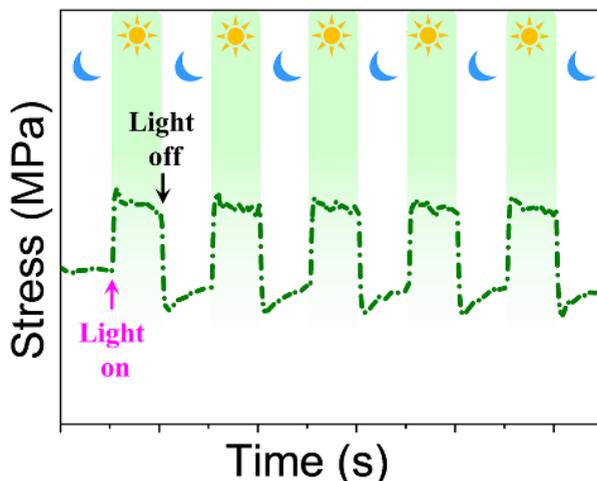
Three-dimensional anisotropic polyethylene as light-responsive grippers and surfing divers

1903329.

- [31] W. Wang, Y. Liu, Y. Liu, B. Han, H. Wang, D. Han, J. Wang, Y. Zhang, H. Sun, *Adv Funct Mater* **2017**, *27*, 1702946.
- [32] M. Yang, Z. Yuan, J. Liu, Z. Fang, L. Fang, D. Yu, *Adv Opt Mater* **2019**, *7*, 1900069.
- [33] M. Pilz da Cunha, E. A. J. Van Thoor, M. G. Debije, D. J. Broer, A. P. H. J. Schenning, *J Mater Chem C* **2019**, *7*, 13502.
- [34] G. J. Fang, J. E. MacLennan, Y. Yi, M. A. Glaser, M. Farrow, E. Korblova, D. M. Walba, T. E. Furtak, N. A. Clark, *Nat Commun* **2013**, *4*, 1521.
- [35] M. R. A. Bhatti, E. Bilotti, H. Zhang, S. Varghese, R. C. P. Verpaalen, A. P. H. J. Schenning, C. W. M. Bastiaansen, T. Peijs, *ACS Appl Mater Interfaces* **2020**, *12*, 33210.
- [36] R. C. P. Verpaalen, S. Varghese, A. Froyen, M. Pilz da Cunha, M. J. Pouderoijen, J. R. Severn, M. R. Bhatti, T. Peijs, C. W. M. Bastiaansen, M. G. Debije, T. A. P. Engels, A. P. H. J. Schenning, *Matter* **2020**, *2*, 1522.
- [37] M. R. A. Bhatti, E. Bilotti, H. Zhang, C. W. M. Bastiaansen, T. Peijs, *Polymer* **2020**, *207*, 122897.
- [38] L. T. de Haan, V. Gimenez-Pinto, A. Konya, T. S. Nguyen, J. M. N. Verjans, C. Sánchez-Somolinos, J. V. Selinger, R. L. B. Selinger, D. J. Broer, A. P. H. J. Schenning, *Adv Funct Mater* **2014**, *24*, 1251.
- [39] L. T. de Haan, C. Sánchez-Somolinos, C. M. W. Bastiaansen, A. P. H. J. Schenning, D. J. Broer, *Angew Chemie* **2012**, *124*, 12637.
- [40] N. U. Zhanpeisov, S. Nishio, H. Fukumura, *Int J Quantum Chem* **2005**, *105*, 368.
- [41] G. K. White, C. L. Choy, *J Polym Sci Polym Phys Ed* **1984**, *22*, 835.
- [42] P. A. Irvine, P. Smith, *Macromolecules* **1986**, *19*, 240.
- [43] R. Huang, X. Xu, S. Lee, Y. Zhang, B. Kim, *Materials* **2013**, *6*, 4122.
- [44] M. Pöllänen, M. Suvanto, T. T. Pakkanen, *Compos Sci Technol* **2013**, *76*, 21.
- [45] K. Weissenberg, *Nature* **1947**, *157*, 310.

Chapter 6

NIR-Vis-UV Light-Responsive High Stress-Generating Polymer Actuators with a Reduced Creep Rate



Abstract Untethered, light-responsive, high-stress-generating actuators based on widely-used commercial polymers are appealing for applications in soft robotics. However, the construction of actuators that are stable and reversibly responsive to low-intensity ultraviolet, visible and infrared lights remains challenging. Here, transparent, stress-generating actuators are reported based on ultra-drawn, ultra-high molecular weight polyethylene films. The composite films have different draw ratios (30, 70 and 100) and contain a small amount of graphene in combination with ultraviolet and near-infrared-absorbing dyes. The composite actuators respond rapidly ($t_{0.9} < 0.8$ s) to different wavelengths of light (i.e. 780 nm, 455 nm, and 365 nm). A maximum photo-induced stress of 35 MPa was achieved at a draw ratio of 70 under near-infrared light irradiation. The photo-induced stress increases linearly with the light intensity, indicating the transfer of light into thermally induced mechanical contraction. Moreover, the addition of additives led to a reduction in the plastic creep rate of the drawn films compared to their non-modified counterparts.

This chapter is largely reproduced from:

Pan, X., Verpaalen, R. C. P., Zhang, H., Debije, M. G., Engels, T. A. P., Bastiaansen, C. W. M. & Schenning, A. P. H. J. NIR-Vis-UV Light-Responsive High Stress-Generating Polymer Actuators with a Reduced Creep Rate *Macromolecular Rapid Communications*, 2021, 42, 2100157.

6.1 Introduction

Reversible stress changes play important roles in energy conversion devices and living organisms, including in piezoelectric devices, wings of birds, and the heartbeats of animals.^[1-3] Various stress-generating actuators have been fabricated using responsive materials, such as hydrogels, shape memory alloys and liquid crystalline polymers, which are driven by various external stimuli including light.^[4-11] These stress-generating actuators exhibit potential in soft robot applications.^[12,13] Light-driven actuators have attracted considerable attention owing to their reversible response and wireless operation with high spatial/temporal control.^[14-18] However, most of these actuators are driven by ultra-violet light (UV) which often causes degradation of the polymers or harm to their environment.^[19-25] Near-infrared and visible lights have lower photon energies, and consequently are less damaging.^[3] To make use of these wavelengths, carbon nanotubes and graphene are appealing, enabling the conversion of visible and NIR lights into heat.^[26]

Commodity polymers, like polyethylenes and polypropylene, are produced worldwide on huge scales, and provide robust mechanical properties at relatively low costs, and hold potential for the development of actuators on a similarly large scale.^[27] Currently, commodity polymers are often combined with hydrogels or liquid crystals to fabricate bilayer actuators. However, it would be more attractive from a processing point of view to directly dope commodity polymers with stimuli-responsive additives to create robust, single-layer stimuli-responsive soft actuators. Recently, ultra-drawn, ultra-high molecular weight polyethylene (UHMWPE) films^[28] containing light-responsive azobenzene dyes with long aliphatic tails were reported.^[29,30] It was shown that fast responding (< 1 second) photo-actuators with maximal actuation stresses up to 60 MPa can be produced at low strain (< 0.1 %).^[29-31] Moreover, it was shown that photo-actuators containing UV stabilizers such as 2-(2H-benzotriazol-2-yl)-4,6-ditertpentylphenol (BZT) have a similar performance.³¹ The operating mechanism of these UV light-responsive actuators is the photo-thermal effect in combination with a negative thermal expansion coefficient of the oriented and chain extended polymer.^[29-31] However, there is continuous and rapid stress decay in these stress-generating actuators due to the innate stress relaxation.

Ultra-drawn UHMWPE fibers and films exhibit irreversible creep deformation at static loading conditions and exhibit stress relaxation at a fixed strain, especially at prolonged time scales and at elevated temperatures.^[32-34] This response is induced by the combined reversible visco-elastic and irreversible visco-plastic deformations over time,^[35] which is difficult to reduce in polyethylene-based systems and limits their performance. Consequently, developing robust high stress-generating commodity polymer actuators that can be addressed with near-infrared (NIR) and/or visible lights remains challenging.

Highly oriented UHMWPE composite actuators containing graphene, BZT, and NIR dye additives cut from stretched film perpendicular to the stretching direction were reported.^[36]

These NIR and/or UV light light-responsive actuators can exhibit bending actuation and be deployed as a gripper in the air (see **Chapter 5**).^[36]

6.2 Results and Discussion

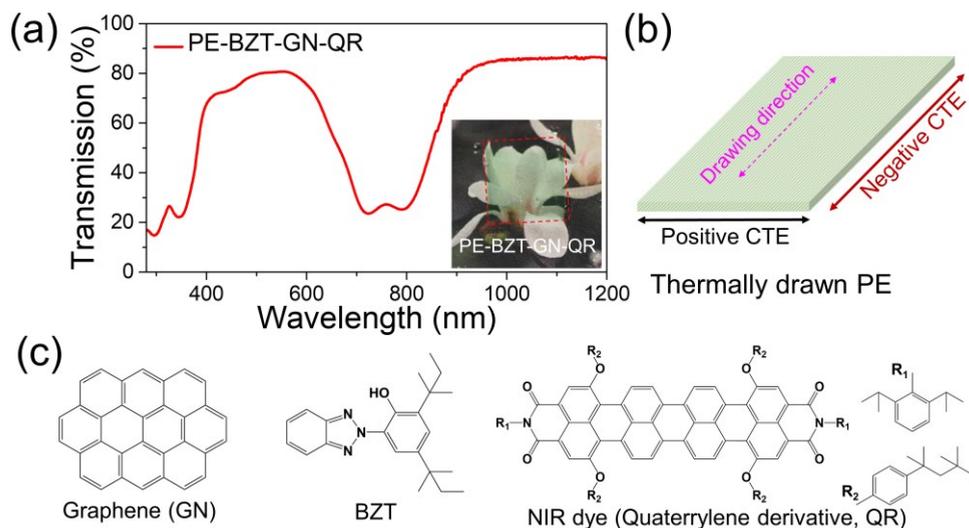


Figure 6.1 (a) Transmission spectra of PE-BZT-GN-QR films with a draw ratio of 30 sandwiched between two quartz glass slides. The inset is a photograph of the PE-BZT-GN-QR film sandwiched between two quartz glass slides. (b) Definitions for the coefficients of positive and negative thermal expansion (CTE) of ultra-drawn PE films. (c) Chemical structures of graphene (GN), BZT, and NIR dyes (QR).

To prepare the NIR-Vis-UV responsive actuators, PE composite (PE-BZT-GN-QR) films were fabricated via solution-casting and subsequent solid-state film drawing following our protocol reported earlier (**Chapter 5**).^[36] In the composite films, three light-responsive additives were used: (2-(2H-benzotriazol-2-yl)-4,6-ditertpentylphenol, BZT) to absorb UV light and improve the visible light transmission of ultra-drawn films (**Figure 6.1a**);^[28] graphene as a NIR-Vis-UV light-absorbing additive to improve the thermal conductivity of the actuator;^[37] a dye to absorb NIR (650-850 nm), visible (400-480 nm), and UV (<400 nm) light simultaneously (**Figure 6.1c**).^[38] Photographs taken from the PE composite films demonstrate optical transmission is retained after adding BZT and graphene (**Figure 6.1a**). It should be noted that ultra-drawn PE films exhibit anisotropic coefficients of thermal expansion (CTE) (**Figure 6.1b**), with a large, draw ratio-dependent negative CTE parallel to the drawing direction.^[39] Thus, ultra-drawn drawn UHMWPE composite films contract along the drawing direction when heated by absorption of light.

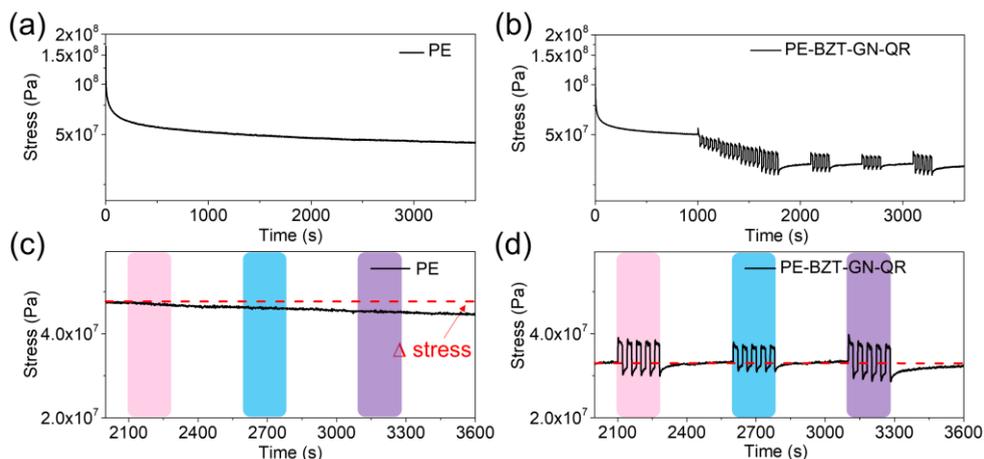


Figure 6.2 Stress relaxation curve of (a) pristine, ultra-drawn UHMWPE films and (b) ultra-drawn UHMWPE (PE-BZT-GN-QR) films with graphene, UV, and NIR dyes with draw ratios of 30 upon pulsed illumination. (c and d) Magnification of the stress relaxation curves in the time interval between 2000 and 3500 seconds. The pink, blue, and violet regions represent NIR, visible, and UV light irradiation, respectively. The horizontal red dashed line represents the stress at ~ 2050 s, which is used to obtain the stress decay (Δ stress) over time.

The stress-generation curves of ultra-drawn PE and PE-BZT-GN-QR films are shown in **Figures 6.2a** and **6.2b**. The stress of pristine PE films decreases during the measurement with and without light illumination (**Figure 6.2a** and **6.2c**). This continuous, gradual decay of stress is caused by the inherent time-dependent stress relaxation of these highly oriented PE systems.^[35] In **Figure 6.2b**, PE-BZT-GN-QR films exhibit similar stress relaxation as the pristine PE film during the first 1000 s. However, upon periodic NIR illumination from 1000 s to 1800 s the stress decreased. This overall decrease during the NIR illumination is caused by temperature-induced chain mobility, in which both the reversible visco-elastic and irreversible visco-plastic contributions are accelerated by the temperature increase.^[30] Having almost reached a plateau, the PE-BZT-GN-QR films showed fast ($t_{0.9} < 0.8$ s) and repeatable actuation stress upon fluctuating exposures to NIR, blue, and UV lights (**Figure 6.2b** and **6.2d**). There is no obvious stress decay (Δ stress ~ 0 MPa) of PE-BZT-GN-QR films either during or between light exposures from 2050 s to 3600 s (**Figure 6.2d**) while there is a continuous stress decay (Δ stress ~ 2.2 MPa) in pure PE film (**Figure 6.2c**) regardless of illumination conditions. This indicates a reduced stress relaxation in the PE-BZT-GN-QR film, and the relaxation in PE-BZT-GN-QR films will be explored in some more detail later in comparison to the pure PE films.

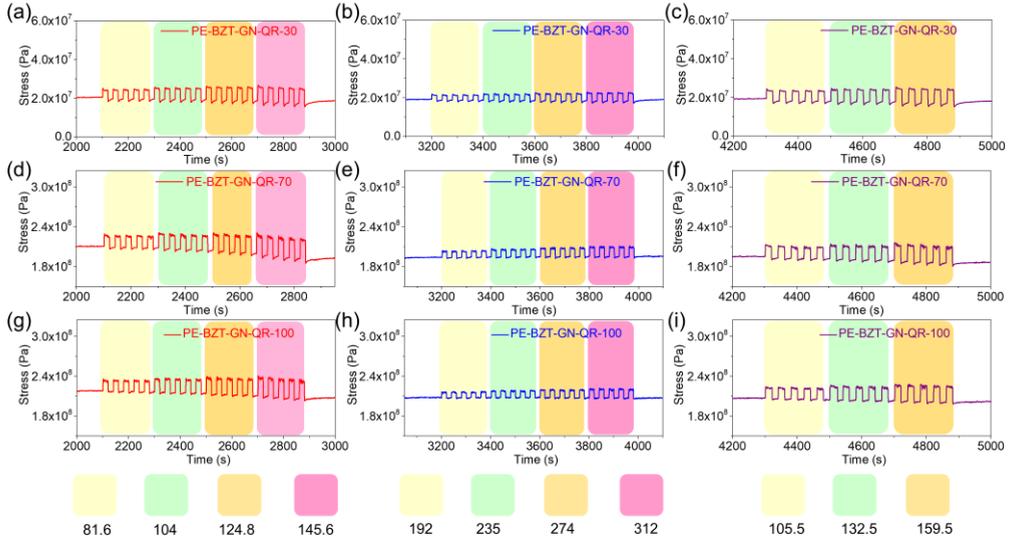


Figure 6.3 Photo-induced stresses of PE-BZT-GN-QR composite films with different draw ratios (30, 70, and 100) under different incident light intensity irradiation as a function of the testing time after NIR illumination (1000-1800 s). The red, blue, and purple curves represent the photo-induced stress under NIR (780 nm), blue (455 nm), and UV (365 nm) irradiations. The regions with different colors represent the incident light intensity which is shown below curves and its unit is mW/cm^2 .

The effects of light intensity and draw ratio on the actuation stresses of the PE-BZT-GN-QR composite films were characterized at different wavelengths and light intensities over more than 5000 s (**Figure 6.3**). These results reveal that PE-BZT-GN-QR films with a draw ratio of 30 exhibit fast ($t_{0.9} < 0.8$ s) and reversible actuation stress change under NIR, blue, and UV light irradiation, and that the actuation stress increases with the light intensity (**Figure 6.3a-c**). The actuation stress under NIR and UV light irradiation is greater than that under blue light due to the greater light absorption of NIR and UV light (**Figure 6.1a**). The maximum actuation stress of PE-BZT-GN-QR with a draw ratio of 30 under NIR irradiation is about 10 MPa. When increasing the draw ratio, the photo-induced actuation stress reaches a maximum (35-40 MPa) at a draw ratio of 70 and then decreases to 30 MPa at a draw ratio of 100 (Figure 3 and Figure 4). The increase in photo-induced stress at draw ratios between 30 and 70 could be attributed to an increasing CTE of PE-BZT-GN-QR films (**Figure 6.4**),^[41] although the thickness of films decreased with the draw ratios. The subsequent decrease in actuation stress at draw ratios between 70 and 100 could originate from the decreasing absorbed energy caused by the decreasing thickness of films at higher draw ratios. Interestingly, the photo-induced stress maintains a fast and reversible response with reduced relaxation relative to the pristine PE system, within the testing light intensity range after pre-illumination (NIR illumination between 1000-1800 s).

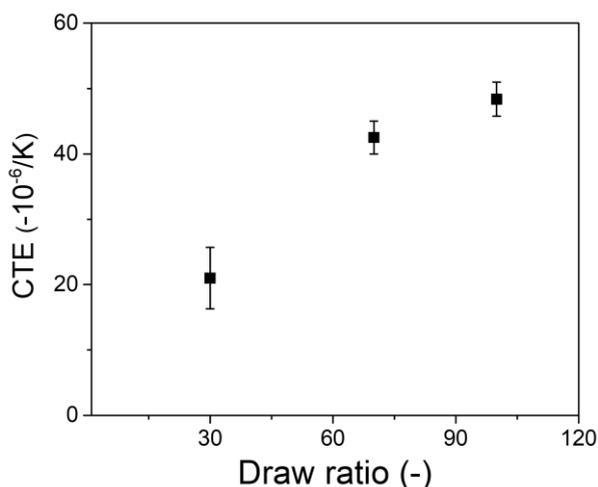


Figure 6.4 Coefficients of thermal expansion of PE-BZT-GN-QR films as a function of draw ratio.

To elucidate the relationship between the photo-induced stress and light intensity, the absorbed energy of the PE-BZT-GN-QR film with a draw ratio of 30 was calculated (**Figure 6.5**).^[30] The results reveal that photo-induced actuation stresses increase linearly with the absorbed energy at all wavelengths, indicating that the films generate photo-induced stresses originating from the negative CTE of ultra-drawn UHMWPE. The difference in slopes of actuation stress versus absorbed energy for the different wavelengths indicates a small difference in the light conversion efficiency of the additives. It was observed that surface melting took place when employing high-intensity UV irradiation, supporting the photon-to-heat conversion hypothesis.^[42,43]

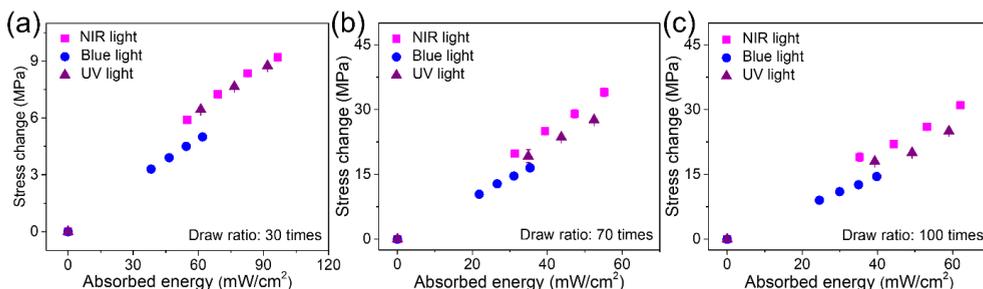


Figure 6.5 (a-c) Photo-induced actuation stress of PE-BZT-GN-QR with draw ratios of 30, 70 and 100 as a function of absorbed energy at different wavelengths. The five dots correspond to the different incident light intensities.

NIR-Vis-UV light-responsive high stress-generating polymer actuators

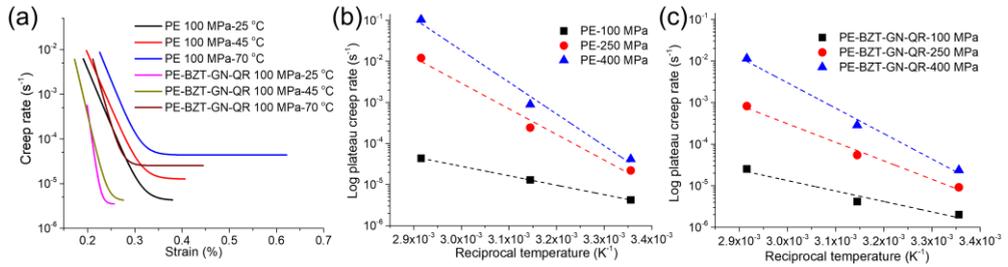


Figure 6.6 (a) Sherby-Dorn plots (log creep rate vs strain) of PE and PE-BZT-GN-QR films with a draw ratio of 70 at different temperatures. (b) Logarithmic plateau creep rate of PE films as a function of reciprocal temperature ($1/T$). (c) Logarithmic plateau creep rate of PE-BZT-GN-QR films as a function of reciprocal temperature ($1/T$) and the unit of the reciprocal temperature is K^{-1} .

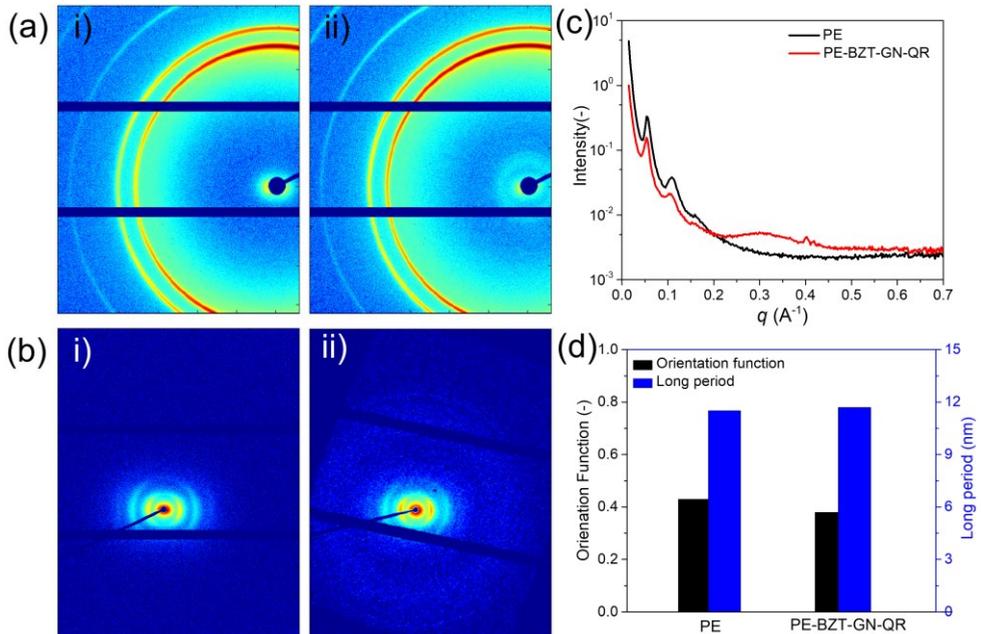


Figure 6.7 (a) Wide-angle X-ray scattering (WAXS) and (b) Small-angle X-ray scattering (SAXS) of the PE undrawn film (i) and PE-BZT-GN-QR undrawn composite film (ii) with a fixed angle of 45 degrees with respect to the incident beam. (c) Intensity of SAXS signal as a function of scattering vector (q) of the PE and PE-BZT-GN-QR undrawn composite films. (d) Herman's orientation function and the long period of PE and PE-BZT-GN-QR undrawn composite films. Here, the undrawn films are fixed with a fixed angle of 45 degrees. There is a small difference in Herman's orientation function and no obvious difference in the long period between PE and PE-BZT-GN-QR undrawn composite films.

To illustrate the mechanism of the fast and reversible stress change with a reduced creep rate in PE-BZT-GN-QR films, the creep deformation was characterized at different stresses and temperatures (**Figure 6.6**). Sherby-Dorn plots characterize the creep rates of PE and PE-BZT-GN-QR films (**Figure 6.6a**). It was observed that PE-BZT-GN-QR films exhibit lower plateau creep rates ($\dot{\epsilon}_p$) than neat PE films at comparable draw ratios at the same stresses and temperatures. This behavior confirms the reduced relaxation observed during the light actuating measurements. X-ray measurements reveal that there is no obvious difference in the initial ordering of the crystal morphology (as evidenced by the long period derived from SAXS) and only a slight difference in orientation (as evidenced by Herman's orientation function) of undrawn PE and PE-BZT-GN-QR films (**Figure 6.7**). It is known that crystals assume preferential orientations with respect to the thickness of the film upon solution-casting of UHMWPE films.^[44] This results in the c-axis of the crystal orienting perpendicular to the subsequent drawing direction and can be described as a negative pre-orientation of the chains. Drawing of UHMWPE is known to be an affine deformation process,^[45] and hence the larger negative pre-orientation of the as-cast PE films may explain the difference in post-draw moduli. We cannot conclusively define the origin of the observed difference in mechanical responses but do not pursue it further as it is outside the scope of the current investigation. Based on these observations, it can be concluded that the light-responsive UHMWPE actuators are performing mechanically as well as, or even better than, their neat counterparts.

The stress-generating actuators based on PE-BZT-GN-QR films are compared with other actuators using the specific actuation stress, defined as the actuation stress divided by the material density.^[2,11,29,46-49] The multi-wavelength responsive actuators in this work exhibit almost 100 times higher specific actuation stresses than natural muscle, and also outperform dielectric elastomers, liquid crystalline actuators and piezo polymers.

6.3 Conclusions

Highly transparent, stress-generating actuators were fabricated using solution-casting and solid-state drawing of UHMWPE films containing graphene and both UV and NIR absorbing dyes. The resulting stress-generating actuators are fast (< 0.8 s) and can be repeatedly and reversibly driven with NIR, blue and UV lights. The maximum specific actuation stress (35-40 MPa) was achieved at a draw ratio of 70. The stable photo-induced stress with reduced stress relaxation was obtained due to the reduced chain slip in the plastic region of ultra-drawn composite films. This makes the composite films based on widely used polyethylene attractive as robust light-driven high stress generating actuators for a manifold of applications.

6.4 Experimental Section

Materials. UHMWPE with a $M_w \sim 4 \times 10^6$ Da. was provided by DSM (Geleen, The Netherlands). 2-(2H-benzotriazol-2-yl)-4,6-ditertpentylphenol (BZT), quaterrylene bisimide based derivative (NIR dye), and an antioxidant (Irganox 1010) were purchased from BASF (Germany). Graphene nanoplates (size $< 2 \mu\text{m}$, specific surface area $\sim 750 \text{ m}^2/\text{g}$) were purchased from Sigma-Aldrich. Paraffin oil and xylene were obtained from Thermo Fisher Scientific Incorporated and Biosolve BV (The Netherlands), respectively. All reagents were used as received (see also **Chapter 5**).

Fabrication. BZT (2 wt% to UHMWPE), the antioxidant Irganox 1010 (0.1 wt% to UHMWPE), GN (0.1 wt% to UHMWPE), and the NIR dye (3 wt% to UHMWPE) were added to xylene (200 mL) and ultra-sonication was used for 1 hour to disperse the graphene. UHMWPE powder (2 g) was added to the suspension and degassing performed using ultra-sonication for 30 minutes. The suspension was transferred to a silicon oil bath ($\sim 125 \text{ }^\circ\text{C}$) and stirred until the Weissenberg effect was observed. The solution was left at an elevated temperature for 1 h to dissolve UHMWPE completely, and the solution was then cast into aluminum trays. The cast films were fixed to avoid excessive shrinkage during drying. After drying for several days in a fume hood at room temperature films were cut into small strips. Ultra-drawing of the dried films was performed at $120 \text{ }^\circ\text{C}$ to different draw ratios (30, 70, and 100) (see also **Chapter 5**).

Analytical Techniques. The (polarized) transmission spectra of films were measured on a UV-3102 PC spectrophotometer in the wavelength range of 300 to 1200 nm at a film-detector distance of about 85 cm with and without a linear polarizer. The films were coated with paraffin oil to reduce the surface light scattering and sandwiched between two quartz glass slides. The stress relaxation was measured on a dynamic mechanical analysis device (DMA 850, TA Instruments) at a pre-strain of 1%. The stress relaxation was measured for at least 1800 seconds. The samples were illuminated with LEDs at different wavelengths in the UV (365 nm), VIS (455 nm), and NIR (780 nm). First, the ultra-drawn samples were pre-illuminated with LED light pulses with a duration of 20 s and an off-time of 20 s from 1000-1800 s. Subsequently, a second pulsed LED illumination procedure was used for 20 s with an off-time of 20 s. The response time ($t_{0.9}$) was defined as the time the signal takes to reach 90% of the maximum actuation stress. The LEDs were provided by THORLABS (M365L2, M455L4, and M780L3) and the distance between LEDs and samples was about 10 cm. The creep of ultra-drawn samples as a function of time was measured at different stresses and temperatures on a DMA 850 (TA Instruments). In this particular case, the LED light was switched off and the creep was measured in the dark. Sherby-Dorn plots^[50] (creep rate versus creep strain) were constructed and an exponential decay function fit describing the strain changes over time was used to smoothen the curve. The coefficient of thermal expansion was measured under iso-stress modes with a constant heating rate ($3 \text{ }^\circ\text{C}/\text{min}$) from 0 to $60 \text{ }^\circ\text{C}$. The thermal conductivity was characterized using the Angstrom method as previously

Chapter 6

reported.^[28,40] The absorbed energy was calculated by the integration of absorption spectra and the LED's spectra. The LED's spectra were characterized by a Labsphere SLMS 1050 integrating sphere connected to an International Light RPS900 diode array detector. The temperature of the samples was measured using an IR camera (Fluke).

6.5 References

- [1] S. R. Anton, H. A. Sodano, *Smart Mater Struct* **2007**, *16*, R1.
- [2] J. Rödel, W. Jo, K. T. P. Seifert, E. M. Anton, T. Granzow, D. Damjanovic, *J Am Ceram Soc* **2009**, *92*, 1153.
- [3] R. Lan, J. Sun, C. Shen, R. Huang, Z. Zhang, L. Zhang, *Adv Mater* **2020**, *32*, 1906319.
- [4] L. Yang, L. Chang, Y. Hu, M. Huang, Q. Ji, P. Lu, J. Liu, W. Chen, Y. Wu, *Adv Funct Mater* **2020**, *30*, 1908842.
- [5] H. Kim, J. A. Lee, C. P. Ambulo, H. B. Lee, S. H. Kim, V. V Naik, C. S. Haines, A. E. Aliev, R. Ovalle-robles, R. H. Baughman, T. H. Ware, *Adv Funct Mater* **2019**, *29*, 1905063.
- [6] H. Qin, T. Zhang, N. Li, H. Cong, S. Yu, *Nat Commun* **2019**, *10*, 1.
- [7] Z. Jiang, B. Diggie, L. A. Connal, *Adv Mater* **2019**, *31*, 1904956.
- [8] A. Pal, D. Goswami, R. V. Martinez, *Adv Funct Mater* **2019**, *30*, 1906603.
- [9] J. Lee, M. Wei, M. Tan, K. Parida, G. Thangavel, S. A. Park, T. Park, P. S. Lee, *Adv Mater* **2020**, *32*, 1906679.
- [10] A. Miriyev, K. Stack, H. Lipson, *Nat Commun* **2017**, *8*, 1.
- [11] H. Banerjee, M. Suhail, H. Ren, *Biomimetics* **2018**, *3*, 15.
- [12] Y. Gao, L. Casalena, M. L. Bowers, R. D. Noebe, M. J. Mills, Y. Wang, *Acta Mater* **2017**, *126*, 389.
- [13] P. Chowdhury, H. Schitoglu, *Prog Mater Sci* **2017**, *88*, 49.
- [14] W. Jiang, D. Niu, H. Liu, C. Wang, T. Zhao, L. Yin, Y. Shi, B. Chen, Y. Ding, B. Lu, *Adv Funct Mater* **2014**, *24*, 7598.
- [15] M. Pilz da Cunha, S. Ambergen, M. G. Debije, E. F. G. A. Homburg, J. M. J. den Toonder, A. P. H. J. Schenning, *Adv Sci* **2020**, *7*, 1902842.
- [16] M. Pilz da Cunha, A. R. Peeketi, K. Mehta, D. J. Broer, R. K. Annabattula, A. P. H. J. Schenning, M. G. Debije, *Chem Commun* **2019**, *55*, 11029.
- [17] M. Pilz da Cunha, E. A. J. van Thoor, M. G. Debije, D. J. Broer, A. P. H. J. Schenning, *J Mater Chem C* **2019**, *7*, 13502.
- [18] A. H. Gelebart, G. Vantomme, E. W. Meijer, D. J. Broer, *Adv Mater* **2017**, *29*, 1606712.
- [19] D. Karentz, L. H. Lutze, *Limnol Oceanogr* **1990**, *35*, 549.
- [20] E. Slaninova, P. Sedlacek, F. Mravec, L. Mullerova, O. Samek, M. Koller, O. Hesko, D. Kucera, I. Marova, S. Obruca, *Appl Microbiol Biotechnol* **2018**, *102*, 1923.
- [21] N. Nagai, T. Matsunobe, T. Imai, *Polym Degrad Stab* **2005**, *88*, 224.
- [22] G. A. Garinis, J. R. Mitchell, M. J. Moorhouse, K. Hanada, H. De Waard, D. Vandeputte, J. Jans, K. Brand, M. Smid, P. J. Van Der Spek, J. H. J. Hoeijmakers, R. Kanaar, G. T. J. Van Der Horst, *EMBO J* **2005**, *24*, 3952.
- [23] Y. Matsumura, H. N. Ananthaswamy, *Toxicol Appl Pharmacol* **2004**, *195*, 298.
- [24] K. Kumar, A. P. H. J. Schenning, D. J. Broer, D. Liu, *Soft Matter* **2016**, *12*, 3196.
- [25] B. Rånby, *J Anal Appl Pyrolysis* **1989**, *15*, 237.
- [26] Z. Cheng, T. Wang, X. Li, Y. Zhang, H. Yu, *ACS Appl Mater Interfaces* **2015**, *7*, 27494.
- [27] R. C. P. Verpaalen, T. Engels, A. P. H. J. Schenning, M. G. Debije, *ACS Appl Mater Interfaces* **2020**, *35*, 38829.
- [28] X. Pan, L. Shen, A. P. H. J. Schenning, C. W. M. Bastiaansen, *Adv Mater* **2019**, *31*, 1904348.

Chapter 6

- [29] S. Varghese, S. Fredrich, G. Vantomme, S. R. Prabhu, J. Teyssandier, S. De Feyter, J. Severn, C. W. M. Bastiaansen, A. P. H. J. Schenning, *J Mater Chem C* **2020**, *8*, 694.
- [30] R. C. P. Verpaalen, S. Varghese, A. Froyen, M. Pilz da Cunha, M. J. Pouderoijen, J. R. Severn, M. R. Bhatti, T. Peijs, C. W. M. Bastiaansen, M. G. Debije, T. A. P. Engels, A. P. H. J. Schenning, *Matter* **2020**, *2*, 1522.
- [31] M. R. A. Bhatti, E. Bilotti, H. Zhang, S. Varghese, R. C. P. Verpaalen, A. P. H. J. Schenning, C. W. M. Bastiaansen, T. Peijs, *ACS Appl Mater Interfaces* **2020**, *12*, 33210.
- [32] J. S. Horvath, *New York Civ Eng Dep* **1998**, *35*.
- [33] I. M. Ward, *Macromol Symp* **1995**, *98*, 1029.
- [34] L. E. Govaert, P. J. Lemstra, *Colloid Polym Sci* **1992**, *270*, 455.
- [35] L. E. Govaert, C. W. M. Bastiaansen, P. J. R. Leblans, *Polymer* **1993**, *34*, 534.
- [36] X. Pan, N. Grossiord, J. A. H. P. Sol, M. G. Debije, A. P. H. J. Schenning, *Adv Funct Mater* **2021**, *31*, 2100465.
- [37] J. Liu, Y. Gao, H. Wang, R. Poling-Skutvik, C. Osuji, S. Yang, *Adv Intell Syst* **2020**, 1900163.
- [38] S. Ernst, D. Keil, K. Reiner, B. Senns, *DE Patent NO.102016213372A1* **2016**.
- [39] G. K. White, C. L. Choy, *J Polym Sci Polym Phys Ed* **1984**, *22*, 835.
- [40] X. Pan, A. H. P. J. Schenning, L. Shen, C. W. M. Bastiaansen, *Macromolecules* **2020**, *53*, 5599.
- [41] C. L. Choy, F. C. Chen, E. L. Ong, *Polymer* **1979**, *20*, 1191.
- [42] S. S. D. Lafleur, L. Shen, E. J. T. W. Kamphuis, S. J. A. Houben, L. Balzano, J. R. Severn, A. P. H. J. Schenning, C. W. M. Bastiaansen, *Macromol Rapid Commun* **2019**, *40*, 1800811.
- [43] L. Shen, S. S. D. La, S. J. A. Houben, N. Murphy, J. R. Severn, C. W. M. Bastiaansen, *Langmuir* **2017**, *33*, 14592.
- [44] N. A. J. M. van Aerle, A. W. M. Braam, *J Mater Sci* **1988**, *23*, 4429.
- [45] P. A. Irvine, P. Smith, *Macromolecules* **1986**, *19*, 240.
- [46] J. E. Huber, N. A. Fleck, M. F. Ashby, *Proc R Soc London Ser A Math Phys Eng Sci* **1997**, *453*, 2185.
- [47] T. Mirfakhrai, J. D. W. Madden, R. H. Baughman, *Mater Today* **2007**, *10*, 30.
- [48] J. D. W. Madden, N. A. Vandesteeg, P. A. Anquetil, P. G. A. Madden, A. Takshi, R. Z. Pytel, S. R. Lafontaine, P. A. Wieringa, I. W. Hunter, *IEEE J Ocean Eng* **2004**, *29*, 706.
- [49] R. Kornbluh, R. Pel, J. Eckerle, J. Joseph, *IEEE Int Conf Robot Autom* **1998**, *3*, 2147.
- [50] O. D. Sherby, J. E. Dorn, *J Mech Phys Solids* **1958**, *6*, 145.

Chapter 7

Technology assessment

7.1 Introduction

The incorporation of a variety of additives into drawn polymer films has been reported in this thesis. A new model describing the effects of low molecular weight, monodisperse additives (waxes) in drawn polyethylene films with a wide molecular weight distribution was presented, enabling an explanation of the experimental results (Chapter 2). Ultra-drawn polyethylene and graphene composite films exhibit both high thermal conductivity and visible light transmission (Chapter 3). Drawn polyvinyl alcohol films combined with graphene oxide and a co-additive show an approximately 3-fold increase in in-plane thermal conductivity in comparison to the neat drawn polyvinyl alcohol films due to the simultaneous polymer chain orientation and hydrogen interactions between the polyvinyl alcohol and graphene oxide dopant (Chapter 4). Ultra-drawn polyethylene films with graphene, UV and NIR dyes were explored as photoresponsive actuators (Chapter 5 and Chapter 6). In this Chapter, we will assess these achievements and discuss existing challenges for future research and potential applications.

7.2 Increasing thermal conductivity of drawn polyethylene composite films

As presented in Chapter 3, drawn polyethylene films combined with a low concentration (0.1 wt%) of graphene and a co-additive (BZT) exhibit metal-like thermal conductivities. Although the thermal conductivity of these composite films slightly increases as the concentration of graphene increases beyond 0.1 wt% (**Figure 3.6c**), graphene cannot be dispersed well at these high concentrations due to the strong interaction between graphene platelets. To increase the concentration of highly thermal-conductive additives, more soluble, well-defined graphene nanoribbons containing alkyl chains (GNRs)^[1] might be a solution. Preliminary research in this direction indicates that the thermal conductivity of the drawn polyethylene films with different concentrations (0.1 wt% and 0.2 wt%) of GNRs increases upon the increasing concentration of GNRs (**Figure 7.1**). Although the thermal conductivity of polyethylene doped with GNRs appears a little lower than that found for polyethylene doped with GN, there is potential for the improvement in the thermal conductivity by increasing the concentration of GNRs. Unfortunately, due to the limited amount of GNRs available, these experiments could not be carried out.

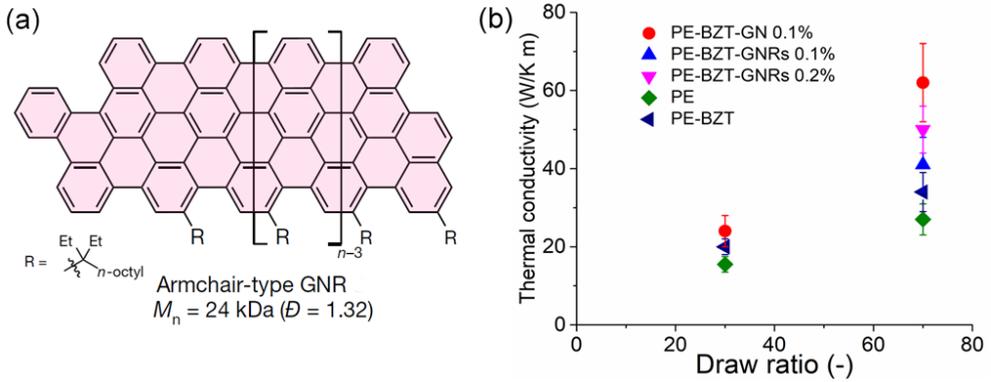


Figure 7.1 (a) Chemical structure of GNR used in this study.^[1] (b) Thermal conductivity of drawn polyethylene composite films as a function of draw ratio. Here, PE-BZT-GN, PE-BZT-GNRs, and PE-BZT represent the drawn polyethylene films with BZT and graphene, drawn polyethylene films with BZT and graphene nano-ribbons, and drawn polyethylene films with BZT, respectively.

To improve the thermal conductivity of polymer composite films, other factors beyond the preparation technology of drawn polymer films and the dispersion of additives should be considered, since intra- and inter-molecular phonon transport in polymers play vital roles and depend on chain orientation, crystallinity, draw ratios, and interaction between the anisotropic matrix and any additives. These structure-property relationships shed light on how to design anisotropic polymers and polymer composites with high TCs ($\sim 100 \text{ W m}^{-1} \text{ K}^{-1}$ for neat polymer^[2] and $\sim 75 \text{ W m}^{-1} \text{ K}^{-1}$ for polymer composites^[3]). Design concepts for fabricating highly thermally conductive polymers and polymer composites can be summarized as follows:

1. Positive factors impacting thermal transport include chain orientation (via crystallinity or drawing), crystal packing, chain length, M_n , and strong intermolecular interactions, while the negative factors include internal voids, presence of side chains, and chemical mismatches.

2. If they can be properly drawn with high draw ratios, polymers with a high M_n can form highly anisotropic materials. In these anisotropic materials, the high chain orientation and crystallinity may be achieved to improve thermal transport in polymer chains.

3. Drawn polymer composites consisting of drawable polymers doped with high thermal conductive fillers are strongly recommended to achieve high TCs at low filler contents if defects and voids can be avoided. Effective interaction between the fillers and polymer matrix is highly desired in these systems, such as via π - π interactions or hydrogen bonds, both interactions being capable of improving intra- and/or intermolecular phonon transport and decreasing the phonon scattering at the interfaces.

7.3 Scalability, reprocessability, and recyclability of drawn polyethylene composite films

The research of polyethylene films and fibers has progressed significantly over the last several decades, resulting in materials with both excellent mechanical properties and chemical resistance. However, scaling up production and applying polyethylene composites in high-end products like soft actuators remains a challenge. These well-aligned films were obtained by lab-scale solution-casting and solid-stretching at 125 and 130 °C, respectively. Although the size of these films can be controlled by the initial size of the undrawn films, the fabrication cost is relatively high. For scalability and reduced fabrication costs, new and optimized fabrication techniques would be appealing and feasible using the fabrication process of commercial polyethylene fibers.

The widespread application of polymers has resulted in ‘white pollution’ due to their poor biodegradability: approximately 0.26 gigatons of plastics are wasted annually, and polyethylene plays a significant role in these contaminations.^[4] If this waste could be recycled properly, it could potentially reduce 2% of the total global carbon dioxide emissions.^[4] The fraction of UHMWPE in this enormous waste stream is extremely small (< 0.01 %). Despite this, recycling and circularity are gaining interest and, for instance, green(er) products based on bio-ethylene were recently commercialized.^[5] Industrial recycling of waste streams (UHMWPE/solvents) in the Western Hemisphere is already common practice for a long time. Recycling of end-of-life products remains problematic especially in life protection (anti-ballistic) and biomedical applications and often results in down-cycling if it occurs at all. This is partly related to recovering, separating, and cleaning of the waste products and, as a consequence, incineration is quite common (polyolefines are considered as “white oil” due to their high caloric value). Here, the issues with respect to recycling and circularity are not addressed or resolved. It is expected that the small amounts of additives and co-additives will also not make these issues any better or worse.

7.4 Drawn polyethylene composite films for thermal management

Thermal management is vital to the lifetime and performance of many electronic devices, including solar cells, and microchips. With the widespread application of electronics, effective thermal management with thermally conductive materials has become a major technological challenge.^[3,6] In general, the traditional thermal conductors include metals and carbon materials. Generally, the common thermal conductors used in daily life, including copper ($\sim 400 \text{ W m}^{-1} \text{ K}^{-1}$), silver ($\sim 420 \text{ W m}^{-1} \text{ K}^{-1}$), and aluminum ($\sim 270 \text{ W m}^{-1} \text{ K}^{-1}$), possess high thermal conductivity. Potential alternatives are polymers and polymer composites due to their relatively low costs and ease of processing, diverse functionalities, excellent corrosion, and chemical resistance, and light weights.^[7] Although the maximum thermal conductivity of drawn polymers and their composites is in the range of 60-100 $\text{W m}^{-1} \text{ K}^{-1}$,

lower than that of common thermal-conductive metals, the specific thermal conductivity per unit density of drawn polymers and their composites should be greater or close to that of above-mentioned metals (**Figure 3.6**), indicating the potential application of drawn polymers and their composites for thermal management.

In devices such as solar cells, thermal conductors with high transmission of visible light are highly sought after. The surface of drawn polyethylene/wax films is shown in **Figure 7.2**. There are no obvious defects on the surface of the drawn films, which, along with their high transparency to light in the visible wavelength region and promising thermal conductivity, could make them interesting. To avoid surface scattering a coating could be applied.

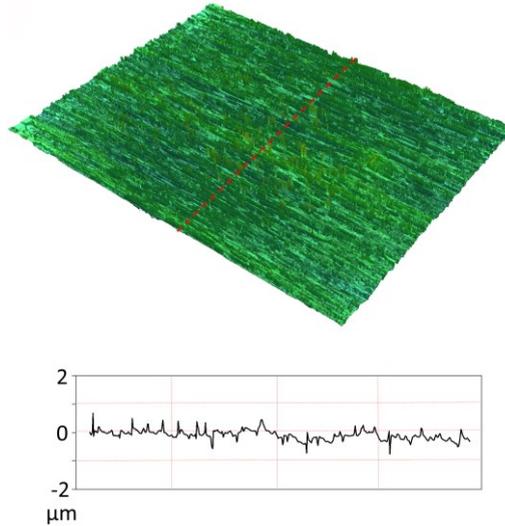


Figure 7.2 Surface (top) structure and roughness of PE-wax D-1 films with a draw ratio of 30. The scanning follows the red line.

7.5 Drawn polyethylene composite films for photothermal actuators

The Young's modulus of drawn polyethylene films in the drawing direction increases with the draw ratio following the Irvine-Smith model,^[8] reaching approximately 300 GPa, greater than most materials (**Figure 7.2**), although the modulus of drawn polyethylene perpendicular to the drawing direction is only around 1 GPa, which is close to that of human muscles.^[9] For both drawn and undrawn composite polyethylene films, adding a small content (< 1 wt%) of additives like graphene oxide and graphene has effective enhancement in their mechanical, thermal, structural, and wettability properties.^[10-13] Thus, drawn polyethylene and its composites present attractive mechanical properties in materials with relatively low density ($\sim 1000 \text{ kg/m}^3$). Of course, strength, impact resistance, and strain at break are also important parameters for fabricating robust polymer actuators.

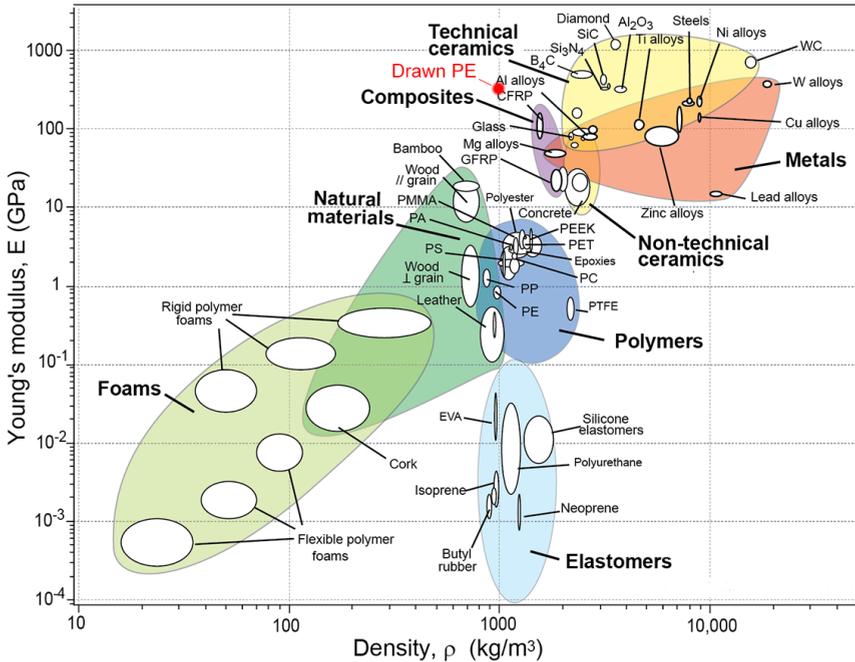


Figure 7.3 Young's modulus of different materials as a function of density.^[14]

Photothermal actuators can convert light energy into mechanical energy to realize a variety of locomotions such as bending, twisting, sinking, and floating, which makes them an excellent candidate for use in the field of soft robotics, micromachines, and intelligent systems.^[15] Generally, the thermally responsive actuators include mainly photothermal and electrothermal actuators. Compared with electrothermal actuators, photothermal actuators have an advantage because they do not require complex wiring systems and can be remotely controlled in a non-contact manner. Moreover, (IR) light is a safe and sustainable energy source, and it can be precisely directed. Typically, photothermal-driven strategies can be classified into two categories: one of the photothermal strategies relies on the periodic deformation caused by light-induced heat. However, the high temperature (often > 100 °C) caused by the photothermal effect often weakens the actuators, compromising both safety and durability. Another light-driven strategy relies on the Marangoni effect that has the advantages of directly realizing the light-to-work conversion. However, the photothermal actuators based on the Marangoni effect usually require a high-temperature gradient (above 45 °C) to produce a surface tension gradient strong enough to generate motion, and can only realize a specific type of motion for a specific shape.^[16] There is a common issue in both photothermal and electrothermal actuators, which is the limited response and recovery times

caused by the slow heat transport between actuation elements and slow heat release to the surroundings resulting from the low thermal conductivity of actuators. Drawn polyethylene composite films with high thermal conductivity can potentially overcome these limitations.

7.6 Conclusions

The potential impact of thermal management has highlighted the promise of drawn polyethylene films for the realization of rapid thermal transport and release. This thesis has demonstrated these polymers and their composites have potential in thermal management, and the high thermal conductivity of drawn polymers can be obtained by adding additives or adopting the polymers with high M_n . This concept is not only applicable for polyethylene films but also other polymers such as polyvinyl alcohol. The exploration of thermal-conductive polyethylene composite films in light-responsive actuators has also been demonstrated.

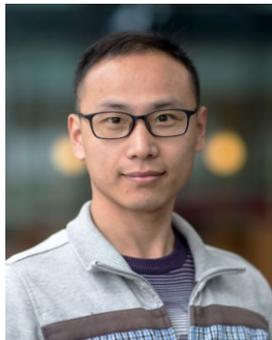
It can be foreseen that drawn polymers with high thermal conductivity will play an important role in the thermal management of optoelectronic devices and new advanced applications such as soft actuators.

Chapter 7

7.7 References

- [1] Y. Yano, N. Mitoma, K. Matsushima, F. Wang, K. Matsui, A. Takakura, Y. Miyauchi, H. Ito, K. Itami, *Nature* **2020**, 588, 180.
- [2] S. Shen, A. Henry, J. Tong, R. Zheng, G. Chen, *Nat Nanotechnol* **2010**, 5, 251.
- [3] X. Pan, L. Shen, A. P. H. J. Schenning, C. W. M. Bastiaansen, *Adv Mater* **2019**, 31, 1904348.
- [4] I. Vollmer, M. J. F. Jenks, M. C. P. Roelands, R. J. White, T. van Harmelen, P. de Wild, G. P. van der Laan, F. Meirer, J. T. F. Keurentjes, B. M. Weckhuysen, *Angew Chemie Int Ed* **2020**, 59, 15402.
- [5] X. Pan, M. G. Debije, A. P. H. J. Schenning, *ACS Appl Polym Mater* **2021**, 3, 578.
- [6] C. T'Joen, Y. Park, Q. Wang, A. Sommers, X. Han, A. Jacobi, *Int J Refrig* **2009**, 32, 763.
- [7] A. U. Chaudhry, A. Mabrouk, A. Abdala, *Integr Med Res* **2020**, 9, 10796.
- [8] P. A. Irvine, P. Smith, *Macromolecules* **1986**, 19, 240.
- [9] M. K. Shin, G. M. Spinks, S. R. Shin, S. I. Kim, S. J. Kim, *Adv Mater* **2009**, 21, 1712.
- [10] Y. Pang, J. Yang, T. E. Curtis, S. Luo, D. Huang, Z. Feng, J. O. Morales-Ferreiro, P. Sapkota, F. Lei, J. Zhang, Q. Zhang, E. Lee, Y. Huang, R. Guo, S. Ptasinska, R. K. Roeder, T. Luo, *ACS Nano* **2019**, 13, 1097.
- [11] S. Lin, M. A. S. Anwer, Y. Zhou, A. Sinha, L. Carson, H. E. Naguib, *Compos Part B Eng* **2018**, 132, 61.
- [12] S. Suñer, R. Joffe, J. L. Tipper, N. Emami, *Compos Part B Eng* **2015**, 78, 185.
- [13] L. Shen, K. Nickmans, J. Severn, C. W. M. Bastiaansen, *ACS Appl Mater Interfaces* **2016**, 8, 17549.
- [14] M. F. Ashby, *Mater Environ* **2013**, Chapter 9, p.603.
- [15] D. Pan, D. Wu, P. J. Li, S. Y. Ji, X. Nie, S. Y. Fan, G. Y. Chen, C. C. Zhang, C. Xin, B. Xu, S. W. Zhu, Z. Cai, Y. L. Hu, J. W. Li, J. R. Chu, *Adv Funct Mater* **2021**, 31, 2009386.
- [16] H. Xuan, Q. Guan, L. Zhang, Z. You, *Adv Funct Mater* **2021**, 31, 2009568.

Curriculum Vitae



Xinglong Pan was born in December, 1991 in Anhui, China. He finished senior high school at Fuyang Third High School in 2010. Thereafter, he studied at China University of Petroleum (East China) in Dongying and Qingdao majoring in Materials Physics. After receiving the Bachelor's degree in 2014, he continued his Master's study at China University of Petroleum (East China) in Qingdao majoring in Materials Science and Engineering under the supervision of Prof. Dr. Qingzhong Xue. After obtaining the Master's degree with the project of Gas Sensors and Gas Separation Membranes based on Nano-carbon Materials in 2017, he started his Ph.D. research in the group of Stimuli-responsive Functional Materials and Devices (SFD) at Eindhoven University of Technology (TU/e) under the supervision of Prof. Dr. Albert Schenning (SFD, TU/e) and Prof. Dr. Cees Bastiaansen (Queen Mary University of London) to develop Functional Drawn Polymer Composites for Thermal Management and Actuators. The most important results of his Ph.D. project are presented in this dissertation.

Publications related to this thesis:

1. **Pan, X.**, Shen, L., Schenning, A. P. H. J., & Bastiaansen, C. W. M.* Transparent, High-Thermal-Conductivity Ultradrawn Polyethylene/Graphene Nanocomposite Films. *Advanced Materials*, 2019, 31(40), 1904348.
2. **Pan, X.**, Schenning, A. P. H. J., Shen, L., & Bastiaansen, C. W. M.* The Role of Polyethylene Wax on the Thermal Conductivity of Transparent Ultradrawn Polyethylene Films. *Macromolecules*, 2020, 53(13), 5599-5603.
3. **Pan, X.**, Debije, M. G.* & Schenning, A. P. H. J.* High Thermal Conductivity in Anisotropic Aligned Polymeric Materials. *ACS Applied Polymer Materials*, 2021, 3(2), 578–587.
4. **Pan, X.**, Grossiord, N., Sol, J. A. H. P., Debije, M. G. & Schenning, A. P. H. J.* Three-dimensional Anisotropic Polyethylene as Light-responsive Grippers and Surfing divers. *Advanced Functional Materials*, 2021, 31, 2100465
5. **Pan, X.**, Verpaalen, R. C. P., Zhang, H., Debije, M. G., Engels, T. A. P., Bastiaansen, C. W. M.* & Schenning, A. P. H. J.* NIR-Vis-UV Light-Responsive High Stress-Generating Polymer Actuators with a Reduced Creep Rate. *Macromolecular Rapid Communications*, 2021, 42, 2100157.
6. **Pan, X.**, Debije, M. G., Schenning, A. P. H. J.* & Bastiaansen, C. W. M.* Enhanced Thermal Conductivity via Oriented Polyvinyl Alcohol and Graphene Oxide Composites. *ACS Applied Materials & Interfaces*, (Accepted)

Patents

Bastiaansen, C. W. M., **Pan, X.**, Schenning, A. P. H. J. Composite Film Comprising Ultradrawn UHMWPE and one or more (Co-) Additives. WO2020201502 A1

Publications not related to this thesis:

1. Liu, X., **Pan, X.**, Debije, M., Heuts, J. P., Mulder, D. J., & Schenning, A. P. H. J.* Programmable Liquid Crystal Elastomer Microactuators Prepared via Thiol-Ene Dispersion Polymerization. *Soft Matter*, 2020, 16(21), 4908-4911.
2. Cao, A., van Raak, R. J., **Pan, X.**, & Broer, D. J.* Temperature-and Light-Regulated Gas Transport in a Liquid Crystal Polymer Network. *Advanced Functional Materials*, 2019, 29(28), 1900857.

Acknowledgments

At the end of these four years, I would like to express my sincere gratitude to all those who helped me during my Ph.D. study.

First of all, I would like to thank my first supervisor, Prof. Albert Schenning. I truly appreciate your guidance and support during my Ph.D. period and making it such a memorable experience for me. Albert, you are an excellent group leader and I admire your passion, enthusiasm, and your ability to lead and unite our team.

I also would like to thank the supervision of Prof. Cees Bastiaansen. Cees, thank you for giving me a lot of interesting and challenging projects. After every discussion with you, your expert knowledge and original thinking motivated me to explore new projects. Thank you for giving me enough freedom to broaden and deepen my research interests, which encouraged me to become more independent and stronger. It is fortunate that after spending two years deeply studying the Beer-Lambert law we arrived at the correct conclusion.

Many, many thanks to the nice secretary in our group, Marjolijn. Thank you for your kind help over the last four years. I would like to thank Dr. Michael G. Debije for helping with my work and on this thesis. Also, thanks to Audrey Debije for a lot of writing help.

I would like to extend my sincere gratitude to other committee members: Prof. Dr. Quan Li, Prof. Dr. Leon E. Govaert, Prof. Dr. Željko Tomović, and Dr. Tom A. P. Engels, for taking the time to carefully read this thesis and give constructive suggestions. Thanks to Prof. Dr. Dick Broer for chairing my Ph.D. defense.

I am grateful to other SFD members who helped with all kinds of analyses and discussions during the past four years. Tom (ST, Sweet Tom), thank you a lot. Forgive me that I do not know how to express my appreciation for all your help, discussion, and encouragement. I hope I will receive information about your own Ph.D. one day. Xiaohong, thank you for being my shopping-companion and cooperation using Karma (to be honest, it is too bad, LOL). Li, thanks a lot. Yuanyuan, I wish you continued success and hope you find a good job. Wilson, thank you for your nice chats and jokes; Pei, thank you for your tasty fruit and biscuits. I hope all of you achieve your Ph.D. degrees soon. Simon and Gilles, thank you for many discussions, nice chats, and the invitation to your parties. Nadia, Jeroen Sol, Tom Engels (again), and Rob, thank you for your cooperation and I always enjoy your suggestions on the research as well as our chats. Ellen and Sarah, thank you for your help and suggestions for my Ph.D. Sean and Marina, thank you for your support with XRD measurements. Also, thanks to other kind members who have made or are making the passionate and positive SFD atmosphere: Alberto, Anahita, Arna, Bruno, Davey, Dirk-Jan,

Dongyu, Fabian, Jeroen, Johan, Laurens, Marc, Matthew, Roel, Sebastian, Strerre, Stijn, Yahi, Yiru. Of course, there is one word: Once an SFD member, always a member☺.

Lihua, 楼长 (Xianwen Lou), Jie, Huiyi, Shidong, and Junyu thank you for your help and/or lunch discussions. Anping and Mr. Pan, thank you for your encouragement and help, and hope that you have a happy family. Peipeng, Gang, Yuxuan, Xiaoxiao, Tao, Xuan, Yan, et al., thank you for your funny stories and discussion over mathematical statistics. I would say sorry to Prof. Pei, and thank you for your help. Also, I would like to thank Prof. Dr. Kenichiro Itami and Dr. Yuuta Yano for your graphene nanoribbons and hope we can continue to cooperate in the future. Thanks to my friends from the same master group, Liangyong Chu, Meixia Shan, Yehan Tao, Zilong Liu, Qikai Guo, and Wenbo Lu.

I would like to express my sincere gratitude to my parents. Thank you for your support and encouragement over the past few years. I want to thank my girlfriend for your silent support, which encourages me to the depths of my heart and I expect to meet with you one day. Finally, thanks to all the other kind people that I have met.

Xinglong Pan

2021-3 in Eindhoven